Effective Thermal Testing and Potential Design Solutions for PocketQube Subsystems

A thesis submitted to the Delft University of Technology in partial fulfillment of the requirements for the degree of

Master of Science in Aerospace Engineering

by

Timo Rühl

December 2018

to be defended publicly on Tuesday January 9, 2019 at 09:00 AM.
An electronic version of this thesis is available at https://repository.tudelft.nl/

Supervising Professor:	Prof. dr. Eberhard Gill
Supervisor:	ir. Jasper Bouwmeester
Co-reader:	ir. Kevin Cowan
Co-reader:	ir. Martin Lemmen

ACKNOWLEDGEMENTS

Before starting this report, I would like to thank everybody that contributed to completing this thesis project.

First of all, I want to express my gratitude and regards to Jasper Bouwmeester for his supervision and guidance over the past year. His valuable feedback, encouragements, and resourcefulness were essential to staying on track and finding solutions to the challenges I faced.

Further, I want to express my gratitude towards Alexander Maas, Amir Mirza Gheytaghi, Martin Lemmen and Mehmet Sevket Uludag for sharing their insights and providing me with valuable suggestions that helped to improve the quality of this work.

I want to thank my friends and beloved ones, particularly my roommates Lorenzo Fiori and Arthur Alglave, for their *supporto* and *sopporto* throughout this last year.

Finally, I would like to thank those I owe the most, my family.

Timo Rühl
Delft, December 2018

ABSTRACT

The PocketQube is an emerging satellite class, which pushes the miniaturization of space technology beyond the well-established CubeSats, promising rapid design-to-orbit cycles while lowering the cost of accessing space. A showstopper in the success story of nano- and picosatellites are their high mission failure rates. Environmental testing before flight is an effective means to identify design flaws and workmanship errors, and thus improve the chances of mission success. However, inefficiencies in the design process, low-budgets, and stringent schedule requirements often motivate small satellite developers to postpone environmental testing towards the end of the design lifecycle, where recovering for design flaws is inefficient. The project circumstance of nano- and picosatellite missions require, therefore, cost- and time-effective test strategies that facilitate early design evaluation.

This research proposes and implements a thermal screening method for PocketQube subsystems to identify temperature hotspots and verify their compliance against operational hardware limits. Key elements of the test method are a thermal IR temperature scan at ambient conditions and an estimation of the worst-case flight temperature using experimentally derived graphs that describe the vacuum heating of thermal hotspots. The study of subsystem layout options complements the screening method by providing solutions to mitigate hotspot overheating.

Moreover, the study proposes to lower the required pressure levels for thermal-vacuum testing of PocketQube subsystems. The analysis shows that, due to the small form factor, pressure levels by four orders of magnitude larger than those used in environmental test standards for larger satellites suffice to maintain the resulting temperature errors below 5K on the hot side of the temperature spectrum.

Both the screening method and moderation in vacuum requirements contribute to the development of subsystem test methods that match the needs of small satellite developers.

CONFERENCE PAPER

[1] Rühl, T., Bouwmeester, J. (2018). Effective thermal testing and design solutions for PocketQube subsystems. In *12th IAA Symposium on Small Satellites for Earth Observation (accepted)*, Berlin, Germany.

The conference paper is included in appendix C.

CONTENTS

LIST OF FIGURES

LIST OF TABLES

ACRONYMS

COTS Commercial off-the-shelf

DASML Delft Aerospace Structures and Materials Laboratory

DAQ Data acquisition

ECSS European Cooperation for Space Standardization

IC Integrated circuit

IR Infrared

LEO Low Earth Orbit

LWIR Short-wave infrared

MWIR Mid-wave infrared

NASA National Aeronautics and Space Administration

PCB Printed circuit board

QFN Quad flat no-leads

SSE Space Systems Engineering group

SMD Surface mount device

SWIR Short-wave infrared

VIA Vertical interconnect access

LIST OF SYMBOLS

Natural convection and gas conduction

α	Thermal diffusivity
$\bar{c}$	Mean kinetic energy
β	Coefficient of thermal expansion
κ	Heat capacity ratio
λ	Thermal conductivity
μ	Dynamic viscosity
ν	Kinematic viscosity
ρ	Density
a_E	Accommodation coefficient
c_p	Isobaric heat capacity
d_m	Mean particle diameter
h_{conv}	Convective heat transfer coefficient
Kn	Knudsen number
l^*	Characteristic length
M	Molar mass
Nu	Nusselt number
p	Pressure
Pr	Prandtl number
R	Ideal gas constant
Ra	Rayleigh number

Other Symbols

ΔH_{vap}	Enthalpy of vaporization
Δ	Absolute difference
A	Area
Bi	Biot number
m	Mass
n	Number
p_0	Standard boiling point pressure
r	Radius
T	Temperature

t Thickness

T_0 Standard boiling temperature

Thermal radiation

α Absorptivity

ϵ Emissivity

λ Wavelength

ρ Reflectivity

σ Stefan-Boltzmann constant

B_{ij} Gebhart factor

c Speed of light

F_{ij} View factor

h Planck constant

h_{rad} Radiative heat transfer coefficient

I Radiant existance

k_B Boltzmann constant

M Spectral existance

Thermal resistance analogy

$\dot{Q}$ Transferred heat

C Conductance

$h_{contact}$ Contact conductance

R Thermal resistance

Uncertainty margin

σ Standard deviation

1 INTRODUCTION

1.1 POCKETQUBES

The PocketQube promises to be the next step in the miniaturization of space technology. The introduction of the CubeSat form factor demonstrates the disruptive potential that standardization offers for the space sector. The form factor creates a market for standardized components and subsystems, as well as increasing launch opportunities (Jones, 2014; Woellert et al., 2011). The consequent reduction in cost and technical complexity lowers the entry barrier for developing satellites. As a result, the space sector opened to new actors traditionally excluded by the high upfront costs (Swartwout, 2016).

A cube of $5cm$ builds the basic unit of the PocketQube reducing the length scale of the popular CubeSat standard by a factor of two (Deepak and Twiggs, 2011). The miniaturization promises faster and cheaper design-to-orbit cycles, which make PocketQubes a promising platform for technology demonstrations and education purposes (Speretta et al., 2016; Bouwmeester et al., 2018).

The Institute for Space Systems at the TU Delft contributes to the promotion of PocketQubes through the development of the Delfi-PQ satellite. The institute's objective is to launch Delfi-PQ satellites regularly to improve the capabilities of its core platform iteratively. The Delfi-PQ will, therefore, provide a test bed for new technologies while stimulating educational needs. The ambition to launch PocketQubes in short time frames including frequent reconfiguration and design changes requires effective test and verification strategies to maintain the competitiveness of PocketQubes concerning cost and development time.

1.2 NANOSATELLITE MISSION FAILURES

A showstopper in the success story of nano- and picosatellites are their high mission failure rates (Swartwout, 2016; Bouwmeester and Guo, 2010). Design flaws and workmanship errors are primary reasons for the low mission success rates (Venturini et al., 2018; Swartwout, 2016). Testing and verification before flight are typically effective means to reveal design deficiencies and detect incorrect assemblies.

The scope and extent of test and verification campaigns vary among the actors engaging in small satellite design (Swartwout, 2016). Traditional satellite developers participating in small satellite design typically perform extensive test and verification campaign, such as they would for a large satellite. On the other hand, cost and schedule restrictions, together with inefficiencies throughout the design process, often motivate inexperienced design teams to cut back on verification and testing programs (Venturini et al., 2018; Swartwout, 2016; Langer and Bouwmeester, 2016). As a result, inexperienced satellite developers skip subsystem-level tests in favor of system-level verification towards the end of the design lifecycle (Venturini et al., 2018; Swartwout, 2016). At this stage, recovering for design issues becomes inefficient, which, ultimately, motivates sending the hardware to the launch provider with known defects (Venturini et al., 2018).

Several authors argue that spending more project resource on testing and verification will improve the mission success rate of nano- and picosatellites (Swartwout, 2016; Venturini et al., 2018; Langer and Bouwmeester, 2016; Guo et al., 2016; Dubos et al., 2010). Langer and Bouwmeester (2016) state that more cost- and time-efficient test strategies are necessary to match the needs and project circumstances of small satellite developers.

1.3 THESIS PROJECT – THERMAL TEST METHODS FOR POCKETQUBE SUBSYSTEMS

The aim of the thesis is to develop a test method to provide a means to quickly check compliance of PocketQube subsystems with the hardware temperature requirements. Moreover, the study aims to provide design solutions to mitigate thermal issue in response to non-compliance with the temperature requirements. The next chapter describes the proposed test method in detail and relates it to the chapters of this report.

The steps to implement the test method enable, moreover, to investigate suitable pressure levels for thermal-vacuum testing of PocketQube subsystems. The pressure level determines the cost for the necessary laboratory equipment. The definition of appropriate pressure levels contributes to developing cost-effective test strategies for PocketQubes.

The development and implementation of the thermal test method is main part of this thesis project. Accordingly, the main research question states as follows:

What are necessary elements to facilitate quick testing and re-design of PocketQube subsystems?

The following sub-questions relate to the main research questions and help in answering them:

- What measurement techniques are appropriate for thermal testing of PocketQube subsystems?
- Which pressure levels are necessary to support thermal-vacuum testing of PocketQube subsystems?
- What are effective design solutions to mitigate thermal issues?

2 PROPOSAL OF A THERMAL TEST METHODOLOGY

2.1 THERMAL TEST METHODS FOR SATELLITE SUBSYSTEMS

Thermal testing supports the design and verification process. A thermal test exposes satellite hardware to flight-like conditions, such as temperature extremes or vacuum. The exposure enables to verify functional performance, characterize the operational performance for system budgeting, and validate simulation models. Moreover, the operation of hardware in relevant environmental conditions demonstrates compliance with the temperature requirements deriving from the hardware specifications. (Welch, 2002; Brieß et al., 2009)

Table 1 presents an overview of the objectives for thermal testing and the related test methods. The last row introduces the thermal test methodology that builds the primary motivation for this thesis project. The remainder of this section details the thermal test methodology and, moreover, relates it to the chapters of this report.

Table 1: Summary of subsystem-level test objective and the relevant hardware models. The abbreviations PT, EM and FM, refer to *prototype*, *engineering model* and *flight model*. Information adopted from Welch (2002); Brieß et al. (2009).

Class	Objective	Description	Hardware Model
Functional characterization	Determining the performance characteristics for system budgeting.	Operating a subsystem at the operational worst-case temperature conditions.	EM / FM
Performance verification	Demonstrating that the system survives the environmental conditions while maintaining functionality.	Operating a subsystem in environment similar to orbital conditions, such as temperature cycles and vacuum.	EM / FM
Thermal model correlation	Providing measurement data to validate thermal simulation models.	Operating a subsystem or component or interface in an environment with well-known thermal boundary conditions.	PT / EM / FM
Stress screening	Reveal hardware flaws and workmanship errors.	Cycling the subsystem to the worst-case temperatures to induce thermo-mechanical loads.	EM / FM
Thermal screening method	Identification of thermal hotspots and verification of their compliance with hot-side temperature requirements.	Operating a subsystem at ambient conditions and estimating the worst-case operational temperature in flight conditions.	PT / EM / FM

2.2 THERMAL SCREENING METHOD FOR POCKETQUBE SUBSYSTEMS

The introduction of the PocketQube poses new challenges to thermal engineering. Two conditions motivate the development of a test methodology to verify compliance of subsystem boards with temperature requirements on the hot side of the allowable temperature range:

- The low mass of PocketQubes implies larger temperature oscillations (Speretta et al., 2016) and on-going research by Avila de Luis (2018) indicates that PocketQubes reach steady-state conditions during the sunlit part of the orbit.
- Moreover, the aspiration for miniaturization drives toward increasing the energy density of subsystem boards. Both aspects motivate the study of the hot-side thermal spectrum of PocketQubes.

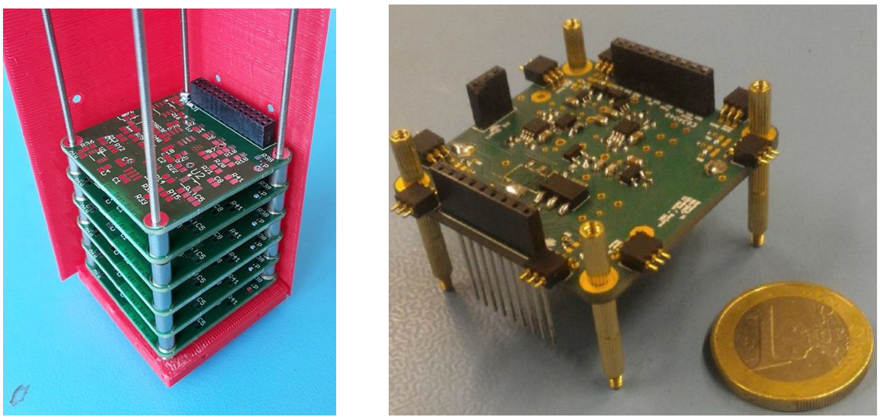

(a) (b)

Figure 1: PocketQube subsystem design. (a) Structural representation of the subsystem assembly for PocketQubes inside the satellite. (b) Representative PocketQube subsystem board including electronic components. Images taken from (DelfiSpace, 2016).

The thermal screening method aims at inspecting PocketQube subsystem board for critical thermal hotspots. The term thermal hotspot refers to components on a subsystem board that reaches high temperatures compared to the board. Thermal hotspots occur to components with poor heat sinking capabilities and high power density. The overheating of electrical components can jeopardize the functionality the component, and thus of a satellite subsystem.

The test method leverages the benefits of thermal IR imagery as a simple means to scan a subsystem board for thermal hotspots and measure their temperature. The IR scan, together with graphs describing the heating characteristics in flight conditions, enables to perform a judgment call about critical temperature conditions concerning the hardware specifications.

The application of a thermal camera for temperature screening of PCB based subsystems was applied in the Shuttle program (Foster, 1992), as well as in the development of the CubeSats UWE-3 (Busch et al., 2015) and the PharamaSat (Diaz-Aguado et al., 2009). The purpose of the IR scan in these publications is in identifying local thermal hotspots for the application of thermocouples in subsequent thermal-vacuum testing. On the other hand, this methodology uses IR imaging as the primary temperature acquisition technique.

The flowchart in figure 2 illustrates the steps to evaluate a subsystem board for critical temperature hotspots. The following list details each step of the methodology. The schematic in figure 3 outlines how to estimate a components flight temperature from the ambient IR scan.

1. A thermal IR camera enables to acquire a global temperature map of a subsystem. The temperature map contains information about thermal hotspots and their temperature increase relative to the subsystem board. Thermal hotspots are a target for further analysis

to verify that the components remain within the allowable temperature ranges during flight.

2. An IR scan is beneficial to capture the thermal behavior of the board. However, an IR scan of a subsystem yields the isolated behavior without the thermal interaction with other subsystems. Thermal simulation models describe the interaction of all satellite subsystems during various operational scenarios. The discretization in thermal simulation models during early development phases is typically low to keep the computational effort and accommodate for design changes. Early thermal simulation models typically represent subsystem boards by a few thermal nodes averaging the power dissipation over the area or volume of the board, see the thermal modelling strategies for previous Delfi satellite projects:
   - **DelFFi** The preliminary thermal model considers a single node per subsystem, while the detailed model discretizes the battery and propulsion payload into further nodes. (Van Boxtel, 2015)
   - **Delfi-n3xt** The thermal model considers each subsystem as a single node, which additional nodes assigned to the batteries. Macco (2014) reports that the lack of discretization results in discrepancies between model prediction and flight data.
   - **Delfi-C^3** The preliminary simulation model uses a single node per subsystem, while the detailed thermal model assigns dedicated nodes to the power amplifiers and batteries providing discretization for the component with the highest heat density per volume. (Graziosi, 2008).

   The combination of a simulation model of the entire satellite and a subsystem IR scan captures the system-level thermal interaction and resolves the board-level thermal behavior. The combination of both techniques provides a simple means to describe the thermal behavior of subsystems during early development phases. The measured hotspot temperature increase ΔT_{op} adds to the maximum subsystem temperature that the thermal simulation model predicts $T_{subsystem}$.

3. The previous bullet points implicitly assume that the IR scan occurs at ambient pressure and room temperature. The presence of natural convection at ambient conditions implies that the IR scan will yield a lower temperature increase of a hotspot than an equivalent test in a vacuum. An estimation of the maximum flight temperature, therefore, requires to consider the additional temperature increase between ambient and vacuum conditions $\Delta T_{amb \rightarrow vac} = T_{vac} - T_{amb}$. This project will use experiments on representative PocketQube subsystems to describe the additional temperature increase. The resulting diagrams enable to estimate the maximum flight temperature of thermal hotspots without the necessity to perform thermal-vacuum testing.

4. Thermal simulation models rely on parameter and modelling assumptions. The assumptions and simplifications typically translate into differences between predicted and actual flight temperatures. A thermal model uncertainty margin accounts for the differences between model and reality. The methodology accounts for the uncertainties by adding a margin to the predicted subsystem temperature. The magnitude of the uncertainty margin varies among actors and space missions. This thesis defines a thermal model uncertainty margin for PocketQubes by comparing simulation and flight data of nanosatellites.

5. The summation of all previous contributions yields an estimate of the maximum flight temperature of thermal hotspots. The temperature prediction enables to perform a judgment call whether the hotspot temperatures are critical concerning hardware limitations, $T_{margin} = T_{allowable} - T_{estimate}$. A hotspot component complies with the temperature requirements if the difference is above zero. Non-compliance implies that either more accurate analysis or re-design is necessary. The thermal screening method is a worst-case estimation because the IR scan measures thermally-isolated subsystem boards. Accordingly, the IR scan will show larger hotspot temperatures than in the actual satellite

assembly. More accurate analysis refers to either using higher fidelity thermal simulation models or measuring the hotspot temperature in a thermal-vacuum test. The choice for more accurate analysis or re-design depends on the necessary effort. This study investigates PCB layout parameters that provide solutions to mitigate hotspot overheating. The re-design of a subsystem board requires to re-iterate the screening method to verify the effectiveness of the design measure in lowering the hotspot temperature.

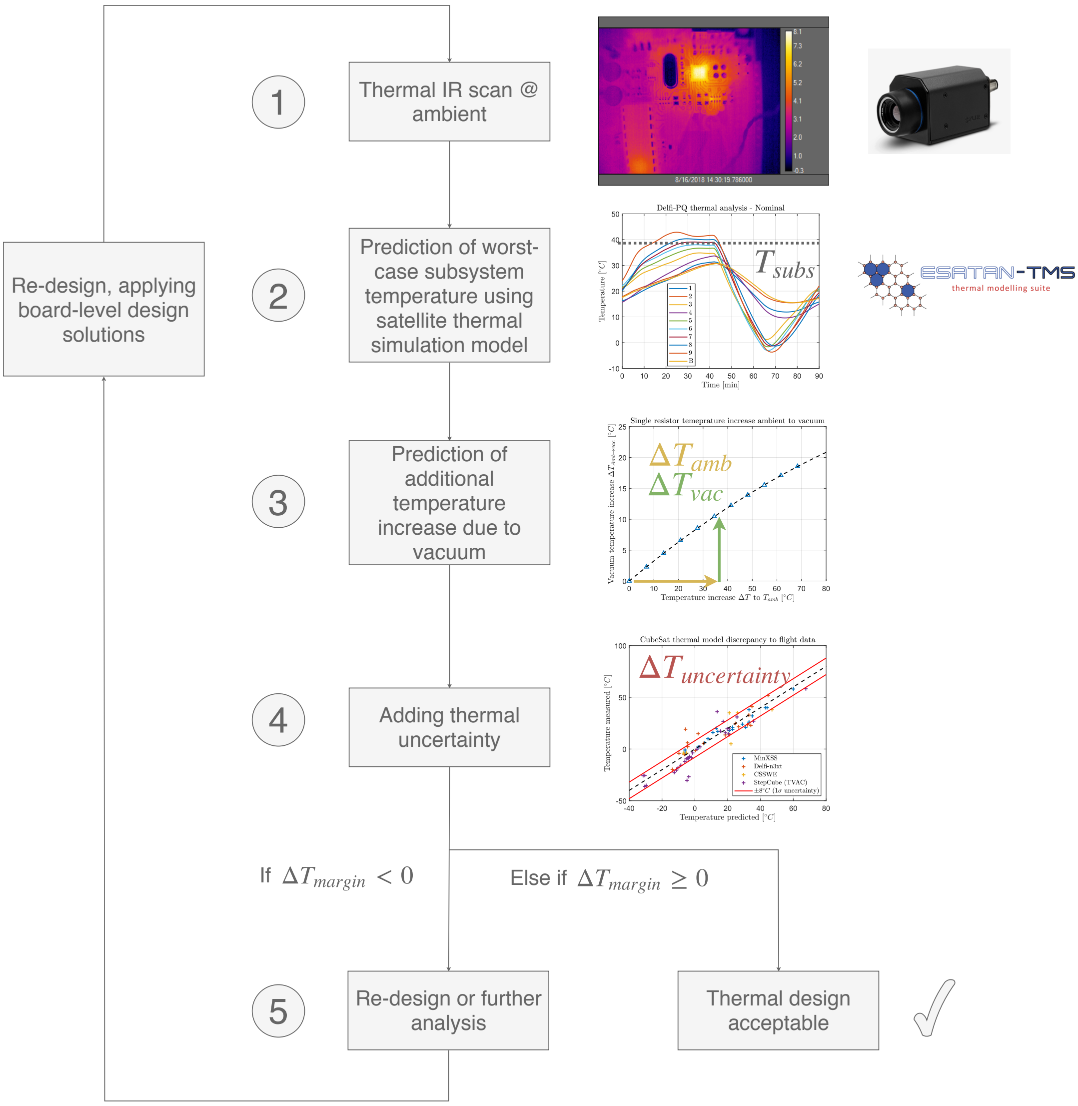

Figure 2: Proposed early thermal screening methodology flow and decision criterion. The image in step 2 derives from temperature data of the Delfi-PQ thermal simulation model provided by (Avila de Luis, 2018).

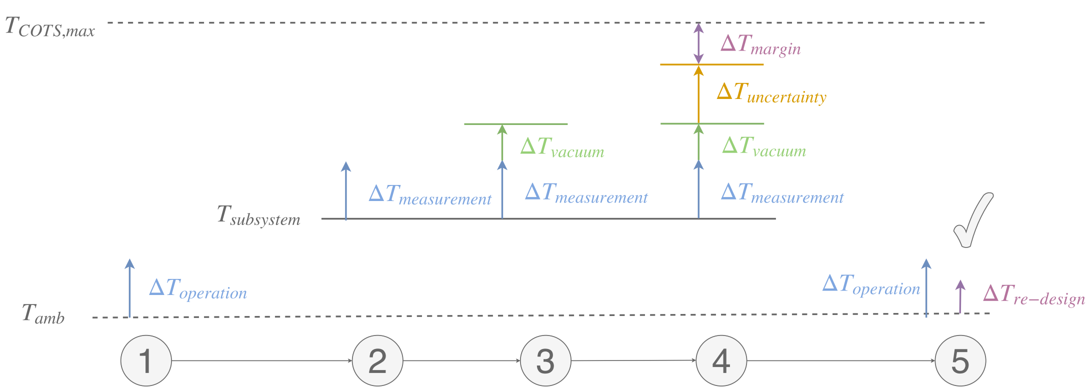

Figure 3: Evaluation scheme for checking compliance of thermal hotspots with the maximum hardware temperatures.

The chapters of this report describe the process of implementing the proposed thermal screening method. Necessary steps include characterizing the measurement performance of IR cameras, determining the temperature increase of components in the absence of natural convection, defining a thermal uncertainty margin and evaluating thermal design solutions.

Table 2: Outline of the chapters in the thesis report in relation to the proposed thermal screening method.

Step	Description and corresponding chapters in the report
1	Performance characterization of IR thermal imaging (Chapter 3) .
2	Prediction of the worst-cases subsystem temperatures. Inputs provided by parallel thesis project by Avila de Luis (2018) .
3	Investigation of the relative temperature increase between ambient and vacuum conditions. Analytical and experimental approach to describe the natural convection heat transfer coefficient (Chapter 4), experimental study using representative PocketQube subsystem boards (Chapters 6 and 8).
4	Defining thermal model uncertainty margin (Chapter 2.4).
5	Design of thermal design solutions by first analyzing the dominant thermal parameters on a PocketQube subsystem-level (Chapter 5) and then studying several design solutions through an experimental test campaign (Chapters 6 and 8).

2.3 THERMAL-VACUUM TESTING OF POCKETQUBE SUBSYSTEMS

The thermal screening method relies on graphs describing how much thermal hotspots heat up in vacuum conditions (step 3). The derivation of these graphs includes thermal-vacuum testing. The experiments provide an opportunity to characterize the error that arises from inaccuracies in the vacuum quality of a test facility. Quantification of the temperature error is a starting point to define the necessary pressure levels for thermal-vacuum testing of PocketQube subsystems.

The vacuum of space limits heat transfer to conduction and radiation. Test facilities reproduce the vacuum conditions on ground. The vacuum quality of a test facility determines its price and the amount of residual gas in the test environment. Residual gases introduce inaccuracies concerning flight conditions. The residual gas creates additional heat paths through convection and gas conduction that introduce temperature errors compared to ideal vacuum conditions.

The test objectives determine the acceptable temperature error due to residual gas in the test environment. This thesis uses thermal balance testing as a case study to define a reference value for the acceptable temperature error. The objective of a thermal balance test is to provide experimental data to correlate a thermal simulation model for unknown parameters (Welch, 2002). The temperature error due to inaccuracies in the test environment must be lower than model uncertainty to improve the accuracy of the simulation model. The next section defines a thermal model uncertainty margin in support of the thermal screening method (step 4). The margin describes the uncertainty of thermal simulations models in predicting the subsystem flight temperatures. The margin will serve as a reference value for the parameter uncertainty in a subsystem simulation model before a thermal balance test. The uncertainty builds a threshold of the maximum temperature error due to imperfections of a test facility relative to ideal vacuum conditions.

2.4 THERMAL MODEL UNCERTAINTY MARGIN

The proposed thermal screening methodology relies on inputs from a simulation model of the satellite. Thermal simulation models rely on assumptions on thermal parameters and geometries. The assumptions typically translate into inaccuracies of the model predictions with respect to the measured flight temperatures. Thermal design standards describe thermal model uncertainty margins to ensure that the actual flight temperatures remain within the predicted boundaries. The margin policy typically varies among commercial, military, and governmental actors The thermal model uncertainty margin typically varies among the commercial, military, and governmental actors (Gilmore, 2002; ECSS, 2016).

A reference value for the thermal model uncertainty margin is $\pm 11K$ applied for early simulation models according to the MIL-STD-1540 standard(Gilmore, 2002). The $\pm 11K$ margin derives from statistical analysis of simulation and flight temperatures of traditional satellites in the 70s and aims to achieve 95% (2σ) confidence that the actual flight temperatures remain within the predicted boundaries (Welch, 2016; Gilmore, 2002).

Nano- and picosatellite developers typically adopt higher risk strategies than traditional actors (Venturini et al., 2018; Swartwout, 2016; Guo et al., 2014). The different risk-management approach motivates reducing margins, such as the thermal model uncertainty. For instance, the thermal design of the Delfi-n3xt uses half the uncertainty margin proposed in the guidelines by the European Cooperation for Space Standardization (ECSS) (Macco, 2014). Moreover, small satellites typically employ less temperature-critical hardware than traditional satellites and employ primarily passive thermal control hardware (Baturkin, 2005). The differences in risk management approach and thermal design justify revising the existing model uncertainty margin.

As of November 2018, only a handful of PocketQubes has been in orbit (Speretta et al., 2016) and temperature flight data are rare (Kovács and Józsa, 2018). The analysis, therefore, considers thermal flight data of CubeSat missions, see table for the reference missions 3. The graph in figure 4a shows the comparison between simulation and flight data for the temperatures of internal subsystems.

Table 3: Reference CubeSat missions to derive thermal model uncertainty margin for nano- and picosatellites.

Satellite	Class	Thermal Control System	Data Type	Reference
Delfi-n3xt	3U	Passive	Flight	(Macco, 2014)
MinXSS	3U	Active (heater)	Flight	(Mason et al., 2017)
CSSWE	3U	Active (heater)	Flight	(Gerhardt et al., 2013)
StepCubeLab	1U	Passive	Test	(Kang and Oh, 2016)

The temperature data yield an $\pm 8K(1\sigma)$ standard deviation for the subsystem temperatures assuming a Gaussian distribution of the data, see the histogram in figure 4b. The standard deviation corresponds to a 68% confidence level that the thermal simulation results remain within the predicted boundaries, see graph 4c for the relation between confidence level and thermal model uncertainty. This thesis assumes that a 1σ-confidence level is appropriate for PocketQubes considering the higher acceptance for risk.

The comparison between simulation and measurement data shows that thermal simulation models perform better in predicting the temperatures of the satellite interior than the exterior. Internal components are typically more temperature sensitive, which using a higher level of detail in modelling the satellite interior (Mason et al., 2017). The higher modelling accuracies in the thermal simulation model result in better prediction of the internal than external temperatures. The focus of this thesis is on internal subsystem boards, which justifies using the thermal uncertainty margin for the internal subsystems.

Table 4: Thermal uncertainty data assuming a Gaussian distribution of the deviation between simulation and flight data for the CubeSats in table 3. All values are given in $[°C]$

	Mean μ	Std. deviation σ
Internal and external	-2.4	10.6
Internal	-1.3	8.2

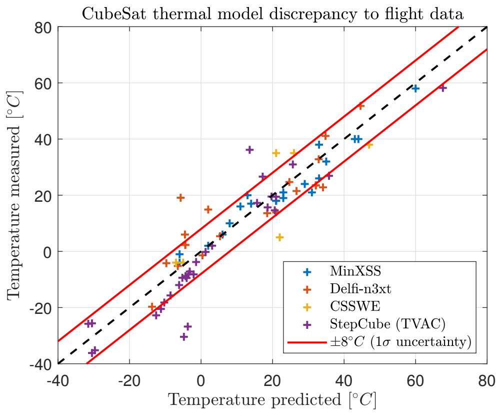

(a)

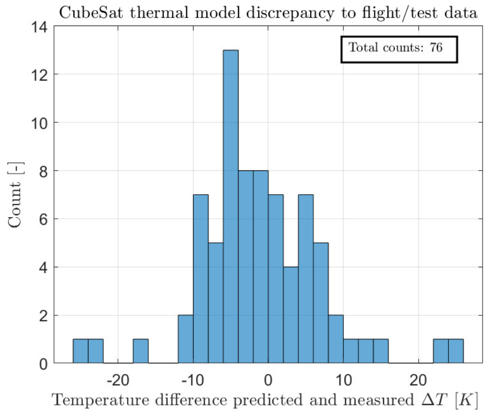

(b)

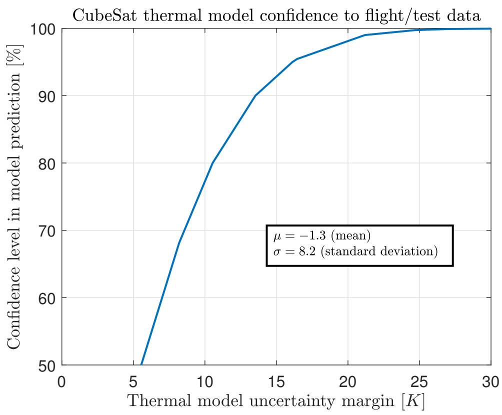

(c)

Figure 4: Derivation of a thermal uncertainty margin appropriate for nano- and picosatellites. (a) Comparison measurement with simulation data for four CubeSats. (b) Histogram of the temperature error. (c) Corresponding confidence graph assuming a Gaussian distribution of the error between simulation and flight data.

3 PERFORMANCE CHARACTERIZATION - THERMAL IR IMAGING

Temperature is the fundamental measurement parameter for thermal testing. Temperature measurements verify that the components remain within operational boundaries and validate thermal simulation models.

The thesis methodology relies on a thermal IR scan to identify local thermal hotspots and measure their temperature increase. Thermal IR imaging is a contactless measurement technique that samples the emitted IR radiation of an object. Thermal IR imaging presents inherent error sources due to background radiation and the emissivity of the body.

This study investigates the performance of thermal IR imaging in comparison to contact measurements using thermocouples, the most common temperature measurement technique in spacecraft thermal testing (Döring et al., 2016; Gilmore, 2002). The chapter starts with theoretical background information on thermal IR imaging. The analysis highlights the challenges of thermal IR imaging. An experimental test campaign uses the microcontroller of an Arduino UNO as a case study to compare the measurement performance of IR imaging with thermocouples. The comparison shows that thermal IR imaging can achieve the same accuracy as thermocouples in measuring relative temperature increases of electronics components. The experimental study, moreover, highlights that the correct application of thermocouples can be challenging.

3.1 THERMAL IR IMAGING

Thermal IR imaging, or thermography, is the process of deriving temperature images form IR signals. Bodies with a temperature above absolute zero emits IR radiation. Planck's law describes the radiative energy that a body emits, $I(T, \lambda)$, as a function of its temperature and wavelength per unit area (Vollmer and Möllmann, 2010; Carlomagno and Cardone, 2010; Breitenstein et al., 2010).

$$I(\lambda) = M_\lambda(T)\mathrm{d}\lambda = \frac{2\pi hc^2}{\lambda^5}\frac{1}{e^{\frac{hc}{\lambda k_B T}} - 1}\mathrm{d}\lambda \tag{1}$$

3.1.1 Wavelength bandwidths for IR imaging

Thermal IR cameras sample radiation in specific bandwidths of the IR spectrum. Table 5 lists the typical IR sampling bandwidths.

Table 5: Wavelength-classification of thermal IR cameras according to Vollmer and Möllmann (2010)

Classification	Wavelength range $[\mu m]$
Short-wave infrared (SWIR)	0.9 *to* 1.7
Mid-wave infrared (MWIR)	3 *to* 5
Short-wave infrared (LWIR)	8 *to* 14

The application of Planck's law over the entire wavelength spectrum yields the characteristics blackbody radiation curves, see the graph in figure 5a. The gray areas in the graph indicate the common bandwidths of thermal IR, and the red line describes Wien's displacement law.

Wien's law relates the temperature of a blackbody to the wavelength, at which the maximum IR radiation occurs.

The operational temperature range of COTS electronic components is of primary interest for this study. The graph in figure 5b shows Planck's law for the corresponding temperature ranging, which spans from -40 to $85°C$. Planck's law illustrates that maximum IR radiation occurs in the LWIR bandwidth. The maxima in the Planck curves imply that the LWIR spectrum is most suitable for thermal IR imaging of COTS electronics components, and thus PocketQube subsystems. Moreover, the graph shows that the spread between the temperature curves is smaller in the MWIR spectrum and almost non-existent in the SWIR spectrum. The lower spreading between the curves implies that sampling in the MWIR or SWIR spectrum requires better temperature resolutions. The higher temperature resolution typically implies higher cost for the equipment, see price list in table 7.

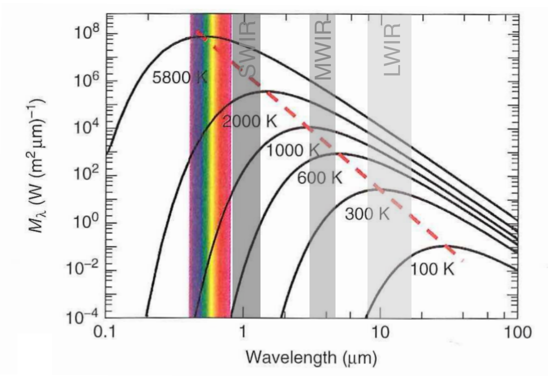

(a)

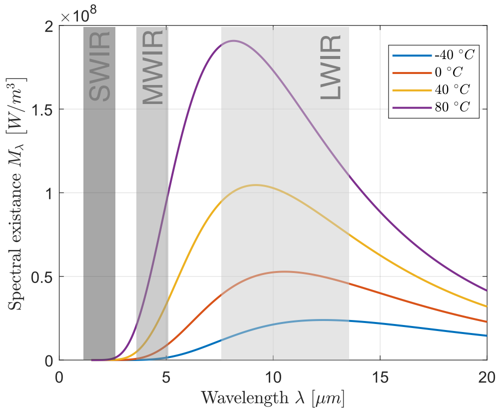

(b)

Figure 5: Planck Spectrum for a blackbody. (a) Planck spectrum over the visible, infrared, and microwave spectrum. (Image modified from (Vollmer and Möllmann, 2010)) (b) Planck spectrum for temperatures in the typical operational temperature range of COTS electronics components.

3.1.2 Emissivity and background radiation

The IR signal that a camera measures, I_{in}, is a superposition of IR radiation from various sources including the body of interest. An uncalibrated measurement will, therefore, show an apparent temperature of a body, instead of its real temperature. Error sources that add to the incoming IR signal are the to the IR measurement are reflected background radiation from the body of interest, absorption of IR radiation by the atmosphere and IR radiation that the optica

$$I_{in} = I_{body} + I_{refl} + I_{atmosphere} + I_{instrument} \tag{2}$$

The reflected background radiation, I_{refl}, is the most relevant signal that adds to the IR radiation of a body. This study considers that the distance between camera and object is $10cm$. The atmosphere exerts a negligible error source for these measurement distance (Carlomagno and Cardone, 2010; Meola and Carlomagno, 2004; Breitenstein et al., 2010). Moreover, thermal cameras typically compensate for the internal IR radiation, $I_{instruement}$, through auto-calibration.

The IR radiation that a body emits, I_{body}, is usually a fraction of the radiation that a blackbody of the same temperature emits. The emissivity is a material parameter that describes the ratio between the emitted and potential radiation of a blackbody, $\epsilon = I(\lambda)/I_{black}(\lambda)$ (Carlomagno and Cardone, 2010). Gray bodies are objects with an emissivity lower than unity. Kirchhof's law describes that the emissivity of gray bodies $\epsilon(\lambda)$ equals their absorptivity $\alpha(\lambda)$ for a specific wavelength. Kirchhof's law yields the relation 3 between emissivity ϵ and reflectively ρ for intransparent gray bodies. The relationship illustrates that emitted radiation dominates over reflected radiation for high-emissivity bodies, whereas for low-emissivity bodies the opposite applies. High-emissivity bodies, therefore, favor thermal IR imaging, whereas low-emissivity bodies are challenging to measure. PocketQube subsystems consist of PCBs with electronics components built on them. The electronics components entail both shiny and black plastic packages.

$$\epsilon(\lambda) + \rho(\lambda) = 1 \tag{3}$$

The IR radiation that a body emits is a function of its emissivity, ϵ_b, and temperature, T_b. Equation 4 describes the radiative energy that a gray body emits in a wavelegnth spectrum. The equation highlights that determining the true temperature of a body, T_b, from an IR measurement, I_{body}, requires knowledge about the emissivity, ϵ_b. The emissivity derives either from material databases in the literature or requires calibration.

$$I_{body} = \int_{\lambda_1}^{\lambda_2} \epsilon_b(\lambda) I_{bb}(\lambda, T) = \int_{\lambda_1}^{\lambda_2} \epsilon_b(\lambda) \frac{C_1}{\lambda^5 \left(e^{\left(\frac{C_2}{\lambda T_b}\right)} - 1 \right)} d\lambda \;\; C_1 = 2hc^2 \;\; C_2 = hc/k_B \tag{4}$$

Uncertainty about a body's emissivity translates into a temperature error ΔT. The graph in figure 6a shows the temperature error in LWIR spectrum when assuming an emissivity of unity, $\epsilon_{est} = 1$, for a body with an actual emissivity, ϵ_b. In other words, the graph shows the temperature error of assuming that an uncalibrated measurement yields the true body temperature.

$$I_{obj}(\epsilon_b, T_b) = I_{est}(\epsilon_{est}, T_{est}) \epsilon_b \int_{\lambda_1}^{\lambda_2} \frac{1}{\lambda^5 \left(exp\left(\frac{C_2}{\lambda T_b}\right) - 1 \right)} d\lambda = \epsilon_{est} \int_{\lambda_1}^{\lambda_2} \frac{1}{\lambda^5 \left(exp\left(\frac{C_2}{\lambda T_{est}}\right) - 1 \right)} d\lambda \tag{5}$$

Thermal IR cameras allow the user to set emissivity values to correct temperature readings. The graph in figure 6b shows the temperature error, ΔT, that derives from over- or underestimating the emissivity of a body at a particular wavelength, λ. The asymmetry in the graph derives from the logarithm in the error function, ΔT.

$$I_{obj}(\epsilon_b, T_b) = I_{est}(\epsilon_{est}, T_{est}) = I_{est}(\epsilon_b + \Delta\epsilon, T_b + \Delta T) \;\; \Delta T = \frac{1}{\frac{1}{T_b} - \frac{\lambda}{C_2} ln\left(\frac{\epsilon_b}{\epsilon_b + \Delta\epsilon}\right)} - T_b \tag{6}$$

The error graphs highlight the challenges of obtaining precise temperature measurements. Moreover, it becomes clear why high-emissivity bodies are suitable targets for thermal IR imaging, whereas low-emissivity bodies are challenging to measure.

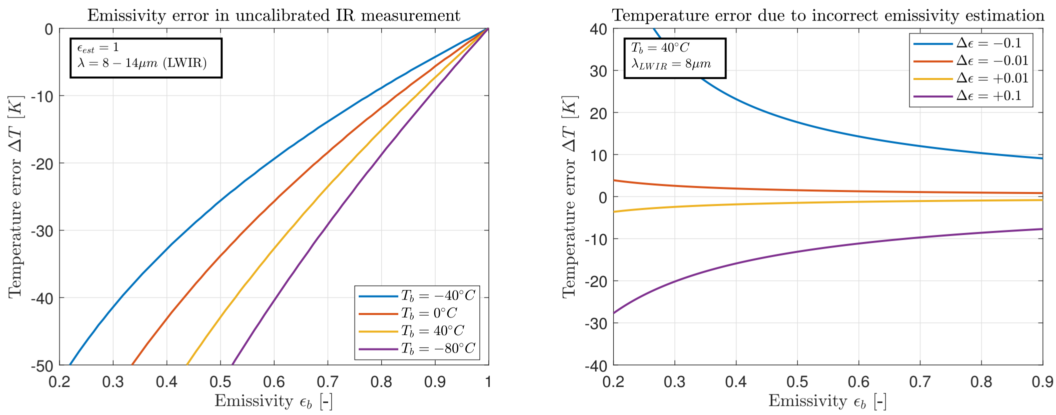

(a) (b)

Figure 6: Temperature error due to emissivity in IR measurements. (a) Temperature error, when assuming blackbody radiation with $\epsilon_b = 1$ (default camera setting). (b) Temperature error ΔT when estimating the emissivity incorrectly at each emissivity.

3.2 THERMOCOUPLE MEASUREMENTS

Thermocouples are contact sensors to measure temperature. A thermocouple consists of two wires with the tips being soldered or welded together to form a junction. The probe, when properly applied to a surface, obtains the same temperature as the surface. The temperature difference between the measurement junction and a second junction point induces a voltage difference. The underlying physical principle is Seebeck effect and the factor that relates voltage difference to thermocouple difference the Seebeck coefficient (Martynenko and Khramtsov, 2005; Bentley, 1998). The relative temperatures difference translates into an absolute temperature measurement with knowledge of the cold junction temperature. An option is to maintain the cold-junction at a known temperature, e.g., by placing the junction in an ice bath, or to determine the junction temperature with an absolute temperature sensor, such as a a thermistor. (Bentley, 1998)

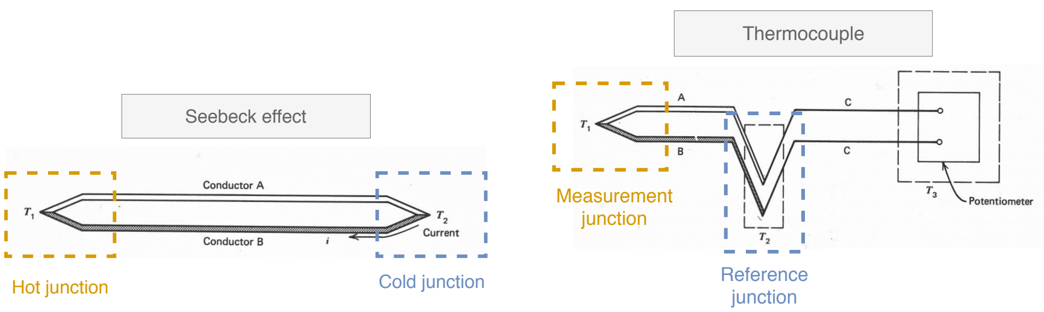

(a) (b)

Figure 7: (a) Seebeck effect. (b) Thermocouple working principle. Images modified from Kinzie and Rubin (1973).

A challenge for contact measurements is the correct application of the probe to the surface. The measurement requires sufficient contact pressure between the surface and the probe to sample the temperature. Attachment methods for thermocouples include removable and permanent techniques. A popular removable application technique include acrylic or silicone adhesive tapes. Permanent application techniques include soldering and epoxy adhesives.

3.3 THERMOCOUPLES VS. THERMAL IR IMAGING

Thermal IR imaging and thermocouple measurements offer both advantages and disadvantages. The thermal IR imaging offers high spatial resolution considering that each pixel is temperature measurement point. Moreover, the IR imaging is contactless, whereas the application of a contact sensor introduces additional heat paths and changes the optical surface properties. On the other hand, thermocouples present a higher measurement accuracy than thermal IR imaging. Besides, thermocouples are flexible towards application locations and test environments. Thermal IR cameras can only measure parts that are visibly accessible, and thermal IR cameras are rated for operation at ambient conditions.

Table 6 compares the performance of a thermal IR imaging with thermocouple measurements. The performance parameters derive from the available equipment, shown in table 7.

Table 6: Comparison of the performance characteristics of thermal IR imaging and thermocouple contact measurements. The quantitative performance parameters derive from the datasheets of the *FLIR A35* camera (FLIR, 2018) and the *NI9211* thermocouple DAQ device (National Instruments, 2015).

	Thermocouples	IR camera
Utilization	Popular measurement technique in thermal testing of space hardware (Döring et al., 2016; Gilmore, 2002).	Emerging in space thermal testing (Döring et al., 2016; Robinson et al., 2017), application in electronics development (Bagavathiappan et al., 2013; Fishburne, 2000).
Spatial resolution	Limited by the space for application and the available DAQ channels, e.g., 4 channels for NI9211.	Limited by camera resolution, each pixel provides a measurement point, e.g., 320×265 pixel camera provides 81.920 measurements.
Limit resolution	Limited by the physical size of the junction.	Limited by the instantaneous field of view, e.g., $f = 9mm$ focal length resolves $0.28mm$ objects at $100mm$ distance.
Nominal absolute accuracy	$\pm 1.5K$ (National Instruments, 2015; DSPE, 2018).	$\pm 5K$ nominal, $\pm 2 - 3$ with calibration (FLIR, 2018).
Applicability	Flexible towards application of various surfaces and liquids.	2D-mesurement in the field of view.
Handling	Manual application. Modification of the optical surface properties and thermal capacitance.	Contactless measurement without modification of the test object.
Error introduction	Insufficient surface contact pressure, introduction of additional heat paths, modification of the optical surface properites and thermal capacitance (Shaukatullah and Claassen, 2003).	Background radiation, incorrect emissivity setting.

Table 7: Performance characteristics of COTS thermal IR cameras and thermocouples. The information on the performance characteristics derive from the datasheets (FLIR, 2018) and (National Instruments, 2015).

Category	ID	Resolution	Accuracy (nominal)	Object temperature range	Cost [€]	Availability
IR cam.	ETS320	320x240	±3°C or 3%	−20 − 250	2.5k	✗
IR cam.	A35	320x256	±5°C or 5%	−20 − 130	5.6k	✓
IR cam.	A65	640x512	±5°C or 5%	−20 − 130	8.6k	✗
IR cam.	A315	320x240	±2°C or 2%	−20 − 350	9.5k	✓(DASML)
Thermoc.	K-type	N/A	±1.5°C	−75 − 250	8	✓
Thermoc.	DAQ & USB	4-TCs	±1.5°C	N/A	860	✓

3.4 CASE STUDY – ARDUINOUNO

Emissivity and background radiation present inherent challenges to thermal IR imaging. However, the benefits of thermal IR imaging are at hand. This section uses an ArduinoUNO board as a test case to evaluate the performance of the available thermal IR camera. The section evaluates, first, techniques to calibrate for background radiation and, second, for emissivity. Contact measurements using thermocouples serve as a reference to evaluate the IR measurements considering their higher nominal accuracy, see table 7.

3.4.1 Similarity to PocketQube subsystems

An ArduinoUNO board resembles PocketQube subsystems in several aspects. The ArduinoUNO is a PCB employing various types of electronic components, see the image in figure 8a. The Arduino PCB is a two-layer board including a $35\mu m$-thick copper ground plane on the bottom.

The ATmega16U2 microcontroller is the primary component of interest for this case study. The microcontroller has a $5 \times 5mm^2$ footprint and is a 32 pin connector (Atmel, 2012). The physical size of the microcontroller resembles the geometry of critical components for PocketQube subsystems, such as the power amplifier of the Delfi-PQ satellite (RFMD, 2018).

The PCB schematic in figure 8b illustrates the circuitry of the ATmega16U2 microchip. The mounting includes an exposed thermal pad (red) and a VIA that connects the chip with the ground plane on the bottom of the board (blue). The microcontroller resembles PocketQube components in size, tracing and mounting. The microchip, therefore, serves as a case study to evaluate the performance of thermal IR imaging for temperature measurements of electrical components on PocketQube subsystem boards. The execution of a continuous integration loop and communication script yields an operational temperature increase of the microcontroller.

3.4.2 Uncalibrated IR measurement

The default operation of the thermal IR camera assumes an emissivity of unity, $\epsilon = 1$, over the entire field of view. Moreover, the default measurement assumes that all incoming radiation originates from the emission of the body, $I_{in} = I_{body}$.

The IR image in figure 9a shows the camera read-out for a non-operational ArduinoUNO board. The center of the image is brighter than the edges meaning that the camera measures a temperature gradient between center and edges. However, the physical reality is that the ArduinoUNO is inactive, and thus at a uniform temperature. The observed temperature gradients imply that the uncalibrated IR measurement is incorrect. Table 8 shows the measured temperature at several locations and compares them with an absolute temperature measurement through a thermocouple applied on the ArduinoUNO board.

The IR image in figure 9b shows the camera read-out when operating the ArduinoUNO. The ATmega16U2 chip in the right corner heats up with the operation and spreads heat over

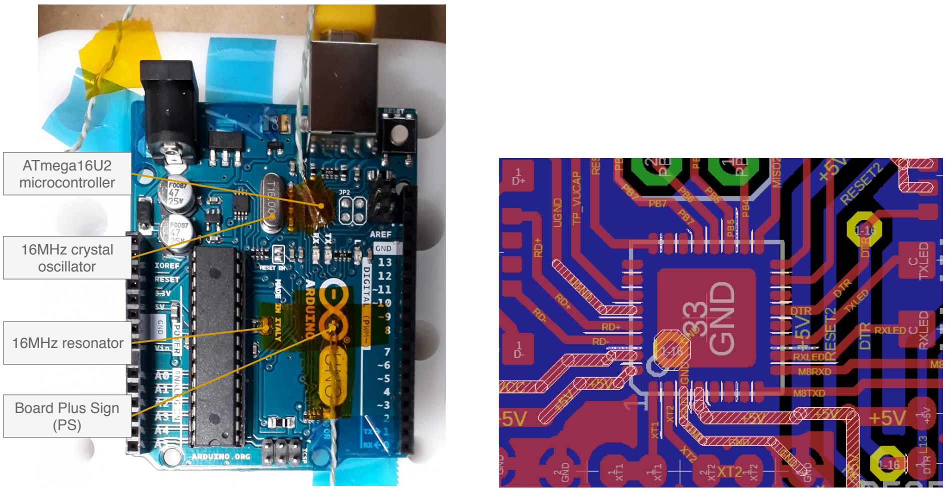

(a) (b)

Figure 8: ArduinoUNO board providing a case study for evaluating measurement techniques for PocketQube subsystem boards. (a) ArduinoUno on Delrin block. The image includes two thermocouples applied with polyimide foil. The thermocouples are removed for thermal IR measurements. (b) PCB schematic of the ATmega16U2 component illustrated in the EAGLE software program. (PCB schematic is taken from (Adafruit.com, 2010)).

the surrounding area. Several dark spots interrupt the continuous temperature map around the microcontroller. The dark spots occur on shiny, i.e., low-emissivity, components, see the image of the ArduinoUNO in figure8a.

The hottest component in both images is the 16MHz crystal oscillator. Other than the microcontroller, however, the oscillator shows no uniform heat spreading to the surrounding. Moreover, the oscillator appears as a bright spot, despite its metallic housing, and thus similarity to the dark spots around the microcontroller. Both the dark spots and the high temperature of the oscillator are a direct result of low emissivity considering the relation $\epsilon + \rho = 1$. The high temperature of the oscillator is due to reflection of background radiation, whereas the low temperature of the dark components is a consequence of the lower IR signal compared to the emission of the adjacent PCB area.

The comparison of the images proves that image correction techniques are necessary to compensate background radiation and emissivity. The next sections present techniques to compensate for both disturbances, ultimately, demonstrating that accurate temperature measurements are possible.

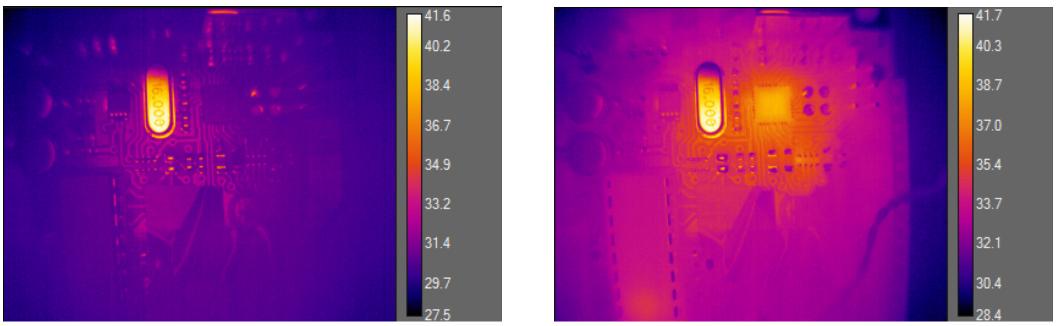

(a) (b)

Figure 9: Absolute IR measurement for the ArduinoUNO at (a) non-operational conditions and (b) operational conditions

Table 8: Overview of the absolute temperature measurement of the IR camera when the ArduinoUNO is inactive and operational, as well as the temperature difference to a thermocouple measurement. The parameter T_{IR} refers to the absolute measurement with the IR camera and $\Delta T_{IR-2-TC}$ to the temperature difference between the IR and thermocouple measurement. The measurement locations refer to figure 8a. All values are given in [°C]

	Arduino state	Microcontroller	Oscillator	Board PS (+)
T_{IR}	Inactive	30.5	40.4	30.5
$\Delta T_{IR-2-TC}$	Inactive	5.6	15.5	5.6
T_{IR}	Operational	38.3	40.5	33.3
$\Delta T_{IR-2-TC}$	Operational	4.5	9.7	5.0

3.4.3 Calibration for IR background radiation

Background radiation reflects from gray bodies and adds to the measurement signal that a thermal IR camera samples. The thermal IR image of the ArduinoUNO in figure 9a and 9b shows that a hot temperature source disturbs the thermal IR image. This subsection explores two approaches to correct for the background radiation in the ArduinoUNO case study. The first method consists of covering the ArduinoUNO from ambient light through a card box. The second method is to use digital image processing.

Card box

Heat sources around a test item emit thermal IR radiation. The disturbing thermal IR radiation reflects from the body of interest and adds to the measurement signal. An approach to correct the signal for the reflection of hot sources is to block their IR radiation.

A card box removes the influence of disturbing IR radiation sources that surround the test item. The card box material is opaque in the IR spectrum. The card box material, therefore, homogenize the background radiation to the thermal IR radiation that the card box emits due to its temperature, i.e., the environmental temperature. The homogenization enables to subtract the constant background signal from the signal of the body. The image in figure 10b illustrates a card box enclosure used for the ArduinoUNO case study. The thermal IR acquires temperature measurements through an opening on the top.

A simple means to test the effectiveness of this technique is to compare with a measurement without the card box. The images in figure and 10b illustrate the measurement set-ups for both cases. The resulting IR images illustrate that the disturbance persists despite the obstruction of the background radiation, see thermal IR images in figure 10c and 10d. The similarity in the pictures demonstrates that the IR emission by the camera itself is the major disturbance to the measurement. On the other hand, the PCB area on the edges shows the same temperature offset as in the uncalibrated measurement of the previous section. The alignment shows that the background radiation is equivalent to theIR radiation that the card box emits.

The alignment between the pictures leads to the conclusion that the usage of the card box is unnecessary. The thermal IR camera provides the dominant disturbance to the measurement. Moreover, the illumination conditions in the clean room of the faculty are stable, particularly when the window blinds are down. The background illumination provides, therefore, a constant offset to the measurement. Attempts to shift the camera away from the center and measure the Arduino with an angle are less satisfying than digital image subtraction, which the next section introduces.

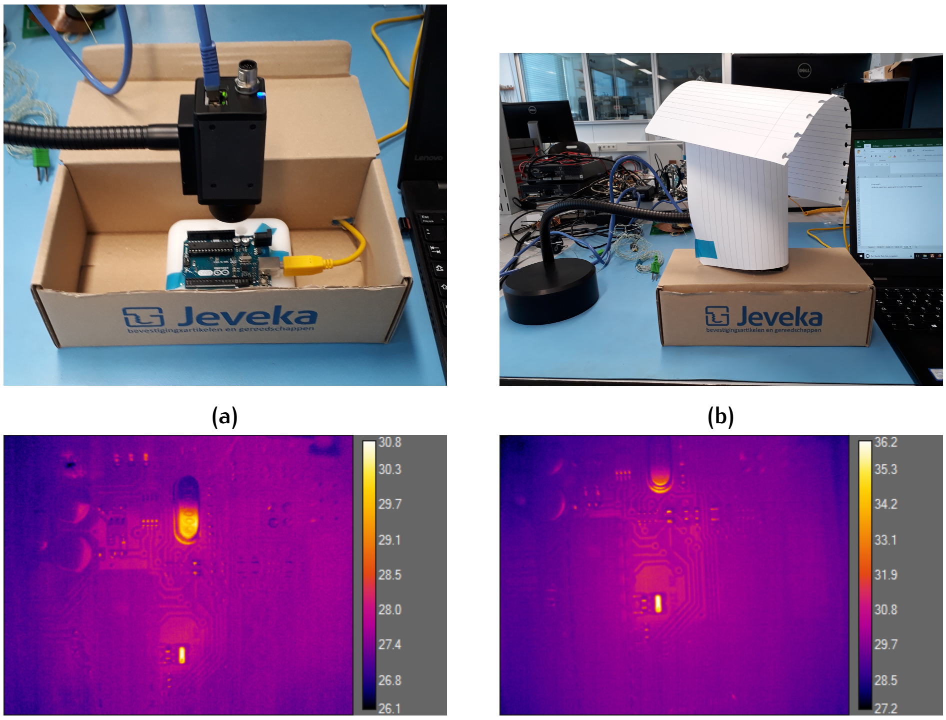

(a) (b)

(c) (d)

Figure 10: Test set-up for blocking disturbing background radiation. (a) Test set-up with an open box allowing surrounding heat sources and ambient light to disturb the measurement signal. (b) Test set-up with a closed box blocking the thermal IR radiation of ambient heat sources. (c) Thermal IR image of the inactive ArduinoUNO board with an opened and (d) closed box.

Table 9: Absolute temperature measurement of the IR camera with and without the card box closed. The parameter T_{IR} refers to the absolute temperature measured with the IR camera and $\Delta T_{IR-2-TC}$ to the error to the ambient temperature of the ArduinoUNO, which is measured with a thermocouple. All values are given in $[°C]$

Measurement	Arduino state	Microcontroller	Oscillator (bright spot)	Board PS (+)
T_{IR} (Box open)	Inactive	27.4	29.8	27.3
$T_{IR-2-TC}$ (Box open)	Inactive	2.8	5.2	2.7
T_{IR} (Box closed)	Inactive	29.4	33.2	29.6
$T_{IR-2-TC}$ (Box closed)	Inactive	4.8	8.6	5.0

Image Subtraction

The reflected background radiation provides a variable temperature offset over the cameras field of view. Digital image subtraction enables to correct the measurement for the constant offset. The schematic in figure 11a illustrates how an image of the inactive Arduino at ambient conditions removes the reflected background radiation. The outcome of the image subtraction is a temperature map that shows the relative temperature to the ambient temperature. The schematic implies that the technique requires alignment between the ambient and operational IR image.

The digital image subtraction removes the constant background radiation, see figure 11b. The temperature map shows, other than the previous images, the relative temperature increase of the ArduinoUNO during operation. The image shows that the subtraction removes the bright area in the center of the board, e.g., for the oscillator and resonator. The subtracted image confirms that the ATmega16U2 microcontroller heats the most.

The subtraction is effective in removing the background radiation. However, the subtracted image in figure 11b still shows dark spots that interrupt the continuous temperature field of the board. Table 10 shows the error in relative temperature increase between the thermal IR and the thermocouple measurement. The comparatively high temperature error demonstrates the necessity to correct for emissivity when trying to measure the temperature of the entire board.

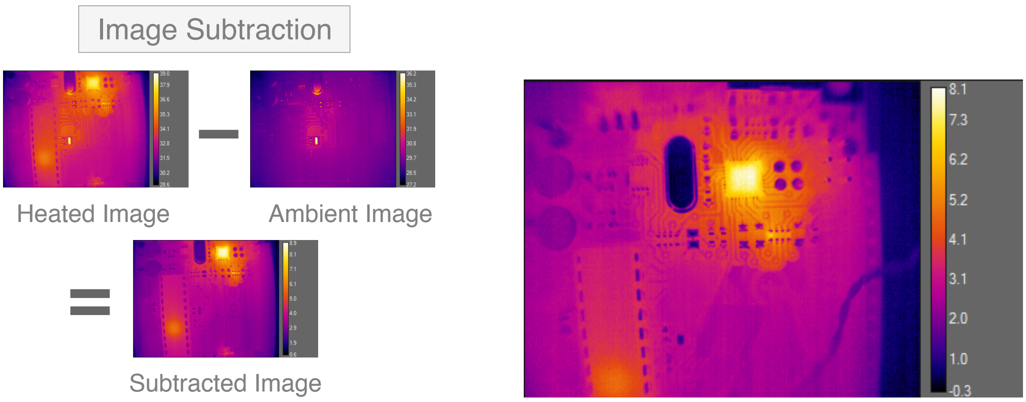

(a) (b)

Figure 11: Digital image subtraction to correct for constant background radiation. (a) Schematic of the image subtraction operation. (b) The outcome of the image subtraction shows the relative temperate increase. The corrected image still shows that correction for emissivity is necessary to obtain a correct image of the entire board.

Table 10: Measured temperature increase after applying the image subtraction. The parameters ΔT_{IR} refer to the measured temperature increase and $\Delta T_{TC-2-IR}$ to the error between the thermocouple and IR measurement. All values are given in $[K]$.

Measurement	Arduino state	Microcontroller	Oscillator	Board PS (+)
ΔT_{IR}	Operational	8.8	2.1	3.1
$\Delta T_{TC-2-IR}$	Operational	0.1	3.5	0.3

3.4.4 Calibration for emissivity

Thermal IR imaging requires for emissivity correction. The necessity for calibration becomes clear when heating the ArduinoUNO. The image in figure 12a illustrates the application of a heater foil to raise the temperature the ArduinoUNO. The temperature plot in figure 12b shows the error that results from using the default emissivity settings of, $\epsilon_b = 1$. The plot illustrates that the temperature error scales with temperature. The scaling illustrates that image subtraction alone is insufficient to achieve temperature measurement with the same accuracy as a thermocouple.

This section presents two techniques to correct the measurement for the emissivity. The first technique is to apply a high emissivity fluid on the board, and the second technique is two perform a two-point emissivity calibration using thermocouples and the heater foil.

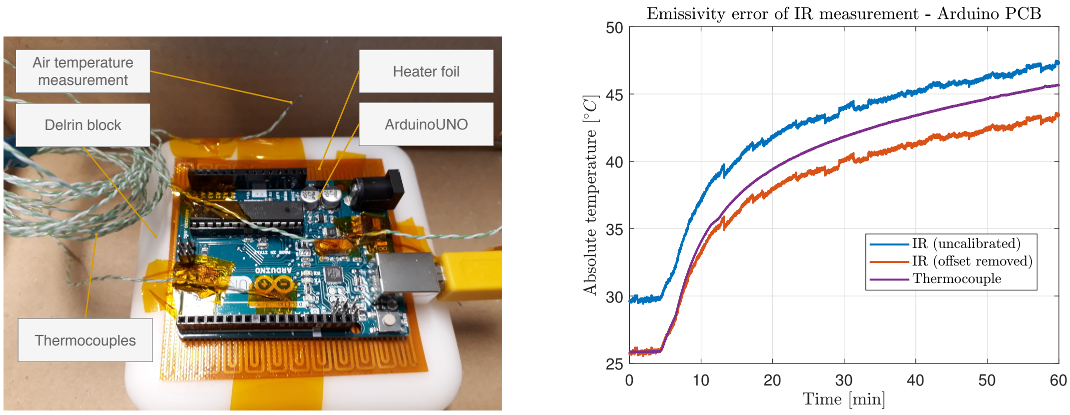

(a) (b)

Figure 12: (a) Test set-up to uniformly heat the ArduinoUNO. (b) Comparison of thermocouple and IR measurement of the PCB temperature at the plus sign.

High-emissivity fluid

The application of paint homogenizes the optical properties of a surface. This subsection uses COTS correction fluid to increase the emissivity of the ArduinoUNO board, see figure 13. Correction fluid is a removable, electrically isolating material with high emissivity, $\epsilon = 0.95$ (FLIR, 2015).

Figure 13: Application of a removable, high-emissivity fluid to the ArduinoUNO.

The thermal IR images confirm that the correction fluid removes the dark spots previously observed. The ambient measurement in figure 14a shows that IR radiation of the camera still disturbs the measurement despite the expected high emissivity. The thermal IR image in figure 14b illustrates the relative temperature increase of the Arduino after applying image subtraction to the measurement. The fluid removes the dark spots but also smears out the temperature gradient between the ATmega16U2 microcontroller and the PCB. The fluid provides additional heat paths and thus smoothens the temperature gradient.

The application of the correction fluid provides a small improvement in the measurement accuracy of the microcontroller and PCB, see table 11. The small difference in the temperature measurement implies that the emissivity of both locations is similar to the correction fluid. On the other hand, the emissivity correction removes the obvious contradictions in the thermal IR image of the image subtraction 11b. However, the application and removal of the correction fluid is time intensive. The benefit of applying the correction fluid is, therefore, questionable. The thesis methodology aims at identifying local thermal hotspots. The thermal hotspots are expected to occur on semiconductor components, such as the ATmega16U2 microcontroller, whose emissivity is similar to the correction fluid. However, the correction fluid provides a simple means to increase the emissivity of metallic components locally. The temperature gradients over the PCB indicate if a metallic component is a local thermal hotspot.

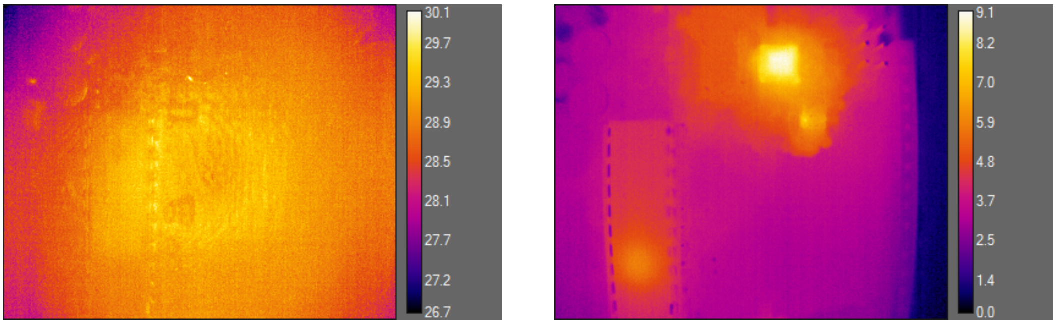

(a) (b)

Figure 14: ThermalIR measurement of the ArduinoUNO with correction fluid for emissivity correction. (a) Measurement of the non-operational Arduino. (b) Measurement of the operational Arduino after applying image subtraction to the measurement.

Table 11: Temperature measurement using the emissivity correction fluid. The parameter T_{IR} refers to the absolute IR temperature measurement, ΔT_{IR} to the measured temperature increase, $\Delta T_{IR,\epsilon=0.95}$ to the temperature increase accounting for the emissivity of the correction fluid, and $\Delta T_{IR,\epsilon-2-TC}$ to the temperature error to the thermocouple measurement. All values are given in [°C].

Measurement	Arduino state	Microcontroller	Oscillator	Board PS (+)
T_{IR}	Inactive	28.9	28.8	29.0
T_{IR}	Operational	37.1	33.0	31.5
ΔT_{IR}	Operational	8.2	4.1	2.5
$\Delta T_{IR,\epsilon=0.95}$	Operational	9.0	4.7	3.0
$\Delta T_{IR,\epsilon-2-TC}$	Operational	-0.1	1.2	0.6

Emissivity calibration

Calibration for the emissivity of the test object is another means to correct IR measurements. Other than the previous method, the technique determines the optical surface properties without modification thereof. This section explains a two-point calibration to obtain an emissivity map of the test item, also referred to as *emissivity mapping* (Vellvehi et al., 2011; Breitenstein et al., 2010; Orlove, 2011).

An emissivity calibration uses the output signal of a thermal IR camera for comparison with a known temperature of a body. Thermal IR cameras measure the incoming IR radiation and convert the measurement into a temperature readout. The conversion occurs by means of a response curve that derives from a blackbody calibration at vacuum conditions (Vellvehi et al., 2011). The available thermal IR camera and ResearchIR software license facilitates only temperature readouts. The software license prohibits accessing the internal calibration curve that relates IR signal to temperature read out. This study, therefore, uses the temperature read out to calibrate for emissivity.

The temperature-based emissivity calibration builds on the assumption that Planck's law is linearizable over small temperature ranges (Vellvehi et al., 2011; Breitenstein et al., 2010; Orlove, 2011). The linearization is valid if Wien's approximation applies, $C_2/(\lambda T_\lambda) >> 1$. Table 12 summarizes Wien's approximation for the LWIR wavelength spectrum and temperatures of interest for this case study. This study assumes that the linearization is sufficient.

Table 12: Overview of Wien's approximation, $C_2/(\lambda T_\lambda) >> 1$, to linearize Plancks's law considering the LWIR spectrum and the temperatures of interest to this study.

	Wavelength λ $[\mu m]$	$T = 25°C$	$T = 85°C$
$C_2/(\lambda T)$	8	6.0	5.0
$C_2/(\lambda T)$	14	3.4	2.8

The linearization yields equation 7, which describes the emissivity (Breitenstein et al., 2010; Orlove, 2011). The superscript *IR* refers to the measured temperature by the IR camera and the subscripts *1* and *2* to reference states of known temperature. A uniform temperature of the test object during calibration is favorable because a single location suffices to measure the absolute temperature, e.g., by using a thermocouple.

$$\epsilon(x,y) = \frac{T_2^{IR}(x,y) - T_2^{IR}(x,y)}{T_2(x,y) - T_1(x,y)} \tag{7}$$

The temperature of a state *3* derives from the emissivity calibration at the reference states *1* and *2*, see equation 8 (Vellvehi et al., 2011; Orlove, 2011; Breitenstein et al., 2010). The equation shows the corrected temperature in relation to the reference state *1*. The second term of the equation shows that the correction includes an image subtraction of the reference state *1*.

$$T_3(x,y) = T_1(x,y) + \frac{1}{\epsilon(x,y)}\left(T_3^{IR}(x,y) - T_1^{IR}(x,y)\right) \tag{8}$$

The emissivity mapping requires to reference states of known temperature. The consideration of reference states with uniform temperature simplifies because one absolute temperature sensor suffices to describe the temperature of the entire body that the IR camera is measuring, i.e., $T_1(x,y) \rightarrow T_1$.

The inactive state of the ArduinoUNO at room temperature is the first reference state. The second reference state is a uniformly heated Arduino using the test set-up in figure 12a. The graph in figure 15a shows the resulting emissivity map. The emissivity map illustrates that both the PCB material and the ATmega16U2 have a high emissivity around $\epsilon = 0.9$, whereas the shiny metallic components show a low emissivity about $\epsilon = 0.3$. The emissivity of the ATmega16U2 aligns with the values for Quad flat no-leads (QFN) packages (Svasta et al., 2004).

The emissivity map corrects the thermal IR image of the ArdunioUNO operation, see figure 15b. The correction achieves alignment between the IR and thermocouple measurements. The residual error is due to the measurement sequence of first heating the Arduino, cooling it down and then operating it. The error is because the ArduinoUNO did not reach the steady-state temperature before the heating when being operated. The temperature map in figure 15b aligns qualitatively with the subtracted image in figure 11b. However, the emissivity mapping fails to entirely remove the in-plane temperature gradients due to the low-emissivity components.

The emissivity calibration achieves accurate temperature measurements, see table 13. However, the low operational temperature increase results in a similar accuracy as the image subtraction in table 10 for the PCB and microcontroller, i.e., the high emissivity components. The benefit of the two-point emissivity correction becomes evident when looking at larger temperature ranges. The graph in figure 16 illustrates that the emissivity correction enables to correct the emissivity error shown at the beginning of this section, see figure 12b for comparison. The alignment between the graphs, moreover, demonstrates that the emissivity of the

ArduinoUNO PCB is constant over a temperature range of $25-45°C$. The constant behavior of the emissivity aligns with the findings by Svasta et al. (2004), which state that temperature variations of PCB material are insignificant.

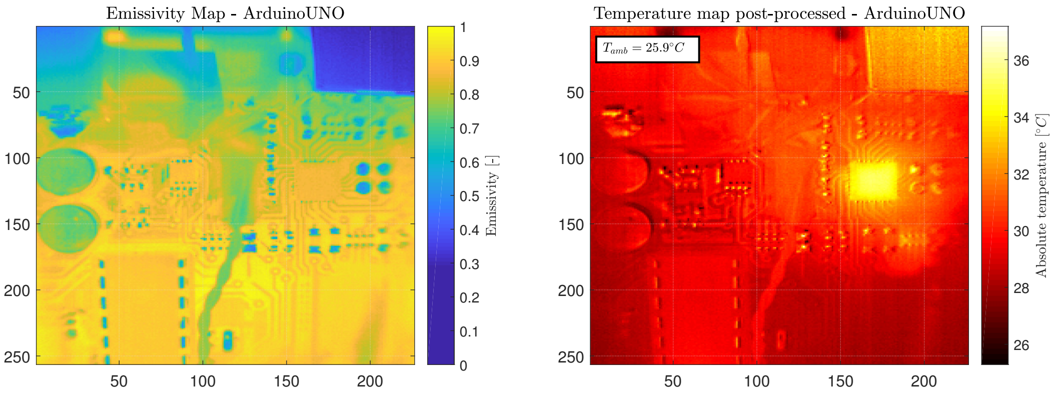

(a) (b)

Figure 15: Emissivity mapping of the Arduino UNO. (a) Emissivity map of the Arduino UNO. (b) Post-processed IR image.

Table 13: Emissivity correction through calibration of the ArduinoUNO emissivity. The parameter $T_{IR,cal.}$ refers to absolute temperature of the calibrated measurement, T_{TC} to the thermocouple measurement and the $\Delta T_{TC-2-IR,cal.}$ to the temperature error between thermocouple and calibrated measurement. The oscillator is covered with a thermocouple and Kapton tape, see figure 15a. The value of the oscillator is, therefore, invalid for comparison with the previous measurements. All values are given in [°C].

Measurement	Arduino state	Microcontroller	Oscillator	Board PS (+)
$T_{IR,cal.}$	Operational	34.98	32.23	28.38
T_{TC}	Operational	34.76	31.71	29.26
$\Delta T_{TC-2-IR,cal.}$	Operational	-0.22	-0.52	0.88

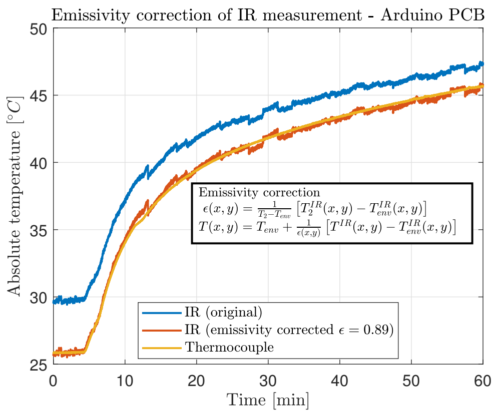

Figure 16: Emissivity correction for the heating of the ArduinoUNO PCB. The emissivity correction removes the temperature error between thermocouple and IR measurement in figure 12b.

3.4.5 Lessons learned – Thermocouple measurement

Thermocouples enable to validate the thermal IR measurements. The previous analysis implicitly assumes that the thermocouples achieve better accuracy. The reason for this assumption is the lower nominal accuracy of thermal IR imaging, see table 6, as well as the inherent uncertainties due to background radiation and emissivity. This section, however, highlights challenges of measuring temperatures with thermocouples, as well as two flaws in the measurement equipment of the cleanroom. Moreover, the section describes the calibration of thermocouples for further testing in this thesis.

LabView script

The LabView environment builds the interface for data logging of the thermocouple measurements. This study uses an existing script on the cleanroom computer that was previously used by other students. Thermocouple measurements require calibration for the cold junction temperature, see explanation above and figure 7b. The existing script uses a manual user input to define a constant cold-junction temperature, currently set to 25°C. The ambient temperature of the thermal test facility, however, varied between $21 - 28°C$ through the test campaigns. Therefore, it is necessary to modify the existing script by setting the cold-junction compensation in the LabView script from `Constant` to `Built-In`. This setting ensures the calibration of the reference junction against the temperature readout of the internal thermistor of the *NI9211* DAQ device (National Instruments, 2015).

Thermocouple wire twisting

The experimental study, moreover, uses the available thermocouples in the cleanroom. At least two of these thermocouples were twisted with the bare thermocouple wires touching, see the image in figure 17. Each contact point of the thermocouple wires creates a new measurement junction.

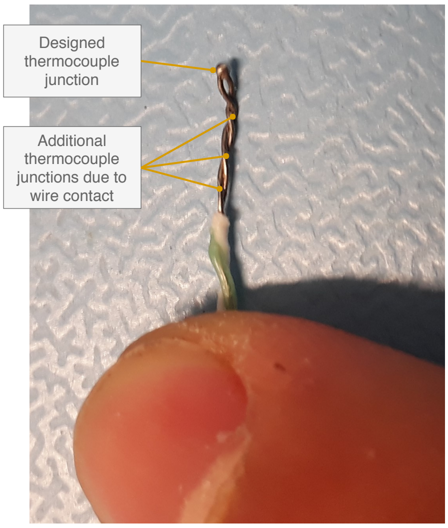

Figure 17: Twisting of the thermocouple wires creates additional thermocouple junctions.

The wrong application of the twisted thermocouple causes measurement errors. The graph in figure 18b illustrates the temperature error when measuring the temperature of the ATmega16U2 microcontroller with the twisted thermocouple in figure 17. The measurement set-up in figure 18a illustrates that the last junction point of the thermocouple is in the air, instead of being on the surface of the chip. The thermocouple, therefore, measures the air temperature instead of the microcontroller temperature. Untwisting the thermocouple removes the measurement error and creates alignment with the IR measurement.

Thermocouple procurement and calibration

The performance characterization in this chapter uses the available thermocouples in the cleanroom. The preparation of further test campaigns in this thesis motivates to procure additional thermocouples, as well as to calibrate them. The digital product information of the *NI9211*

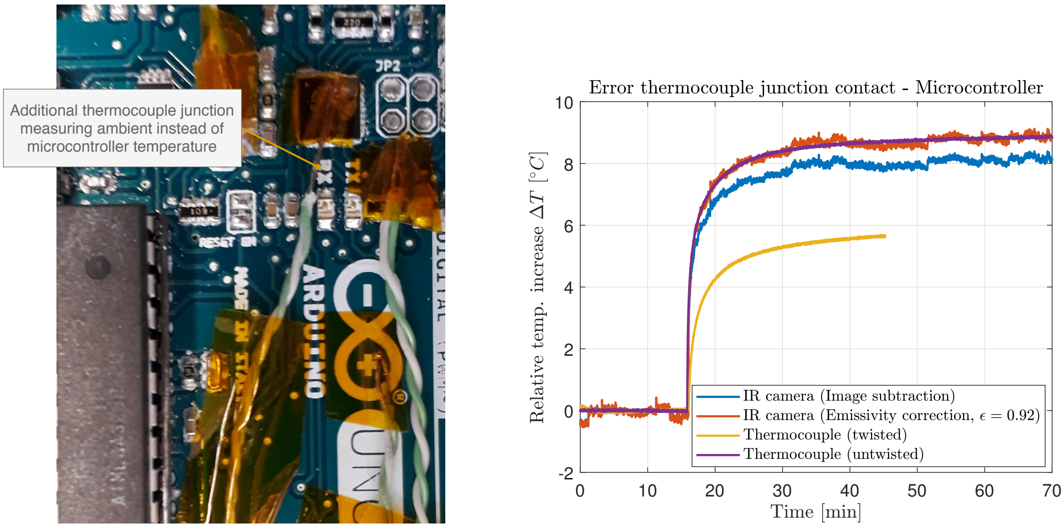

(a) (b)

Figure 18: Incorrect thermocouple application. (a) The additional junctions of the thermocouple in figure 17 measure the ambient air instead of the microcontoller temperature. (b) Temperature error due to errorneous thermocouple application and comparison with IR measurement.

DAQ device shows that its last calibration was in 2011. This subsection describes the calibration process for the thermocouples, which, ultimately, demonstrates that an absolute accuracy of $\pm 0.2K$ is achievable.

The calibration of the thermocouples uses both freezing and boiling water as a reference body. The thermodynamic properties of freezing and boiling water define the absolute temperature. The calibration against water, therefore, alleviates the need for an additional sensor with higher accuracy or a temperature controlled heat source. The temperature range from freezing to boiling water, moreover, covers the expected temperature range for further testing. The images in figure 19a and 19b illustrate the test set-up for the ice bath and boiling water calibration.

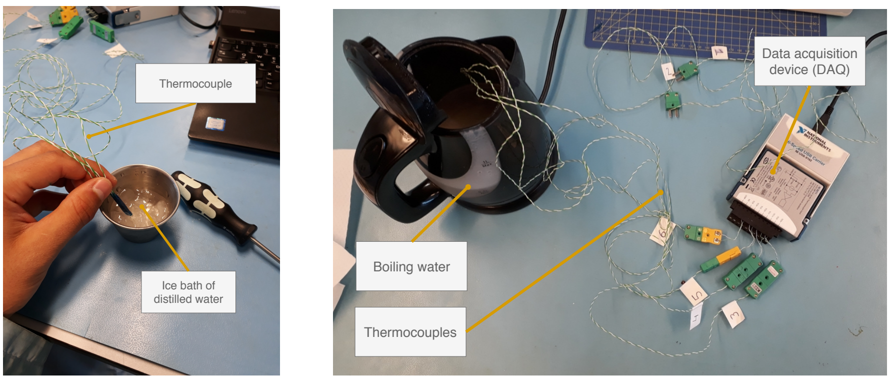

(a) (b)

Figure 19: Test set-up for the calibration of the thermocouples using (a) an ice bath of distilled water and (b) boiling water.

An ice bath contains both liquid and frozen water. This calibration uses distilled water for creating an ice bath. Distilled water provides a stable reference point considering that the salinity of water modifies the freezing point. The temperature plot in figure 20a shows the measured response of the thermocouples to the ice bath. The plot illustrates the measurement stability of the thermocouples and the DAQ device. The sharp peak in the measurement plot results from lifting the thermocouples out of the ice bath. The peak demonstrates the fast response time of the thermocouples. The fast response time, on the other hand, shows that the exposure time to the ice bath is sufficient for calibration.

A calibration with boiling water requires continuous heat supply to sustain the boiling process. The image in figure 19b illustrates the measurement set-up using an ordinary kettle with the ability to supply heat continuously. The boiling point of water depends on the ambient pressure, see the Clausius-Clapeyron relation 9(VDI, 2010). The calibration considers a boiling temperature of $99.97°C$, which accounts for the atmospheric pressure of $1014.0hPa$ during the measurement and an assumed elevation of the laboratory of $10m$. The temperature plot in figure 20b shows the thermocouple response to the boiling water.

$$ln\left(\frac{p}{p_0}\right) = \frac{\Delta H_{vap}}{R}\left(\frac{1}{T_0} - \frac{1}{T}\right) \tag{9}$$

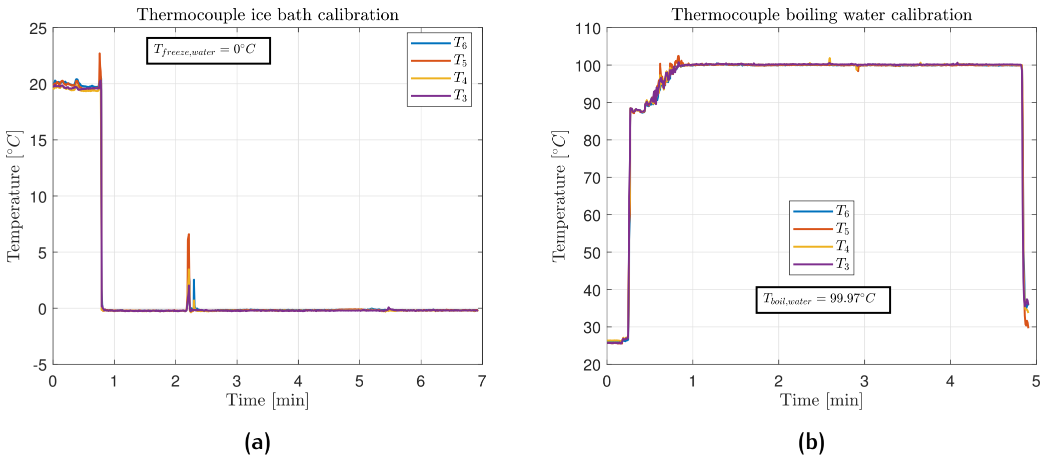

Figure 20: Temperature plot for the (a) ice bath and (b) boiling water calibration of the thermocouples.

Table 14 summarizes the calibration results. The results show that a temprature accuracy of $\pm 0.2K$ is achievable. The thermocouples 3 and 4 repetitively show a larger offset that the other thermocouples, despite random variation of the DAQ channels between the measurement. The other thermocouples will., therefore, be primarily used for further testing.

Table 14: Two-point thermocouple calibration using an ice bath at $0°C$ and boiling water at $99.97°C$. The values show the offset between the thermocouple measurement and the absolute temperature of the source. All values are given in [°C].

Thermocouple ID	Ice bath	Ice bath	Ice bath	Ice bath	Boiling water	Boiling water
1	-0.1224	-	-0.1931	-	-	0.0027
2	-0.0822	-	-0.1800	-	-	-0.0137
3	-0.0890	-0.1470	-0.2558	-0.2063	0.1979	0.1242
4	0.0420	-0.1001	-0.2082	-0.2091	0.1773	0.1596
5	-	-0.0241	-	-0.1798	0.0197	-
6	-	0.0898	-	-0.1641	0.0174	-

3.5 CONCLUSIONS

This chapter describes the performance of thermal IR imaging in comparison with thermocouple measurements. The microcontroller of an ArduinoUNO serves as a case study to evaluate the applicability of thermal IR imaging for electronic components on PocketQube subsystems. This bullet-point list summarizes the major findings of this investigation:

- **LWIR cameras are suitable for temperature screening of PocketQube subsystems.** LWIR cameras achieve similar measurement accuracy as thermocouple measurements in a temperature range from $20 - 45°C$. The theoretical analysis shows that the radiation maxima for the operational temperature range of COTS electronics components coincide with the sampling bandwidth of LWIR cameras. MWIR cameras achieve higher measurement accuracy but are more expensive and suitable for temperatures beyond the upper-temperature limit of COTS electronics components.

- **Thermal IR imaging requires correction for reflected background radiation and emissivity of the target object.** The analytical and experimental analysis highlight that using an IR with default settings results in the temperature measurements. The reflected background radiation provides a constant offset in a laboratory environment with stable illumination conditions. The emissivity of an object yields measurement errors that scale with temperature.

- **The emitted IR radiation by the camera itself contributes most significantly to reflected background radiation.** The thermal IR camera provides the primary heat source for background reflection in test set-up with the camera orientation perpendicular to and the camera positioning over the center of the PCB.

- **Digital image subtraction is the preferred correction technique for room temperature measurements with component temperature increases below $< 10K$.** The ArduinoUNO case study demonstrates that digital image subtraction is a simple technique to correct thermal IR imaging for the undesired background reflection. The subtraction removes apparent thermal hotspots due to the reflection of IR radiation originating from surrounding heat sources. The digital image subtraction yields accurate temperature readouts for high emissivity components with a relative temperature increase lower than $< 10K$.

- **The measurement of component temperature increases beyond 10K requires emissivity correction.** Temperature errors due to emissivity scale with the object temperature. The emissivity mapping technique is suitable to correct for these errors in a temperature range from $25 - 45°C$. The technique requires knowledge about the emissivity of the target object. Calibration is a suitable means to determine emissivity values. However, the calibration requires either additional sensors or a temperature controlled heat source.

- **The emissivity of PCBs and microcontroller packages is high, which makes them suitable targets for thermal IR imaging.** The ArduinoUNO case study shows that the emissivities of microcontroller packages and PCBs are in the order of $\epsilon = 0.92$ and 0.89.

- **Local application of removable, high-emissivity fluids is suitable to measure low-emissivity components.** Accurate IR temperature measurements of low emissivity components are challenging. The application of removable correction fluid to components is a useful technique to measure the temperature of low-emissivity components. The application of the correction fluid is necessary when the temperature gradients on the high-emissivity PCB indicate a thermal hotspot.

- **Thermocouples achieve an absolute measurement accuracy of at least $\pm 0.2K$ at 0 and $100°C$.**

- **Contact points between thermocouple wires result in additional measurement junctions.** Each contact point between bare thermocouple wires provides a new measurement junction that shifts the measurement location accordingly.

- **Thermocouples are relative temperature sensors that require accurate reference calibration.** Precise temperature measurements require calibration of the reference junction temperature. DAQ devices, such as the *NI9211* include absolute temperature sensors for calibration.

4 NATURAL CONVECTION AT SUBATMOSPHERIC PRESSURES

This study investigates both the temperature heating of hotspots between ambient and vacuum conditions and the necessary pressure levels for thermal-vacuum testing of PocketQube subsystems. This chapter, first, investigates analytical approaches to describe natural convection and the conditions under which natural convection vanishes. An experimental test campaign determines the natural convection coefficient at various pressure. The experimental data, then, provides the baseline for a preliminary estimation of the temperature error that results from residual natural convection phenomena compared to ideal vacuum conditions.

Table 15: Vacuum classification according to the National Physics Laboratory (2010) and Jousten (2016)

Vacuum level	Pressure (Pa)	Pressure (mbar)
Ambient	10^5	10^3
Rough	10^5 to 10^2	10^3 to 10^0
Fine	10^2 to 10^{-1}	10^0 to 10^{-3}
High	10^{-1} to 10^{-5}	10^{-3} to 10^{-7}
Extreme-ultra high	$< 10^{-6}$	$< 10^{-8}$

The key test equipment for vacuum testing is the test chamber and the pump. Table 16 lists vacuum pumps used in this study to achieves the previously defined vacuum levels. Figure 21 shows the pressure profile of two of the pumps for a VacuuTherm VT6130 test chamber.

Table 16: Overview of pumping systems that satisfy the vacuum categories shown in table 15. The annotation SSE refers to the attainable pressure in the Vacutherm VT6130 test chamber in the cleanroom of the faculty. The given pressure values derive from the depressurization curves in figure 21. The pricing for the pumps is obtained from (Dijstra Vereenigde, 2018).

Vacuum level	Pump	Attainable pressure [Pa]	Cost [k€]	Availability
Ambient	N/A	10^5	N/A	✓
Rough	Vacuubrand MD1	1.5×10^2 (rated), 2.8×10^5 (SSE)	1.2	✓
Fine	Vacuubrand RZ6	10^0 (rated), 2.1×10^1 (SSE)	2.2	✓
High	Vacuubrand HP40B2	10^{-5} (rated)	7.2	✗

4.1 ANALYTICAL APPROACH

4.1.1 Natural convection heat transfer

Natural convection is a heat transfer mechanism due to fluid motion. The driving mechanism is either inertia or buoyancy forces, the former being referred to as forced and the latter as natural convection. The buoyancy forces in natural convection are a result of temperature-induced density differences.

Natural convection is absent in space for two reasons: First, there is no medium that could accommodate for the necessary fluid motion and, second, buoyancy forces that drive natural convection on Earth are absent in orbit (Martynenko and Khramtsov, 2005).

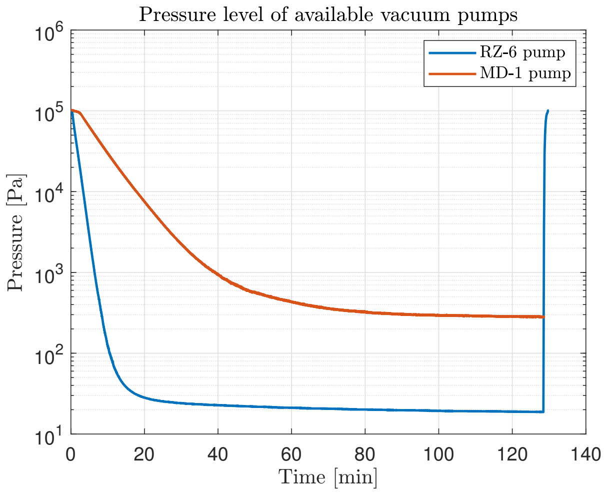

Figure 21: Depressurization of the environmental test chamber over time. The MD-1 pump achieves a steady pressure level of $280Pa$ after two hours, while the RZ-6 pump achieves pressure levels of 21 and $19Pa$ after one and two hours respectively.

4.1.2 Flow regimes - Knudsen number

Natural convection vanishes when a fluid medium rarefies. The state of a fluid from ambient to low pressure can be described as viscous, molecular, or in a transitional state between the two. The viscous flow regime accommodates for fluid motion of the molecules, while in the molecular flow regime molecules move individually without frequent interaction of other molecules. The absence of a fluid motion implies that the effects due to natural convection disappear.

The Knudsen number is a dimensionless parameter defining the flow regime, see categorization of the flow regimes in table 17. The Knudsen number is the ratio between the characteristic length l^* of the geometry and the mean free path l_{mean} of the surrounding medium.

$$Kn = \frac{l^*}{l_{mean}} \qquad\qquad l_{mean} = \frac{k_B T}{\sqrt{2}\pi d_m^2 p} \tag{10}$$

Table 17: Overview of the flow regimes and corresponding Knudsen numbers according to Jousten (2016).

Flow regime	Knudsen number $[-]$
Viscous	$0.01 > Kn$
Transitional	$1 > Kn > 0.01$
Molecular	$Kn > 1$

The mean free path, and thus also the Knudsen number, depends on the thermophysical properties of the fluid. The dependency of the Knudsen number on pressure indicates at which pressure natural convection phenomena vanish. The graph in figure22b illustrates the Knudsen number for various characteristic lengths relevant to PocketQubes, see table 18. The graphs illustrates that the available vacuum pumps provide transitional flow conditions for the relevant characteristic lengths. The transitional regime describes the pressure region, where viscous flows changes to molecular motion and natural convection phenomena vanish. The following analysis of the thermal conductivity of air further supports the hypothesis that natural convection phenomena vanish in the transitional flow regime.

Table 18: Overview characteristic lengths for PocketQubes. All units in $[mm]$.

Side panel (3p)	PQ9 subsystem (vertical)	PQ9 subsystem (horizontal)	Spacers
180	42	10.5	7

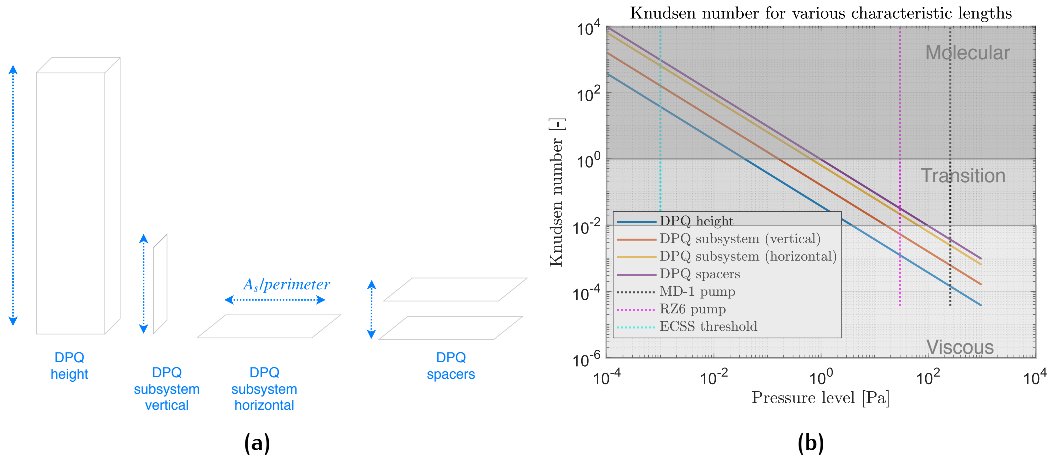

Figure 22: Knudsen numbers and characteristic geometries relevant to PocketQube testing. The characteristic lengths l^* refer to the values given in table 18.

4.1.3 Gas conduction and natural convection heat transfer

Temperature differences between a medium and a surface cause density differences in fluids, which, ultimately, result in gas or fluid motion. A thin fluid/gas layer remains motionless in close vicinity of a surface due to friction forces, also referred to as the no-slip region. The driving motor that, first, establishes this fluid motion and, then, maintains the density differences is heat conduction through the motionless medium. The energy balance over the no-slip region states that the incoming heat due to heat conduction from the surface equals the outgoing enthalpy stream due to the fluid motion (Bejan, 2013; Jousten, 2016).

$$q = -\lambda_{fluid} \frac{\partial T}{\partial y}|_{y=0} = h_{conv} \left(T - T_0 \right) \tag{11}$$

The thermal conductivity of a fluid/gas is constant in the viscous regime and becomes linear dependent on pressure in the molecular regime (VDI, 2010). With the decrease in thermal conductivity of the medium also the gas conduction in the boundary layer reduces removing the driving mechanism for the establishment of a natural convection flow.

Analytical solutions to describe the heat transfer due to gas conduction in the molecular flow regime exist only for simplified cases, such as two infinite plates at distance x_{gap} with a stagnant fluid between them. The relations in table 19 describe the heat transfer due to gas conduction between two parallel plates according to Jousten (2016). An empirical relation describes the heat transfer in the transitional flow regime. Rearranging the empirical relation with the expressions of the molecular and viscous flow regime yields the thermal conductivity as a function of pressure.

$$\lambda_{fluid}(p) = \frac{p\, x_{gap}}{8 \frac{\kappa - 1}{\kappa + 1} \frac{T}{\bar{c} a_E} + \frac{x_{gap}}{\lambda_0} p} \tag{12}$$

The graph in figure 23 shows the thermal conductivity as a function of pressure for various gap size x_{gap}. The graph, moreover, includes grey boxes that indicate the fluid regimes for a horizontal PocketQube subsystem board, see figure 22b. The graph shows that the thermal conductivity decreases as a function of pressure in the transitional flow regime. The behavior

Table 19: Conductive heat transfer through stagnant air between two plates. (Jousten, 2016)

Viscous	Transitional	Molecular
$\dot{Q}_{vis} = \frac{\lambda_{fluid} A}{x_{gap}} (T_2 - T_1)$	$1/\dot{Q} = 1/\dot{Q}_{mol} + 1/\dot{Q}_{vis}$	$\dot{Q}_{mol} = \frac{1}{8} p \bar{c} a_E \frac{\kappa+1}{\kappa-1} \frac{T_2 - T_1}{T}$

of the thermal conductivity supports the prior observation that the natural convection disappears in the transitional flow regime.

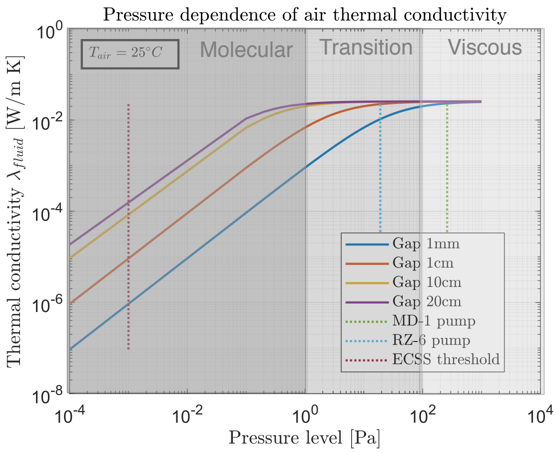

Figure 23: Thermal conductivity of air between two vertical plates at subatmospheric pressures.

4.1.4 Rayleigh number and the ideal gas law

The Knudsen number and thermal conductivity provide an explanation why and at which pressure natural convection phenomena vanish. However, both figures provide limited utility for the engineering application. The primary interest in this research is to quantify the effect of natural convection to predict the temperature increase considering various vacuum regimes and estimate to what extent natural convection is relevant for the testing.

The natural convection coefficient is typically expressed as a function of the dimensionless Nusselt number, $h = f(Nu)$. The literature contains many correlations that describe the Nusselt number as a function of the Rayleigh Ra and Prandtl Pr number, which are functions of the geometry and thermophysical fluid properties.

$$Ra = \frac{g l^* \beta (T_s - T_\infty)}{\nu \alpha} \qquad Nu = f(Ra, Pr) \qquad h_{conv} = \frac{Nu \lambda}{l^*} \tag{13}$$

The Rayleigh number is a function of the thermophysical properties of the fluid. The substitution of the kinematic viscosity $\nu = \mu/\rho$ and the thermal diffussivity $\alpha = \lambda/(\rho\, c_p)$ yields the Rayleigh number as a function of the density $Ra(\rho^2)$. Langebach et al. (2007) propose to combine the expression of the Rayleigh number with the ideal gas law. The ideal gas relates density to pressure and thus the Rayleigh number. The ideal gas retains validity in the viscous regime, only loosing its applicability when the gas rarefies in the molecular flow regime (Theodore, 2011). The dynamic viscosity μ, the specific heat capacity c_p, and the thermal conductivity λ are primarily temperature dependent and pressure independent in the viscous flow regime (VDI, 2010; Theodore, 2011; Jousten, 2016). Moreover, the thermal expansion coefficient β is substituted by $\beta = 1/T$, which is valid for an ideal gas in an isochoric process. The combination of Rayleigh number and ideal gas yields the Rayleigh number as a function of pressure, see equation 14.

$$p = \rho \frac{R}{M} T \qquad \nu = \frac{\mu}{\rho} \qquad \alpha = \frac{\lambda}{c_p \rho} \qquad \beta = \frac{1}{T} \qquad Ra\left(p^2\right) = \frac{g {l^*}^3 (T_s - T_\infty)\, c_p M^2}{\mu \lambda R^2 T_{film}^3} p^2 \tag{14}$$

4.1.5 Validation of the analytical approach

The relationship between Rayleigh number and pressure was used by Langebach et al. (2007) to describe the convective heat transfer in a cylindrical enclosure for a pressure range of $10^2 < p < 10^5 Pa$. However, no other publication using this relationship was found during the research. The remainder of this section validates the previously described approach using experimental data.

Several authors study the natural convection phenomena at subatmospheric pressures for vertical flat plates and horizontal cylinders (Hosseini and Saidi, 2012; Saidi and Abardeh, 2010; Saunders, 1936; Gryzagoridis, 1971). The Rayleigh number depends on the geometry through the characteristic length and is thus applicable to various geometry shapes. The following validation uses empirical formulas found in the literature to describe the natural convection phenomena for the various geometries.

The validation analysis shows that natural convection phenomena can be described in the viscous regime as a function of pressure. However, the analysis shows that the analytical approach fails to provide an accurate estimation in the transitional flow regime. The unsuccessful validation at low pressures provides the baseline motivation for the following section to determine the natural convection coefficient experimentally experimentally.

Vertical flat plate

PocketQube subsystems assimilate flat plates closest among the common geometries, for which empirical relations for the Nusselt number exist. Hosseini and Saidi (2012); Saunders (1936); Gryzagoridis (1971) investigate the effect of low pressure on natural convection over vertical flat plates.

The data plot in figure 24a compares the experimental data by Saunders (1936) with the the analytical approach using Rayleigh number and ideal gas. The analytical approach uses the Nusselt number relation by Schlichting and Gersten (2016), which is valid in a Rayleigh number range of $10 < Ra < 10^8$ (Gryzagoridis, 1971). The graph aligns with the experimental results showing that the relation $Ra(p^2)$ describes the curvature of the experimental results qualitatively. However, the graph in figure 24b illustrates that the relative error between theory and experiments increases at sub-atmospheric pressures.

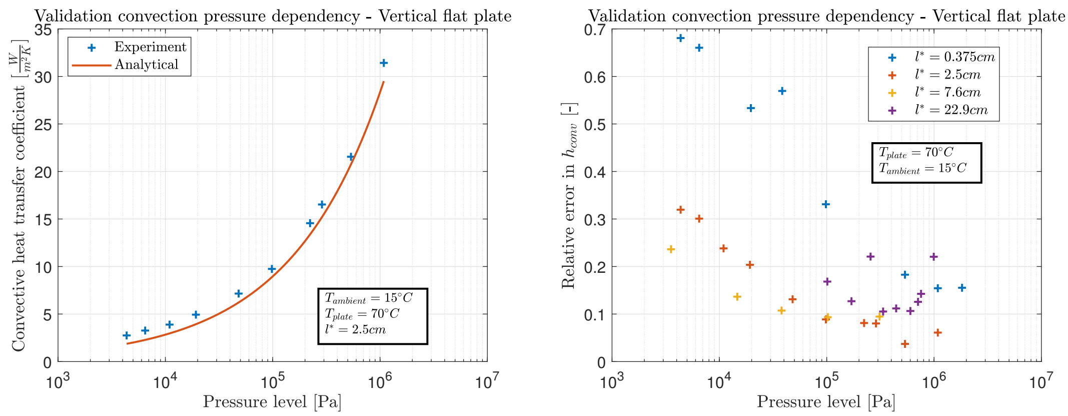

(a) (b)

Figure 24: Validation of the convective heat transfer relation to pressure. (a) Comparison measurement and and analytical approximation for a vertical flat plate. (b) Comparison of the relative error between measurement and analytical approximation for various geometries. Data taken from Saunders (1936).

The previous data set by Saunders (1936) covers pressures in the viscous flow regime. Hosseini et al. (2010) investigate natural convection on a flat plate in the transitional and molecular flow regime. The data plot in figure 25a compares theory and prediction for this dataset. Other than the previous plot in figure 26a, the analytical approximation fails to align with the curvature of the experiments qualitatively. The Rayleigh numbers in this flow regime are below the value, for which Gryzagoridis (1971) considers the empirical correlation applicable. Moreover, the Knudsen number of these measurements indicates that the fluid is in a transitional and molecular state, which limits the applicability of the empirical Nusselt equations.

Hosseini et al. (2010) conclude from the experimental study that natural convection becomes negligible at a pressure of $0.1 Pa$. The previous graph on the thermal conductivity 23 shows that a pressure of $0.1 Pa$ corresponds to a one- and two-order of magnitude change in thermal conductivity for air gaps of 10 and $1 mm$. The observation by Hosseini et al. (2010) supports the hypothesis that natural convection disappears with the reduction in the thermal conductivity of air.

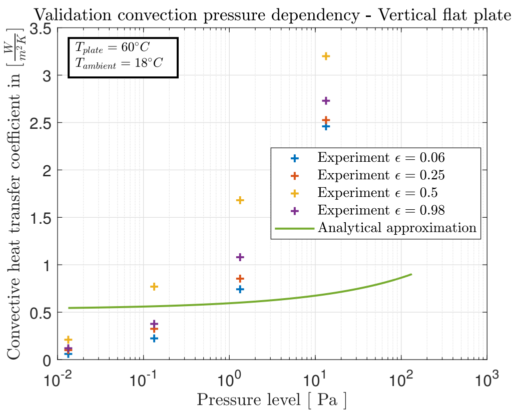

(a)

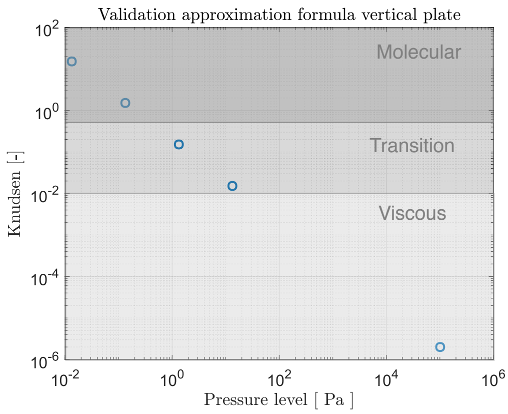

(b)

Figure 25: Validation of the analytical approach for vertical convection case (a) Comparison between the analytical computation of the convective heat transfer coefficient and the experimental results obtained by Hosseini et al. (2010) and (b) Knudsen number for the experimental test points. The letter ϵ refers to the emissivity of the test object.

Horizontal cylinder

Hosseini and Saidi (2012) and Saidi and Abardeh (2010) determine the convective heat transfer coefficient for a horizontal cylinder at subatmospheric pressures. The data plot in figure 26a compares the experimental results for a test item temperature of $100°C$ to an analytical approach using the correlation by Morgan (1975). The qualitative alignment between the experimental data and the analytical approximation shows that the Rayleigh-pressure relation describes the convective heat transfer coefficient qualitatively. The relative error between experiment and analytical calculation increases with decreasing pressure, see scatter plot in figure 26b. The lowest pressure of the measurements is in the transitional flow regime, which explains the comparatively large error.

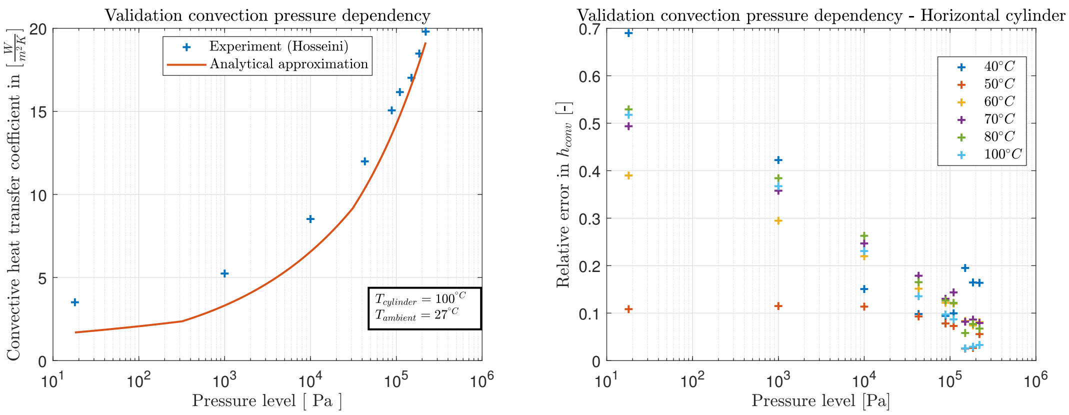

(a) (b)

Figure 26: Validation of the convective heat transfer relation to pressure. (a) Comparison measurement and and analytical approximation for a cylinder temperature of 100°C. (b) Relative error in the convective heat transfer coefficient. Data taken from Saidi and Abardeh (2010); Hosseini and Saidi (2012).

4.2 EXPERIMENTAL APPROACH

The analaytical approach using Rayleigh number and ideal gas yields comparatively large errors in the vicinity of the transitional flow regime. Moreover, experimental data for the natural convection coefficient at the pressures of interest to this study could not be found. Both circumstance motivate performing an experiment to characterize the natural convection for a PocketQube subsystem geometry and at the pressures listed in table 16

4.2.1 Experimental set-up

The test object consists of two copper plate with a heater foil and thermocouples in between, see illustration in figure 27b. The power supply cables of the heater foil provide both electrical energy and act as suspension wires to position the object in the test chamber. The image in figure 27a illustrates the experimental set-up with the test object hanging in the vacuum chamber.

The test sequence consists of heating the test item to a steady-state temperature and switch off the power supply, such that the test item cools down through natural convection and radiation. The transient heat balances of the cooling process results in the following expression, see equation 15. The heat balance implies isothermal surface properties of the test object because of the thermal conductivity of copper. The subscript ∞ refers to the temperature of the test chamber. The analysis assumes that the wall is at the same temperature as the air in close vicinity to the wall.

$$h_{conv}(T) = \frac{mc_p|\frac{\mathrm{d}T}{\mathrm{d}t}| - \epsilon\sigma A(T^4 - T_\infty^4) - \dot{Q}_{cable}\,(T)}{A(T - T_\infty)} \tag{15}$$

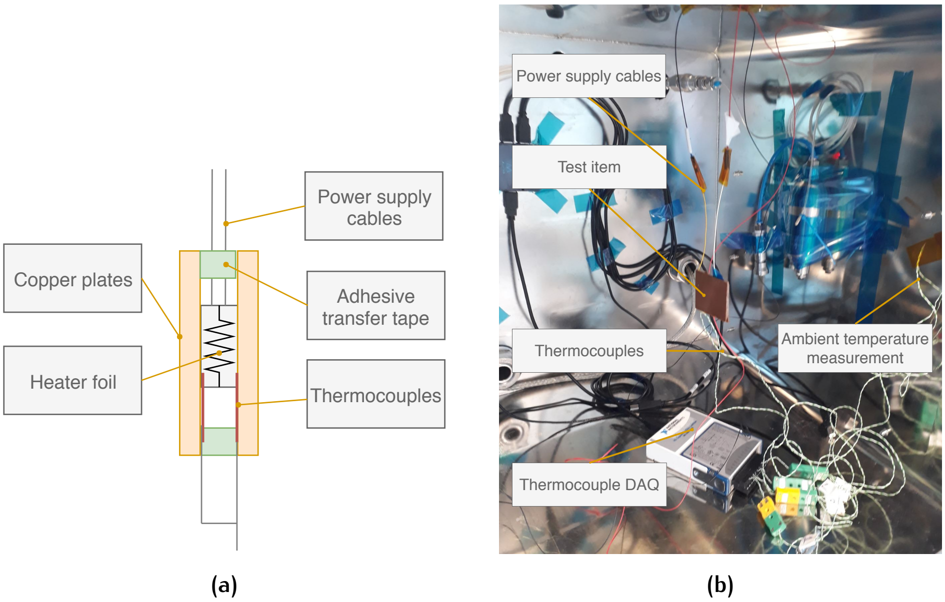

Figure 27: The experimental set-up for the characterization of the natural convection heat transfer coefficient at vacuum pressures. (a) schematic of the test item and (b) test item in the experimental test facility.

4.2.2 Emissivity calibration and conductive heat loss characterization

Equation 15 includes the emissivity, ϵ, of the test object and the conductive heat loss through the power supply cables $\dot{Q}_{cable}$. The graph in figure 28b. The image in figure 28b illustrates the experimental test set-up to determine the conductive heat loss through the power supply cables. The IR image in figure 28b shows temperature of the cables when heating the test object. The section A in the appendix includes the graphs describing the conductive heat loss.

The emissivity calibration uses the same set-up but with the camera shifted. The calibration yields a copper emissivity of $\epsilon = 0.08$, which aligns with the literature (Gilmore, 2002).

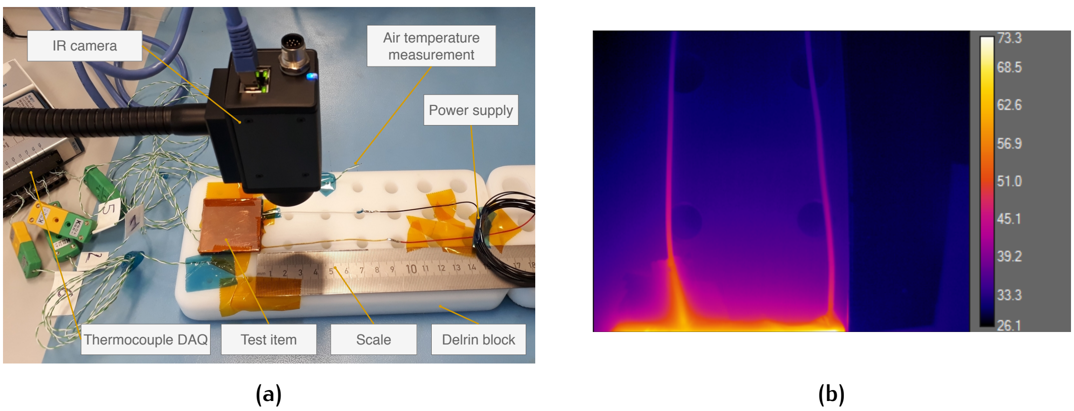

Figure 28: IR camera measurement to calibrate the emissivity of the test item and determine the conductive heat loss through the cabling. (a) Experimental test set-up and (b) IR image of the power supply cables including IR measurement points

4.2.3 Results

The temperature plots in figure 29a illustrate the cooling process of the test object at various pressures. The temperature curves yield the convective heat transfer coefficients shown in figure 29b. The graph of $280Pa$ is starting with an offset because the experiment was interrupted before reaching the ambient temperature during the measurement.

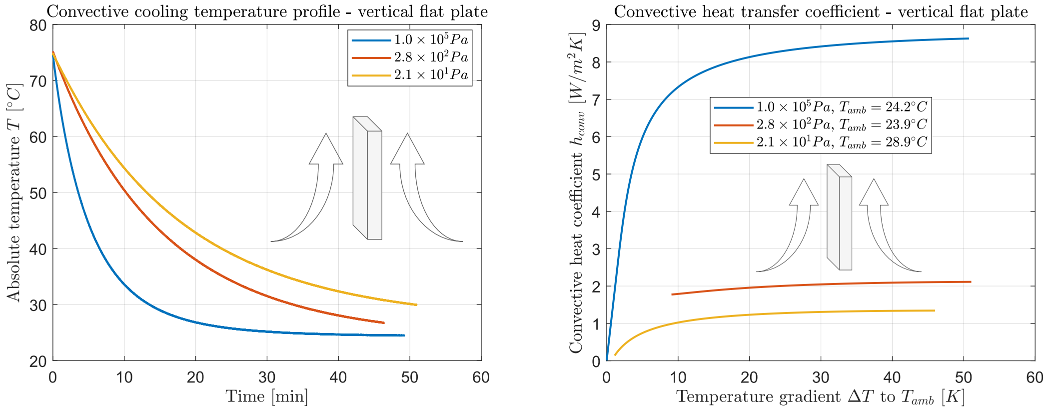

(a) (b)

Figure 29: Experimental determination of the natural convection heat transfer coefficient at ambient pressure, as well as in rough and fine vacuum, considering an isothermal surface with the footprint of a PocketQube subsystem. (a) Experimental cooling curve of the test item. (b) Resulting natural heat transfer coefficient graphs.

4.3 NATURAL CONVECTION EFFECTS ON POCKETQUBE SUBSYSTEMS

The experimental data enable to study the temperature error that results from residual natural convection phenomena at low pressures. A description of the temperature error provides a starting point to choose appropriate pressure levels for thermal-vacuum testing of PocketQube subsystems.

Natural convection provides additional paths for heat sinking. Equation 16 describes the steady-state heat balance for an isothermal subsystem board subject to convection and radiation, whereas equation 17 considers radiation only. The formulas take into account that the presence of natural convection yields a temperature difference ΔT to the radiation only case. The equations enable to perform a preliminary estimation of the thermal behavior of PocketQube boards at subatmospheric pressures. The appendix A explains why the single-node heat balance suffices in first order to describe a PocketQube subsystem board arguing from the Biot number.

$$\dot{Q}_{dis} = \epsilon \sigma A \left(T^4 - T_{Amb}^4\right) + h_{conv}(T, p) A \left(T - T_{Amb}\right) \tag{16}$$

$$\dot{Q}_{dis} = \epsilon \sigma A \left((T + \Delta T)^4 - T_{Amb}^4\right) \tag{17}$$

This study assumes a maximum heat dissipation on a PocketQube subsystem of $\dot{Q}_{dis} = 2W$. This estimate derives from the expected $10W$ power limit for future 3p PocketQubes (Bouwmeester et al., 2018). The maximum dissipation per subsystem is assumed to be 20% of the total available budget following the budgeting that Speretta et al. (2016) describe for the Delfi-PQ communication system.

The single-node heat balance yields the steady-state temperature profiles in figure 30a. The vacuum case, as expected, shows the highest temperature increase with power input. The temperature difference relative to the natural convection cases scales with the magnitude of the convective heat transfer coefficient.

The temperature difference between the graphs in figure 30a corresponds to the error of performing vacuum testing at higher pressure levels than ideal vacuum. The plots in figure 30b show the temperature error between the ideal and imperfect vacuum conditions.

Ideally, the pressure level suppresses natural convection to such an extent that the temperature error remains below the noise limit of the measurement equipment. However, the vacuum quality typically determines the cost of the necessary equipment, see the pump prices in table 16. The test objective typically allows defining a temperature error that is acceptable to fulfill the objective while minimizing cost. The fine vacuum regime results in temperature errors below the example $\pm 8K$ thermal model correlation threshold. The small temperature errors illustrate the suitability of the fine vacuum regime for thermal-vacuum testing of PocketQube subsystems and motivate analyzing the temperature error further.

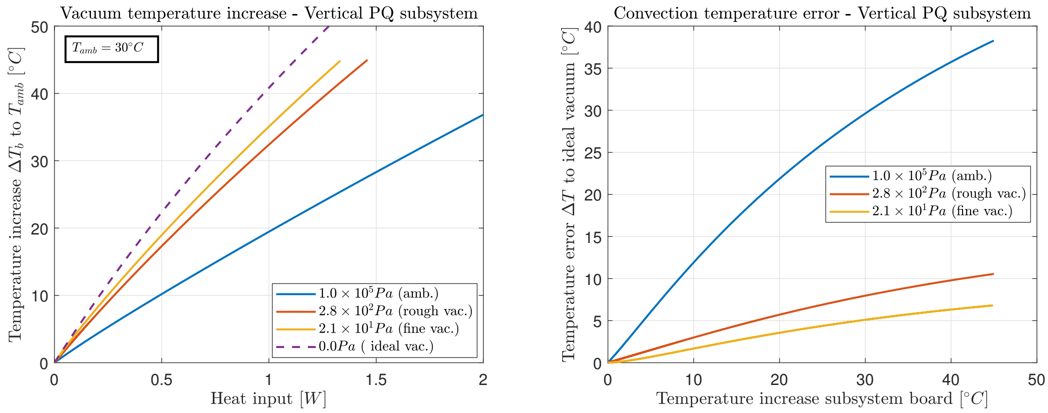

(a) (b)

Figure 30: Heating characteristics of PocketQube subsystems as a function of pressure. (a) Temperature increase of a PocketQube subsystem with isothermal surface properties at various ambient pressures. (b) Temperature difference relative to ideal vacuum conditions.

4.4 CONCLUSIONS

This chapter investigates natural convection phenomena at subatmospheric pressures. The following bullet point list summarizes the major findings:

- **The combination of the Rayleigh number, ideal gas law, and empirical relations describes the natural convection heat transfer at subatmospheric pressure in the viscous flow regime.** The validation of the Rayleigh-pressure relation, see equation 14, describe the natural convection heat transfer coefficient for vertical flat plates and horizontal cylinders with a relative error below 50% in the viscous flow regime ($Kn < 0.01$).

- **The natural convection coefficient for a vertical flat plate in the fine vacuum regime ($21Pa$) is more than eight times lower compared to atmospheric conditions.** The experimental test campaign shows that the natural convection heat transfer coefficient decreases significantly between ambient and fine vacuum conditions. The residual gas in the fine vacuum provides an additional heat transfer coefficient compared to ideal vacuum conditions.

- **The conceptual single-node analysis shows that thermal-vacuum testing in the fine vacuum regime ($21Pa$) yields temperature errors below $8K$ compared to ideal vacuum conditions.** The temperature error between fine and ideal vacuum conditions is small, particularly for subsystem power dissipations below $0.5W$ ($< 5K$). The low temperature error makes the fine vacuum regime a suitable application domain for thermal-vacuum testing of PocketQube subsystems.

5 THERMAL BEHAVIOR OF POCKETQUBE SUBSYSTEMS

The design of thermal control solutions requires to understand the thermal behavior of the object of interest. This chapter investigates the thermal behavior of PocketQube subsystem boards both in its interaction with other subsystems and of the boards themselves. The schematic in figure 31 shows the analysis sequence corresponding to an increasing level of detail in the assembly. The outcomes of this analysis provide a starting point for the design of representative PocketQube subsystem boards to support of the proposed thermal screening methodology.

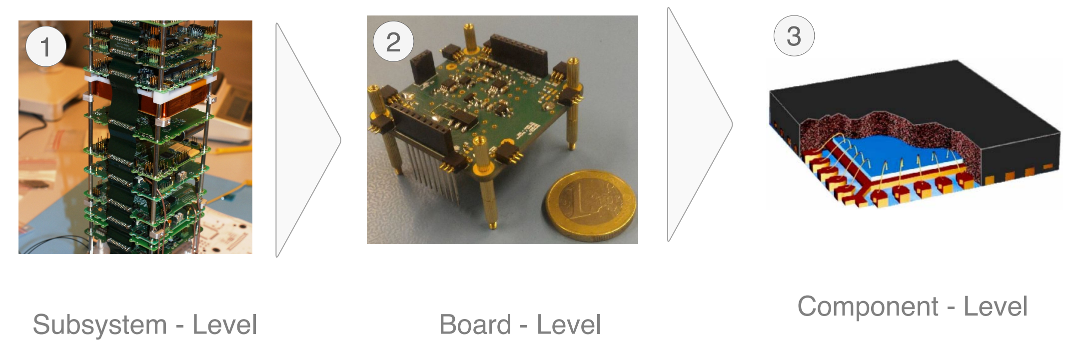

Figure 31: Three levels of analysis that this chapter is looking at to determine the relevant thermal conductances and resistances for PocketQubes. Images are taken from Bouwmeester et al. (2017); DelfiSpace (2016); Mortan and Wright (2004).

5.1 THERMAL RESISTANCE ANALOGY – MODELLING APPROACH

The thermal resistance analysis is a methodology to describe heat transfer similar to the network analysis of electronic circuits. The analogy implies that popular network formulas for electronic circuits are applicable to thermal design.

The thermal network analogy includes thermal resistances, R, and conductances, C, to describe the heat transfer. The heat flow between two points, $\dot{Q}$, is the conductance, C, times the temperature gradient between the two points, ΔT.

$$\dot{Q} = C\Delta T = (1/R)\,\Delta T \tag{18}$$

The heat transfer scales linearly with the conductance and inversely with the resistance. The linear relationship between heat flow and conductance makes interpreting the thermal behavior more intuitive because a higher conductance yields a higher heat transfer. The analysis in this chapter computes the heat flow paths using the thermal resistance but presents the results using the thermal conductance.

Heat transfer occurs through conduction, convection, and radiation. Both the conductive and convective heat transfer are linearly dependent on temperature gradients between two objects, whereas the radiative heat transfer scales with the difference of the temperatures to the fourth power. The thermal resistance analogy requires, therefore, to either linearize the radiative or conductive and convective heat transfer. This study linearizes the radiative heat transfer, which yields the following thermal resistances:

$$R_{cond} = \frac{l}{\lambda A} \qquad R_{conv} = \frac{1}{h_{conv} A} \qquad R_{rad} = \frac{1}{4\sigma\epsilon B_{12} A \left(T_2^2 + T_1^2\right)\left(T_1 + T_2\right)} \tag{19}$$

5.2 SUBSYSTEM-LEVEL HEAT TRANSFER

The interior of PocketQubes consists of PCB-based subsystems board. The most popular arrangement of the subsystem boards is in stacking the subsystems on top of each other (Kovács and Józsa, 2018; Speretta et al., 2016; Bouwmeester et al., 2017).

In the stacking architecture, subsystem boards interact thermally with the adjacent boards above and below. Moreover, subsystems exchange heat with the structure that encloses the internal stack and builds the interface to the space environment. The schematic in figure 32a describes the thermal interaction between two adjacent subsystem boards and the enclosure, represented in the schematic by a single rectangle. The image shows a representative PocketQube subsystem board and labels the relevant components for subsystem-level heat transfer.

5.2.1 Thermal resistance model

The thermal resistance network in figure 32a formalizes the schematic in figure 32a. The thermal resistance network is identical when considering an adjacent subsystem above or below a subsystem board. The geometric and optical surface parameters change, but the network remains similar. The subsystem-level analysis, therefore, considers the interaction of a subsystem with the adjacent subsystems separately using a single compartment, as shown in the schematic in figure 32a.

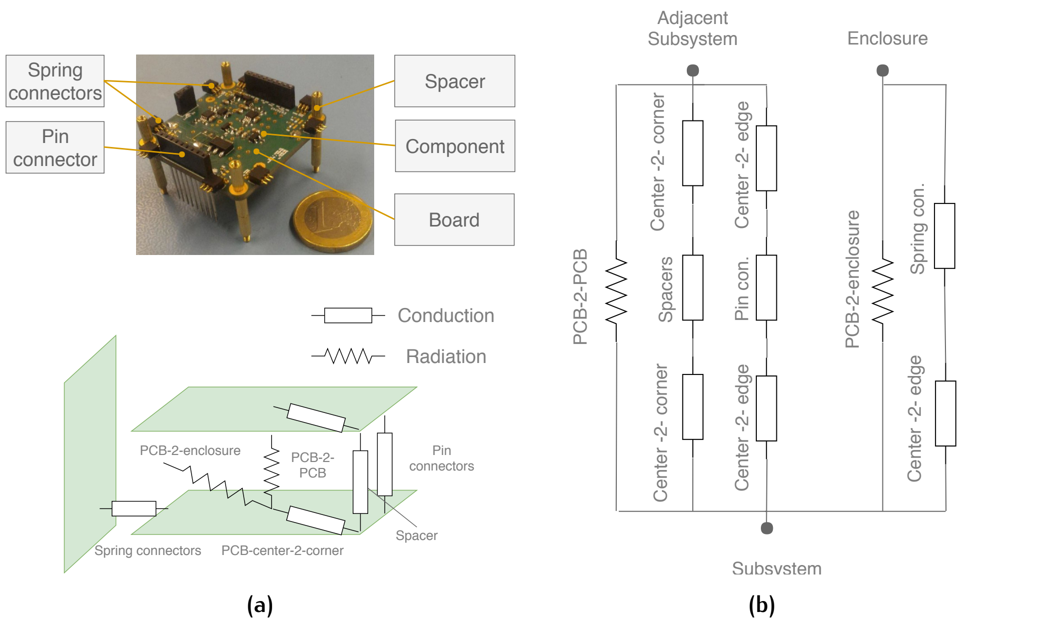

Figure 32: Thermal resistances of a Pocket subsystem stack. (a) Schematic of the subsystem-level heat transfer. (b) Equivalent thermal nodel network.

The nodal network in figure 32b represents the subsystem boards by a single thermal node. This assumption implies that the subsystem mass is concentrated in a single node (Gilmore, 2002), which simplifies the analysis.

The Biot number compares the magnitude of the conductive heat transfer within a subsystem board with the radiative heat sinking from the surface. The dimensionless number provides an estimate if the single node assumption is appropriate in first order, see further explanation in appendix A. The Biot number shows a value significantly smaller than unity when assuming a high radiative heat transfer, i.e., a temperature gradient of $100K$ between subsystem board and environment for a four-layer PCB with PQ9 footprint. The low Biot number indicates that the single node assumption suffices in first-order.

$$Bi = h_{rad} / \left(\lambda_{\parallel} / l^{*} \right) = 0.01 << 1 \tag{20}$$

5.2.2 Radiation between subsystems

PocketQube subsystems exchange heat via radiation. The primary building block for subsystem boards and enclosure are PCBs. The IR calibration of the ArduinoUNO yields a PCB emissivity of $\epsilon = 0.9$. An emissivity lower than unity implies that a fraction of the emitted IR radiation in the satellite interior experience multiple reflections. The Gebhart factor describes the radiative heat exchange between two surfaces considering multiple reflections of the IR radiation. The analysis assumes that all surfaces are gray bodies, which simplifies the radiative calculations.

$$B_{ij} = F_{ij}\epsilon_j + \sum_{k=1}^{n} (1 - \epsilon_k)\, F_{ik} B_{kj} \qquad \sum_{j=1}^{n} B_{ij} = 1 \tag{21}$$

The internal geometry of PocketQubes consist of rectangular box compartments, see CAD model of the subsystem assembly in figure 33a. PocketQube subsystem boards employ flat electronics components. Therefore, the subsystem boards are, in first-order order, flat surfaces when omitting larger components including the batteries, attitude control hardware or payloads. Moreover, the radiative analysis neglects the presence of the spaces and pin connectors. The assumption is reasonable considering that the surface area of enclosing side walls and subsystem is more than seven times larger than the exposed surface area of the spacers.

The standard geometries simply the computation of the radiative heat exchange. The literature contains analytical relations to describe the view factors, F_{ij}, which omits the necessity of using ray-tracing methods (ECSS, 2011).

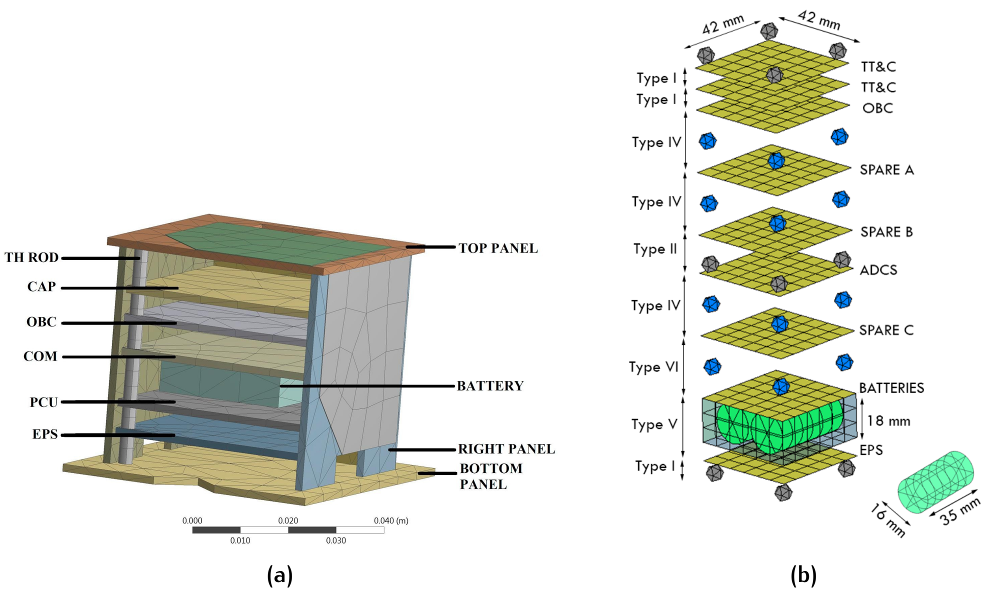

Figure 33: PocketQube subsystem breakdown of (a) the SMOG-1 (1p) and (b) the Delfi-PQ (3p). Images are taken from Kovács and Józsa (2018) and Avila de Luis (2018).

The computation of the linearized, radiative resistance requires the temperatures of the two nodes that exchange heat. As of November 2018, only a handful of PocketQubes has been flying in space, such that thermal flight data are rare. This analysis, therefore, considers thermal simulation data from the SMOG-1 (Kovács and Józsa, 2018) and Delfi-PQ (Avila de Luis, 2018) as a reference for temperatures to compute the radiative heat exchange for PocketQubes subsystems.

The maximum and minimum radiative heat transfer occur on the hot and cold side of the temperature spectrum. Table 20 summarizes the temperature conditions for both satellites that result in the maximum and minimum radiative heat transfer. The abbreviations in the table refer to the subsystem breakdown in figure 33a and 33b. The temperature of the enclosure is the mean temperature of the enclosing side walls considering that both satellites have limited attitude control resulting in rotational motions of 1 (SMOG-1 (Kovács and Józsa, 2018)) and 5 (Delfi-PQ (Boerci, 2016)) revolutions per minute.

Table 20: Temperature inputs to radiative resistance analysis in [°C]. The abbreviations refer to the SMOG-1 subsystem breakdown in figure 33a. Data taken from Kovács and Józsa (2018) and Avila de Luis (2018).

Satellite	Case	Type	Subsystem	Adjacent Board	Enclosure
SMOG-1	A	Hot	16 (CAP)	24.3 (Top)	13.1
SMOG-1	B	Cold	−13.6 (EPS)	−30 (Bottom)	−21.2
Delfi-PQ	A	Hot	40.3 (TTC - low)	42.9 (TTC - high)	45 (mean)
Delfi-PQ	B	Cold	-20.1 (-Z)	11.8 (EPS)	-20 (mean)

5.2.3 Conduction between subsystems

Conductive heat exchange between subsystems occurs through the spacers and pin connectors. The conductive paths include three thermal resistances in series, see the nodal network in figure 32b. This subsection describes the derivation of these conductive resistances for the following components:

- Resistance of the board.
- Resistance of the spacers.
- Resistance of the pin connectors.

Resistance of the board

The conductive path between two subsystem nodes includes conduction through the board. The conduction through the board depends on both the geometry and the layout of the board.

The in-plane thermal conductivity, $\lambda_{\parallel}$, of both FR4 and copper is isotropic (Graebner and Azar, 1997; Gurrum et al., 2011). Graebner and Azar (1997) show that thermal conductivity of PCBs depends only on the number of continuous copper and FR4 layers. The symmetry in geometry and the thermal properties implies that the thermal resistance from the center to the corners is equal for all four corners.

The heat spreading through the board is two-dimensional. The determination of the thermal resistance requires the use of a nodal network solver an analytical solutions to describe the two-dimensional heat spreading for the rectangular geometry could not be found. The schematic in figure 34a explains how to derive the equivalent thermal resistance from the nodal network. The methodology includes the application of a constant heat load, $\dot{Q}$, in the center of the board. The temperature gradient, ΔT, between the center and the corners with constant temperature determines the equivalent thermal resistance, $R = \Delta T / \dot{Q}$. The graph in figure 34b shows the equivalent conductance as a function of the number of continuous copper planes.

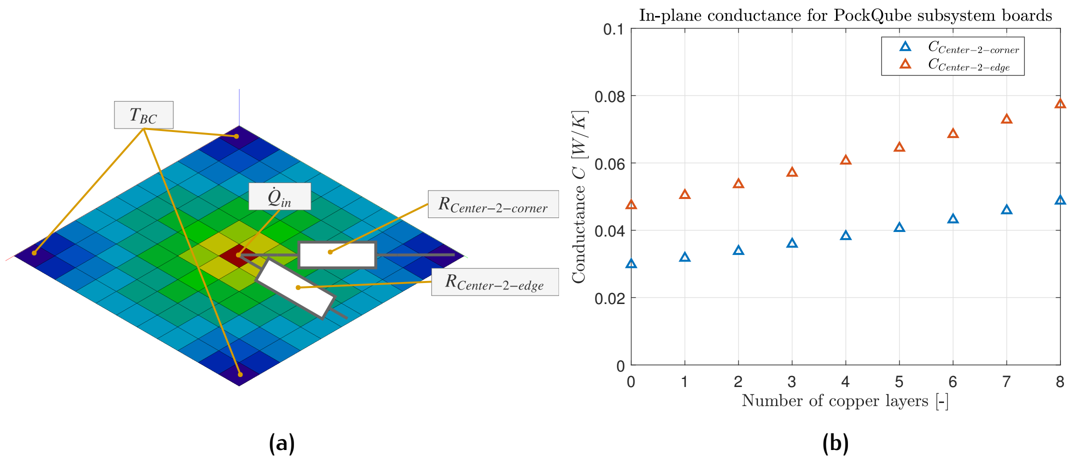

Figure 34: Conductive resistance through PCBs. (a) Modeling schematic to determine the equivalent thermal resistance. (b) Conductive resistance of PocketQube subsystems boards as a function of the number of continuous copper layers.

Spacers

The spacers build the structural interface between adjacent subsystem boards. The spacers are hollow aluminum cylinders, other than the design shown in figure 32b. The thermal resistance of the spacers is a series resistance of two contact resistances and the conductive resistance of the spacer.

$$R_{spacers} = \frac{R_{spacer}}{n_{spacers}} \qquad R_{spacer} = R_{contact} + \frac{l_{spacer}}{\lambda_{Al} A_{spacer}} + R_{contact} \tag{22}$$

The contact resistance between two bodies is a result of surface roughness and geometric inhomogeneities (Gluck and Baturkin, 2002). The inhomogeneities provide that the actual contact area is smaller than the geometrical footprint. Heat exchange in the microscopic gaps occurs through radiation, which is smaller than conduction through an equivalent material. The graph in figure 35 shows the the coefficient of contact conductance, $h_{contact}$, as a function of the contact pressure between the two bodies. This analysis assumes an aluminum-aluminum interface under vacuum conditions, corresponding to graph 1 in figure 35. This analysis assumes a contact pressure of $10kPa$, which is the smallest value in the graph and five times the pressure that the contact experiences due to the dead weight of a four-layer PCB.

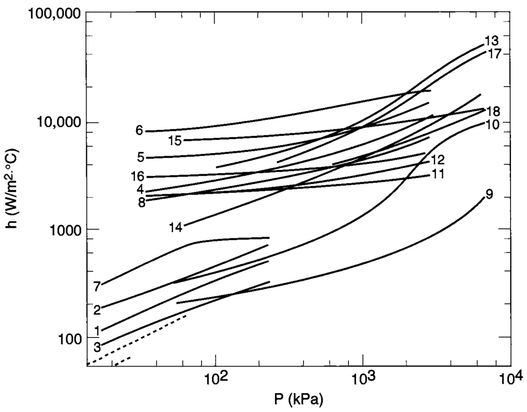

Figure 35: Contact conductance for various materials as a function of the contact pressure. Image taken from Gluck and Baturkin (2002)

Threaded M2 rods provide structural guidance for the assembly of the subsystem boards and hollow spacers, see image in figure 1a. The length of the rods spans from the bottom to the top of the satellite. Nuts and threaded aluminum frames enable to fasten the rods at the bottom and top. The threaded rods have a small contact area and low contact pressure with the internal subsystem boards. The analysis, therefore, neglects the conductive heat transfer through the rods.

Pin connectors

The pin connectors provide the electrical interface between two adjacent subsystem boards. The PQ9 standard describes nine individual pins for the connectors (Radu et al., 2018).

The connector pins consist of a polymer socket and bronze pins, see the image of the subsystem board in figure 32a. The low thermal conductivity of polymers (Han and Fina, 2011) in comparison to bronze (ECSS, 2004) justifies neglecting the sockets for the conductive analysis.

The thermal resistance through the pins is a series of a conductive and two contact resistances, like for the spacers. The contact resistance of bronze, however, is unknown. Van Boxtel (2015) determines the thermal conduction through a *PC104* connector experimentally. The experimental results of Van Boxtel (2015) enable to deduce the contact resistance using the equation 23.

$$R_{pins} = \frac{R_{pin}}{n_{pins}} \qquad R_{pin} = 2R_{contact} + R_{pin} = \frac{2}{h_{contact}A_{pin}} + \frac{l_{pin}}{\lambda_{Bronze}A_{pin}} \tag{23}$$

The derivation of a pin's contact conductance uses the conductance value, for which Van Boxtel (2015) reports the highest measurement accuracy, $R_{pins} = 1/0.26\,K/W$. A visual inspection of the test material shows that the used pin connectors include 52 individual pins with a $8 \times 8mm^2$ footprint and $12mm$ length. These geometry parameters yield a contact coefficient of $154\,W/m^2K$.

The power supply subsystem includes eight spring connectors, as shown in figure 32b. The thermal resistance of the spring connectors is equivalent to the pin connector but with an assumed length of $5mm$.

5.2.4 Results

The comparison between conductive and radiative heat transfer shows that radiation accounts for more than 70% of the overall heat transfer on a subsystem level, see comparison in figure 36. The majority of the radiative heat transfer occurs between adjacent subsystems. The importance of radiation indicates that changes in the optical surface properties will impact the subsystem-level thermal behavior the most. The results builds the baseline for designing thermal control solutions to either retain or reject heat on a from a subsystem board.

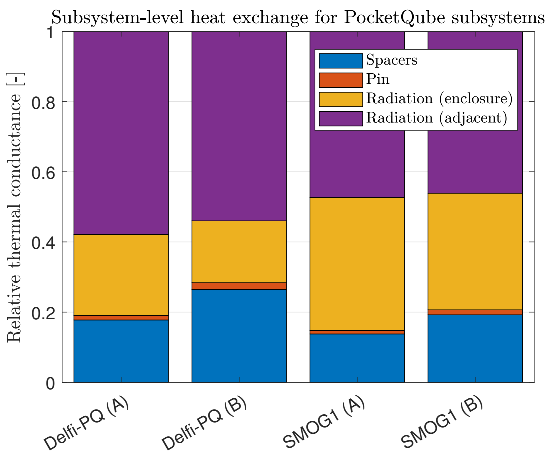

Figure 36: Relative thermal conductances for the Delfi-PQ and SMOG-1 considering operational worst-case temperatures described in table 20.

5.3 BOARD-LEVEL THERMAL HEAT TRANSFER

PCBs are the basic building block for PocketQube subsystems. The PCBs provide the electrical and communication interface to the components. PCBs are a composite of FR4 epoxy laminate and copper. FR4 is is both electrically and thermally insulating, whereas copper shows the opposite characteristics. The thermal conductivity of copper (Gilmore, 2002) is by four orders of magnitude larger than of FR4 (Graebner and Azar, 1997). The difference in thermal conductivity implies that copper is a significant factor for the thermal behavior of PCBs.

This section investigates the impact of the board-level design characteristics on the thermal behavior. The analysis focuses on design parameters related to the amount of copper in a board. The approach uses again the resistance analogy to describe conduction through a board. The thermal resistance network is then summarized to an equivalent board conductance using the electrical network formulas. The outcome of this study build the input to the following chapters, which investigate board-level design solutions further. The analysis considers the following PCB layout characteristics:

- The number of copper layers.
- The location of the continuous copper planes.
- The number of copper traces connecting components on the board.
- The geometrical parameters of the trace, i.e., thickness and width.
- The number of VIAs providing a vertical link through the subsystem.

5.3.1 Thermal resistance model

Determining the equivalent thermal conductance of a subsystem board requires several modelling assumptions. Two assumptions simplify the nodal network to perform a quick, comparative analysis of the PCB characteristics. First, the analysis omits considering radiative heat sinking from the board's surface. Second, the analysis describes the out-of-plane heat transfer by an equivalent resistance $R_{\perp}$, compare the network schemes in figure 37a and 37b.

PocketQube subsystems are built on flat PCBs with components mounted on the surface (Radu et al., 2018), see the image of a representative subsystem board in figure 32a. The flat shape of the PCBs implies that heat transfer over the board occurs solely through conduction. Moreover, the view factor between surface mount electronics components is negligible considering the small exposed surfaces. The analysis, therefore, focuses on conduction to describe the board-level heat transfer.

Exceptions to the previous assumption about small view factors are larger components, such as magnetic coils, batteries, or payload components. The geometric shape of these component provides view factor between these components is considerable. The proposed methodology focuses on detecting thermal hotspots, which are expected to occur electronics components with higher power density. Therefore, the analysis avoids considering the board-level heat exchange for the larger subsystem components, which require more detailed thermal modeling to determine radiative heat exchange factors.

Dissipated power on a hotspot will conduct to the board and eventually sink from the surface through radiation, see the nodal network in figure 36. Nodal discretization is necessary to describe the simultaneous conductive heat spreading and radiative heat sinking. The required level of detail is high for a preliminary investigation of the board-level design characteristics. Instead, the analysis omits describing the radiative heat sinking and focuses on conduction through the board.

resistances of the simplified and multi-node model the analysis and summarize conductive paths.

Dissipated heat spreads simultaneously in the in- and out-of-plane direction of a board, see nodal network in figure 37a. The high conductivity of copper implies that heat will predominantly flow along the copper paths. Therefore, in-plane heat spreading dominates over the out-of-plane when considering a single-layer board with a continuous copper plane on top. The dominant in-plane heat spreading motivates summarizing the out-of-plane heat transfer by an equivalent thermal resistance, $R_{\perp}$.

The introduction of an equivalent resistance simplifies the resistance network, see schematic in figure 37b. The nodal networks illustrate that the equivalent resistance of the board consists of two parallel heat paths through the copper and the FR4. A multi-nodal network enables to determine the equivalent resistance of each material plane $R_{\parallel}$, see schematic in figure 38b. The analysis assumes an equal circumferential temperature on the edges of the board, T_{BC}. The assumption leads to an equivalent thermal node, B, which describes a sink temperature of the board.

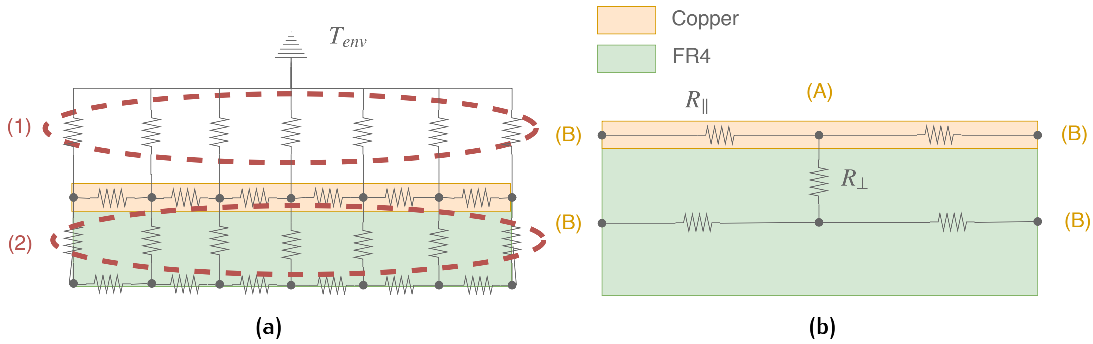

Figure 37: Thermal resistance model for the subsystem boards. (a) Detailed multi-nodal network model of the board. The enumeration denotes the two modelling assumptions. The heat sinking from the bottom side is not shown for visualization purposes. (b) Simplified two-node thermal resistance network to describe board-level heat conduction.

The equivalent resistance, $R_{\perp}$, describes the heat transfer in the out-of-plane direction. The thermal resistance in the out-of-plane direction solely depends on the FR4 layers because of the high conductivity and low thickness of the copper layers (Gurrum et al., 2011; Graebner and Azar, 1997).

$$R_{\perp} = \frac{t_{FR4}/2}{\lambda_{FR4,\perp} A_{equivalent}} \tag{24}$$

Equation 24 includes an equivalent area in the out-of-plane direction, see schematic in figure 38a. A comparison between the simplified and multi-nodal mode enables to determine the equivalent area. The schematic in figure 38b describes the methodology to determine the equivalent resistance of the multi-node model. The temperature gradient between center and edges yields a thermal resistance, see equation 25. The thermal resistance corresponds to the nodal network $A \rightarrow B$, see figure 37b. The comparison between the thermal resistance of both models yields the equivalent area, $A_{equivalent}$.

The thermal behavior of the network $A \rightarrow B$ changes with the location of the copper plane. The derivation of the equivalent area with the copper plane on top or bottom yields similar values, such that the remainder of the analysis uses their mean.

$$R = \frac{\dot{Q}_{in}}{T_{in} - T_{BC}} \qquad A_{eq.\,cu.\,top} = 2.8 \times 2.8 mm^2 \qquad A_{eq.\,cu.\,bot.} = 2.9 \times 2.9 mm^2 \tag{25}$$

The multi-nodal board model in figure 38b enables to determine the equivalent conductance of a copper and FR4 plane. The comparison in table 21 shows that the continuous copper plane has an equivalent thermal conductance by one order of magnitude larger than a significantly thicker FR4 plane. The reason for this difference is that the in-plane thermal conductivity of copper is by three orders of magnitude larger than the conductivity of FR4.

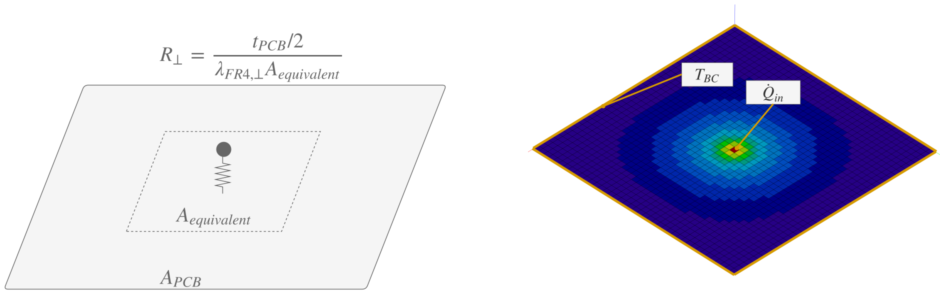

(a) (b)

Figure 38: Determination of the equivalent area, $A_{equivalent}$, to determine $R_{\perp}$. (a) Schematic of the equivalent area under a component mounted on the surface, represented by a node and thermal resistance. (b) Determination of the equivalent resistance by using a multi-node, two-layer model of the board in ESATAN. The model consist of a copper and FR4 layer with a high contact coefficient providing a negligible contact resistance between the materials complying to the PCB description by Graebner and Azar (1997), $h_{contact} = 10^5\ W/m^2K$.

Table 21: Equivalent conductance of continuous, $42 \times 42mm$ copper and FR4 planes.

	Copper	FR4 epoxy laminate
Thickness t $[\mu m]$	35	1565
$C_{\parallel}$ $10^{-3}[W/K]$	18.1	1.7

5.3.2 Design parameters for subsystem board layout

Location of continuous copper planes

PCBs employ continuous copper planes for electrical grounding and shielding. The location of the continuous copper planes is a significant factor for the thermal behavior, see equivalent conductance in table 22. The schematics in figure 39a and 39b show the equivalent thermal networks for a single-layer subsystem board with a continuous copper plane on top and below. The schematic in figure 39b includes a smaller copper layer on top that represents the necessary tracing for placing a local hotspot in the center. The analysis assumes a worst-case scenario for the heat spreading, i.e. two traces, one for power supply and one for grounding.

Table 22: Equivalent board conductance for a single-layer PocketQube subsystem board.

	Copper plane on top	Copper plane on bottom
Conductance C_{Board} $10^{-3}[W/K]$	2.6	19.2

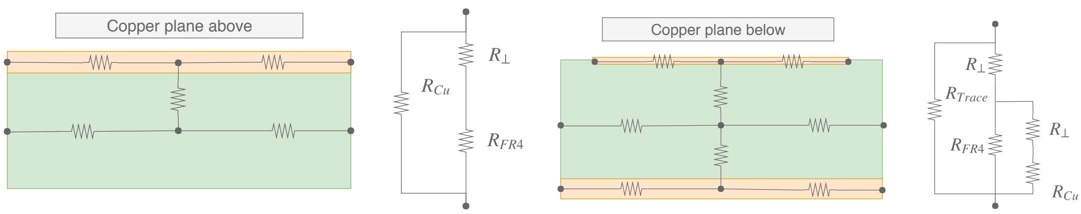

(a) (b)

Figure 39: Equivalent thermal resistance network for a continuous copper plane on the (a) top and (b) bottom side of the board. The schematic in figure (b) includes a copper trace to account for necessary tracing for a local hotspot placed on top and in the center of the board, also referred to as point (A) in figure 37b.

Number of thermal VIAs

A VIA is a copper element to electrically connect various circuitry layers in a PCB. The high thermal conductivity of copper makes VIAs a relevant factor for the heat transfer in the out-of-plane direction. The electronic circuit design determines the necessary VIAs for the electrical functionality. The term *Thermal VIA* refers the VIAs that increase heat spreading without providing electrical functionality. Thermal VIAs increase conductive heat sinking through the board by bypassing the insulating FR4 layers in the out-of-plane direction.

The thermal resistance of a through board VIA derives from the conduction through a hollow copper cylinder with height t_{PCB} and the footprint defined by the radii r_{outer} and r_{inner} (Kasemsadeh and Heng, 2017). The conductance of a single VIA is four times larger than the equivalent conductance through the board, see table 23. The magnitude in conductance illustrates the impact VIAs have on the thermal behavior.

$$R_{VIA} = \frac{t_{PCB}}{\lambda_{Cu} \pi \left(r_{outer}^2 - r_{inner}^2 \right)} \tag{26}$$

Table 23: Comparison of the equivalent conductance of the FR4 board in the out-of-plane direction and a thermal VIA.

	Board FR4 $R_\perp$	Thermal VIA
Conductance $C_\perp$ $10^{-3}[W/K]$	2.9	12.3

Thermal VIAs are an effective means to bypass the insulating FR4 layers. The application of thermal VIAs to the worst-case board layout introduced in figure 39b will increase the equivalent board conductance, and hence increase the heat sinking. The graph in figure 40b shows that the board-level conductance increases with the number of thermal VIAs connecting the central node with the continuous copper layer. The application of thermal VIAs, accordingly, is an effective means to alleviate the temperature load of an isolated thermal hotspot by increasing the heat spreading through the board.

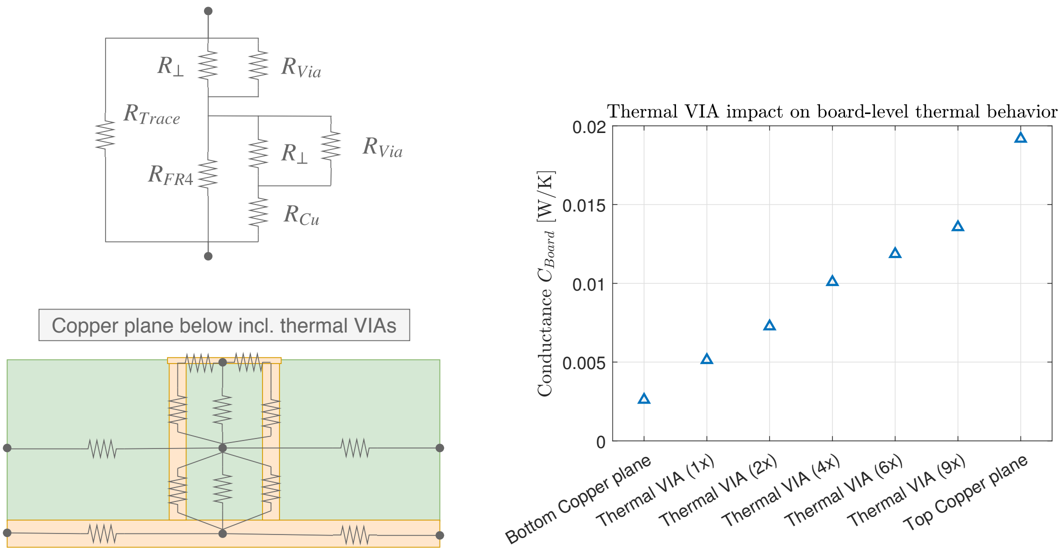

Figure 40: Impact of thermal VIAs on the board-level conductance. (a) Equivalent nodal network and (b) board-level conductance as a function of the number of layers.

Number of copper planes

The thermal heat transfer on a board-level depends on the number of continuous copper planes. Graebner and Azar (1997) conclude from an experimental study on multi-layer PCBs that the continuous copper planes provide the most relevant parameter for the board-level heat transfer. The presence of FR4 in in the circuitry inhibits the heat flow. The IR image of the Arduino in figure 11b illustrates how interruptions in the circuity inhibit the heat spreading

The Delfi-PQ includes subsystem boards with maximum of eight layers of electric circuitry. The maximum number of continuous copper planes in an eight-layer board is typically four (Sattel, 2018). This study, therefore, considers a PCB with four continuous copper layers as the upper limit case.

The thermal resistance network follows the previous modeling approach, see figure 41a. The analysis shows that adding continuous copper layers to a single-layer board with copper on top yields a comparatively small increase in the equivalent conductance, see table 24.

The small increase in conductance implies that the FR4 layer below the top copper plane inhibits heat spreading through the additional copper planes. The insulating behaviors implies that thermal VIAs connecting the copper planes enhance the conductive heat transfer. The graph in figure 41b illustrates that the application of thermal VIAs enables to almost double to equivalent board conductance.

Table 24: Equivalent board conductance for single- and four-layer PocketQube subsystem boards.

	Single-layer (copper bottom)	Single-layer (copper top)	Four-layer	Four-layer 2x VIA
Conductance C_{Board} $10^{-3}[W/K]$	2.6	19.2	22.2	43.2

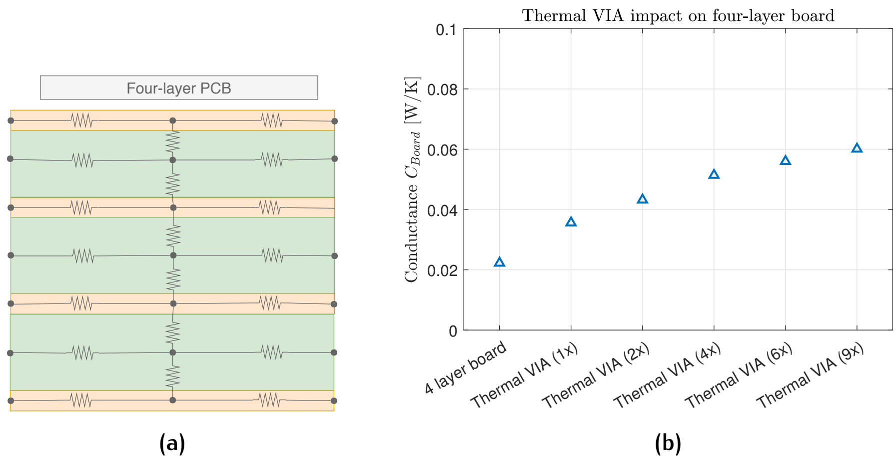

Figure 41: Equivalent board-level thermal conductance of a four-layer PCB. (a) Equivalent the nodal network. (b) Impact of applying the thermal VIAs to the four-layer PCB. The VIA modeling follows the approach shown in figure 40a.

Tracing and electronic circuitry

Copper tracing connects electrical components providing energy supply and signal paths. The copper tracing provides paths for sinking heat for the power dissipated over a component. The heat sinking capabilities depend on the number of traces and their geometry.

The number of pins defines the maximum traces connecting to an electronic component component. The Delfi-PQ microcontroller and power amplifier provide a benchmark for the number of traces, see table 25. The analysis assumes that two power traces of $25 mils$ width and signal traces of $10 mils$ width for each component. The thickness of the copper tracing is equal to the copper planes, i.e., $35 \mu m$.

The graph in figure 42 describes the increase in board conductance with the number of traces. The graph includes two dashed lines that illustrate the equivalent conductance of the previous analysis cases of board with a continuous copper plane on either top or bottom. The number of traces can have the same effect as the application of thermal VIAs.

Table 25: Equivalent board conductance for single-layer board with signal traces. Information taken from (RFMD, 2018; Texas Instruments, 2015)

	Resistor	Power Amplifier RFPA0133	Microcontroller MSP432-VQFN
n_{pin} $[-]$	2	16	64

The tracing analysis presents a best-case scenario for the heat spreading. The analysis assumes straight traces that spread from the center of the board to the edges. Moreover, the analysis assumes that all traces connect with a single node in the center. Both assumptions provide a best-case scenario for the heat spreading. First, there is a resistance between the location where the dissipation occurs, the junction, and the traces- Second, discontinuities in the tracing inhibit heat spreading (Graebner and Azar, 1997; Texas Instruments, 2013; Stout, 2009).

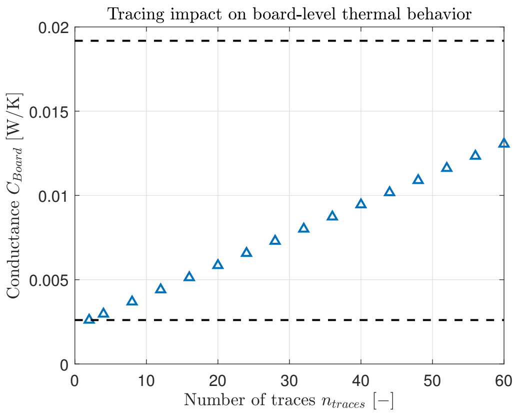

Figure 42: Equivalent thermal conductance of a single-layer subsystem board including tracing. The thermal resistance model follows the example shown in figure 39b.

5.4 COMPONENT-LEVEL HEAT TRANSFER

The operation of electrical components causes dissipation, which translates into heat. The primary mechanism for heat sinking from a component is conduction to the board (Edwards and Nguyen, 2016; Lohan et al., 2000; Kasemsadeh and Heng, 2017). Moreover, heat sinking occurs through radiation from the components surface. The schematic in figure 43 shows the corresponding nodal network. A single node represents the component and a current source to the heat input to the node due to power dissipation.

The resistance $R_{junction-2-board}$ describes the conductive link between component and board. The conductive resistance depends on the material composition of the component and its mounting. Therefore, thermal resistance varies among components. Table 26 shows the conductance of the components relevant for the Delfi-PQ. The comparison shows that Integrated circuit (IC) components show a higher conductance than resistors. IC components typically include thermal pads with a high thermal conductivity that connect the dissipating part with the board and facilitate heat sinking (Gurrum et al., 2011).

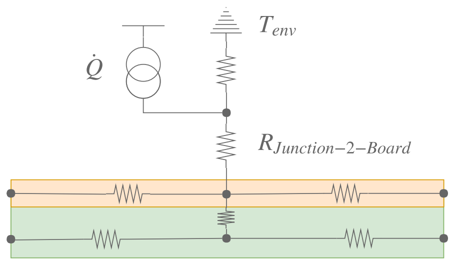

Figure 43: Equivalent thermal nodal network for a component on subsystem. The resistance $R_{junction-2-board}$ describes the conductive link between the component and the baord. Component datasheets provide the resistance values. The electrical dissipation of a component translates into heat, which the current source represents. The illustration of the heat sinking from the board's surface is omitted.

Table 26: Conductance between junction and mounting location. Technical data sheets for electronics components provide information on the conductive resistance, $R_{junction-2-board}$. The radiative conductance C_{rad} assumes an emissivity of $\epsilon = 0.9$ and a temperature gradient of $60K$ between component and environment. All values are given in $10^{-3}[W/K]$

	Resistor 1206 (Vishay, 2010)	Power Amplifier 16QFN (Stout, 2009)	Microcontroller VQFN (Texas Instruments, 2015)
$C_{junction-2-board}$	50.0	166.7	120.5
C_{rad}	0.04	0.06	0.6

5.5 CONCLUSIONS

This chapter investigates the thermal behavior of PocketQube subsystems on three assembly levels. The analysis uses the thermal resistance analogy to identify dominant heat paths and significant design parameters. The following bullet point list summarizes the major findings. The results of the board-level analysis provide the input for the design of representative PocketQube subsystem boards in the next chapter.

Subsystem-level heat transfer

- **Radiation is the primary exchange mechanism on a subsystem-level.** The comparison of radiative with conductive heat paths shows that the radiative accounts for more than 70% of the total heat transfer between a subsystem with its surroundings. The majority of the radiative heat exchange occurs with the adjacent subsystem boards. The magnitude of the radiative heat transfer implies that thermal control measures are most effective when targeting at the radiative heat transfer. The emissivity is physically constraint between zero and unity. The high emissivity of PCBs implies that the design space is larger for reducing the emissivity than increasing it. Accordingly, the most impactful thermal control measures are reductions in the emissivity to retain heat on a subsystem.

- **The contact conductance between spacers and subsystem boards provides the largest resistance for the conductive heat flow.** The contact resistance between two aluminum surfaces with rough surface properties is by two orders of magnitude larger than the conductive resistance through the spacer material. Smoothing the contact areas, increasing the contact pressure and applying a thermal filler enable to reduce the contact resistance and enhance the conductive heat transfer. The high emissivity of PCBs indicates that lowering the contact resistance is a more effective thermal control solution to reject heat on a subsystem level.

Board-level heat transfer

- **The amount of continuous copper is the most significant factor for the board-level thermal behavior.** The analysis shows that the equivalent conductance of a copper plane is by one order of magnitude larger than of a FR4 plane despite the significantly lower thickness. Similarly, in the out-of-plane direction, a single thermal VIAs provide a considerably larger conductance than FR4 because of the higher thermal conductivity of copper.
- **The placement of a heat source with respect to continuous copper planes is the most impactful board-level design measure.** The equivalent conductance for a single-layer board changes by a factor of seven when placing the continuous copper plane on the same or opposite side of a heat source. The placement of a thermal hotspot on a continuous copper plane is, therefore, an effective strategy to mitigate overheating.
- **Thermal VIAs are an effective means to increase heat transfer through insulating FR4 layers.** The FR4 layers are the major inhibitor for heat transfer in the out-of-plane direction. The application of two thermal VIAs almost doubles the equivalent board conductance for single- and four-layer boards.
- **The addition of continuous copper layers to a single-layer board with a copper plane on top provides a small improvement in the equivalent conductance.** However, the application of thermal VIA connecting the copper planes increases the equivalent conductance.

Component-level heat transfer

- **Conduction to the mounting location is the primary path for heat dissipated on an electric component.** The comparison of the thermal conductances between three electronic components highlights that conduction to the board is significantly larger than radiation to the surroundings. IC components show better conduction to the board than resistors and are thus easier to handle from a thermal perspective.

6 DESIGN OF REPRESENTATIVE POCKETQUBE SUBSYSTEM BOARDS

The thermal screening method relies on graphs to describe the temperature increase of a thermal hotspot at ambient and vacuum conditions. Moreover, the method includes a feedback loop with potential design solutions to mitigate hotspot overheating. This thesis uses testing to implement both elements, which requires hardware test objects.

As of July 2018, the design of the Delfi-PQ subsystems is incomplete regarding hard- and software. The absence of hardware motivates designing test boards dedicated to this study. The design of dedicated test boards provides more deterministic test cases for parameter analysis than engineering or flight models of PocketQube subsystems.

This chapter first re-iterates how the testing relates to the proposed thermal screening method by defining test objectives. The following section presents the electronic design of the test boards. Their design follows from the previous thermal resistance analysis and a simple three-node thermal resistance model of the subsystem boards. The next section introduces the three-node model, which enables to define and predict test scenarios in fulfillment of the test objectives.

6.1 TEST OBJECTIVES

Primary objective *To characterize the temperature increase of the thermal hotspots on the representative PocketQube subsystems boards (see figure 46) both at ambient and vacuum conditions by measuring the steady-state temperature response of the hotspots to constant heat loads.*

If a component reaches critical temperature conditions, countermeasures are necessary to mitigate overheating. The thermal resistance analysis in chapter 5 identifies PCB layout parameters to enhance sinking from a hotspot to the board. These layout options provide both design solutions to both counteract and prevent thermal hotspot overheating.

Secondary objective (A) *To compare the performance of board-level thermal design solutions in reducing the temperature of thermal hotspots on the representative PocketQube subsystem boards (see figure 46) by measuring the steady-state temperature response to constant heat loads at ambient conditions.*

The work on the primary objective includes vacuum measurements that will use the available test equipment, see available pumps in table 16. The pressure level of the available pumps is several orders of magnitude lager than the vacuum conditions during flight. Therefore, the experimental graphs describing the vacuum heating of hotspots (primary objective) will show a lower temperature than in flight conditions. However, the experiments provide data to validate numerical simulation models against ambient and low-pressure measurements. A validated simulation enables to describe the thermal behavior in the complete absence of natural convection phenomena because the natural convection heat transfer coefficient is the only model parameter that changes with the environmental pressure. Consequently, it is possible to estimate the temperature error of performing thermal-vacuum testing at moderate pressure levels. The additional temperature increase adds to hotspot vacuum heating diagrams. The additional temperature increase equals the error for performing thermal-vacuum testing at moderate pressure levels compared to the design standards of larger spacecraft (ECSS, 2016).

Secondary objective (B) *To determine the temperature error of performing thermal-vacuum testing in the fine vacuum regime ($10^2 - 10^{-1} Pa$) compared to ideal vacuum conditions ($0 Pa$) by validating a numerical simulation model against the experimental data of the test boards at ambient ($10^5 Pa$) and fine vacuum conditions.*

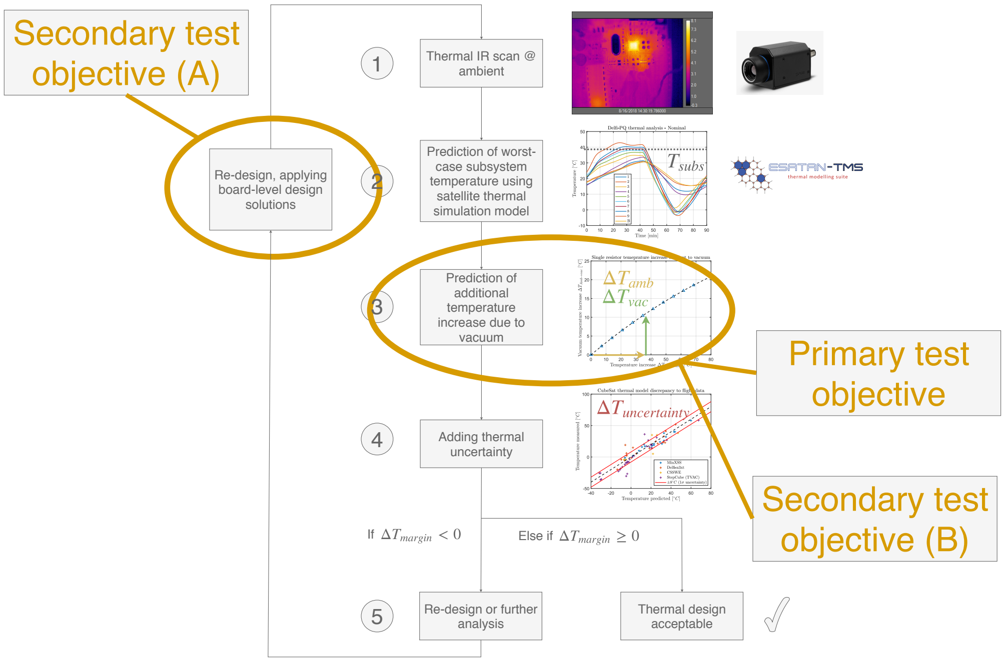

Figure 44: Primary and secondary test objectives in relation to the proposed thermal screening method.

6.2 TEST BOARD CIRCUIT LAYOUT

This study uses representative PocketQube subsystem boards with Surface mount device (SMD) resistors as the hotspot component. Resistors provide flexibility towards manipulating the power dissipation, i.e., heat input to the system, because the power dissipation depends directly on the supply voltage. The passive electronic design, compared to the use of IC components, removes the necessity of designing operational scripts to achieve power dissipation on the hotspot, see also experiment design for the ArduinoUNO case study in chapter 3. Moreover, resistors provide a worst-case scenario for SMD components because of their small geometric size and comparatively poor thermal conduction to the mounting location, see comparison of the thermal resistances in table 26. The *1206* SMD resistor metric enables to reproduce the footprint of the Delfi-PQ power amplifier by placing two resistors next to each other. Th power amplifier for RF communication is a critical hotspot component of the Delfi-PQ and, therefore, serves as a case study to later demonstrate the application of the thermal screening method.

The electronic circuit schematic in figure 45 shows the test boards and describes its design attributes. The image in figure 46 shows the PCB hardware that derives from the circuit design. The main test board includes eight individual test boards with a footprint following the PQ9 standard for PocketQube subsystems (Radu et al., 2018). Each individual test board includes two pin connectors for external power supply. Table 27 describes the layout of the test boards highlighting their difference concerning thermal design.

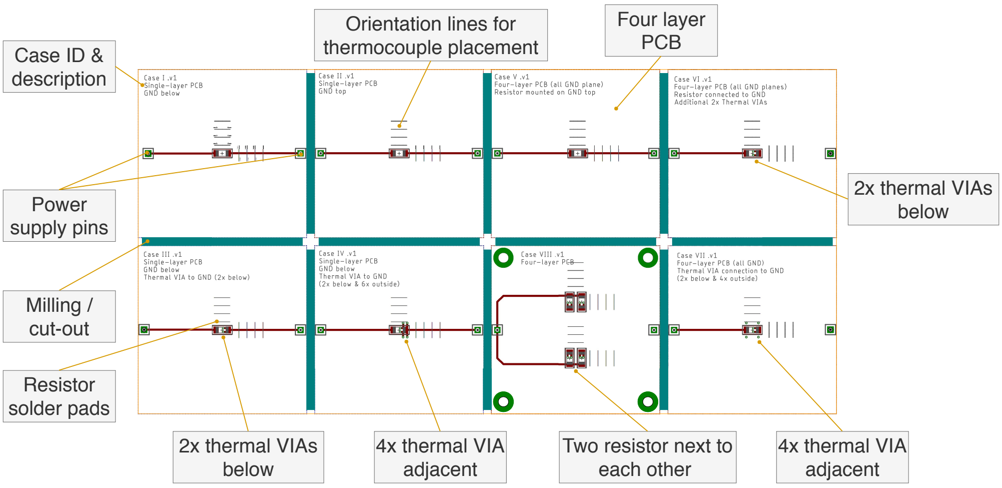

Figure 45: Electronic circuit design of the test boards. The numeration of the board segments refers to table 27.

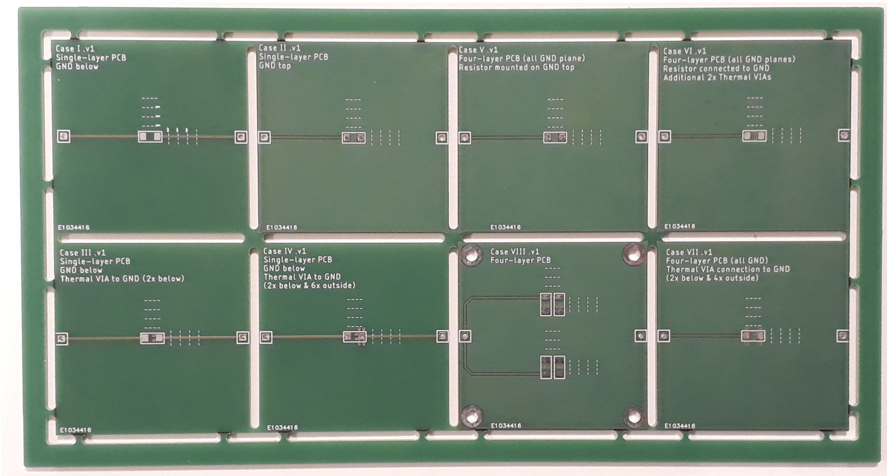

Figure 46: Image of the test PCB. The eight individual test boards are cut out from main board. The enumeration and description in the top left corner refers to table 27

Table 27: Description of the test board characteristics, see figure 45 for the corresponding circuit design.

Test ID	No. copper layers	Description	Study case
I	1	GND on back	Hotspot on FR4 plane (worst-case)
II	1	GND on top	Hotspot on continuous copper plane
III	1	2x VIA below	Connecting hotspot to 2x VIAs
IV	1	2x VIAs below & 4x VIAs adjacent	Increasing number of VIAs
V	4	Four-layer PCB	Increasing number of copper layers
VI	4	2x VIA below	Connecting to 2x VIAs
VII	4	2x VIAs below & 4x VIAs adjacent	Increasing number of VIAs (best-case)
VIII	4	Two resistors next to each other & 2x VIAs below	Hotspot with larger footprint

6.3 ANALYSIS CASES – CONCEPTUAL ANALYSIS

The temperature increase of a thermal hotspot depends on its heat exchange with the environment. This section presents the analysis cases of the experimental test campaign. The discussion on the analysis cases makes use of a simple nodal network simulation model. The network model enables both to identify dominant parameters for the analysis case design and predict the experimental behavior.

6.3.1 Three-node thermal resistance model

The temperature increase of a thermal hotspot depends on its thermal connection to the surroundings . A component exchanges heat with the surroundings through radiation and convection, as well as conduction to the PCB that the component is mounted on. The thermal resistance network in figure 47a provides a simplified thermal representation of a resistor on a PCB. The network includes three thermal nodes, one for the resistor and two for the board. A current source connects to the resistor node, which represents the heat input due to electrical power dissipation. The network includes two conductance that describes the conductive heat transfer between the resistor junction, mounting location, and mean temperature of the board.

The temperature increase of the resistor relative to the mean board temperature depends on the footprint of the resistor, the conductive link to the board, the thermal characteristics of the board, and the environmental temperature, see a summary of the parameters in table 28. The ambient pressure determines the magnitude of the convective heat transfer between resistor and board and the surroundings, see pressure depends of the convective heat transfer coefficient in figure 29b. The schematic in figure 47b illustrates that the temperature of the resistor increase with decreasing environmental pressure.

Table 28: Overview on the relevant design characteristic for thermal hotspot heating and the related nodal network parameters, compare network schematic in figure 47a.

	Characteristic	Related network parameter
(a)	Footprint of the heat source	C_{res}, $R_{rad,res}$, $C_{conv,res}$
(b)	Thermal conductance of the board	C_{board}
(c)	Environmental temperature	$R_{rad,res}$, $C_{conv,res}$, $R_{rad,board}$, $C_{conv,board}$

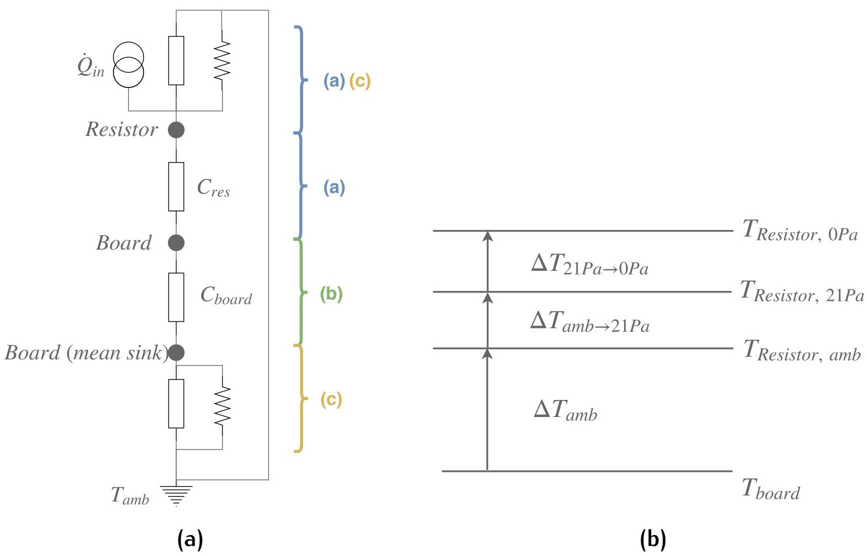

Figure 47: (a) Three-node thermal resistance network describing the test boards for conceptual analysis. (b) Temperature increase of the resistor relative to the mean board temperature as a function of the environmental pressure.

6.3.2 Power dissipation

The power supply is the primary input to the system, which causes temperature differences between the thermal nodes. The nodal temperatures scale with the supplied power, see figure 48a showing the resistor temperature increase.

The previous discussion on the power budget for PocketQubes concludes that the maximum power dissipation of future PocketQube subsystem boards is $2W$. The analysis in figure 48a predicts that a resistor already heats up beyond $+85°C$ for a power input of $1W$. The analysis considers, therefore, a maximum power input of $750mW$, which covers a range from room temperature to the standard operational temperature limit of COTS electronics. The table29 shows the nominal power inputs for each experiment of the test campaign. The table includes the actual power measured over the resistor with a multimeter.

Table 29: Power input for the experimental test cases, including nominal values supplied by a constant voltage source and the actual power measured over the resistor.

Test parameter	Power (nominal) [mW]	Power (actual) [mW]
1	0	0
2	125	124.8
3	250	247.7
4	500	488.4
5	750	734.4

The graph in figure 48a shows that both a linear and power fit describe the simulation results. The description with a linear fit is reasonable considering that the convection scales linearly with temperature, whereas the application of a power fit is reasonable because the radiative heat transfer scales with temperature to the fourth power. The alignment of the linear curve demonstrates that the radiative heat transfer is linearizable for the power inputs of this study.

$$\dot{Q}_{rad} \sim (T^4 - T_{amb}^4) \approx 4\, T_{mean}^3\, (T - T_{amb}) \tag{27}$$

The origin presents a physical boundary condition considering that without power supply the temperature of the test item remains at the temperature of the environment. This research assumes that, in first-order, a linear fit through the origin suffices to describe the thermal behavior.

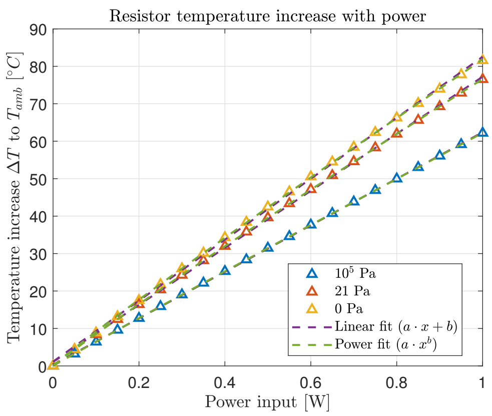

(a)

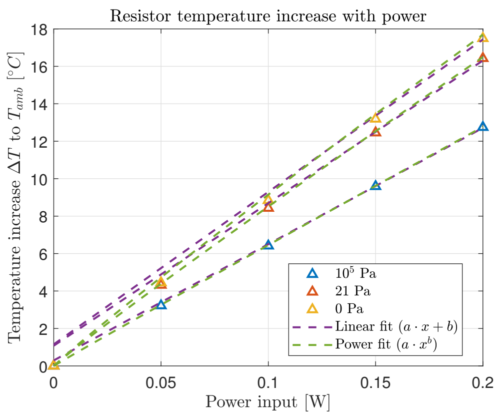

(b)

Figure 48: Preliminary analysis of the power scaling of the resistor temperature according to the nodal network in figure 47a. (a) Simulation results and fitted curves. (b) Close up of the curves around the origin.

6.3.3 Footprint of the thermal hotspot

A component's footprint determines the temperature increase in response heat loads. A small component shows a larger temperature increase than a small component because the radiative and convective heat sinking scales with the surface area.

The Delfi-PQ power amplifier provides a case study for the footprint analysis. The power amplifier is the most power consuming component of the Delfi-PQ, yet having the smallest footprint, see table 30. The choice of the *1206* SMD resistor metric follows this case study. The footprint of two 1206 resistors resembles the footprint of the power amplifier closest compared to other resistor sizes.

As of July 2018, the layout of the Delfi-PQ communication board is still under development. The current design proposal includes a continuous copper plane, which accommodates the power amplifier, a second continuous copper plane for electromagnetic shielding, and two layers of circuitry. The design of the test board VIII incorporates these design features providing a study case for the Delfi-PQ power amplifier.

Table 30: Overview on the most power-consuming electronics components of the Delfi-PQ satellite.

Component	Type	Footprint [mm]	Power dissipation [mW]
Microcontroller	MSP432 (Texas Instruments, 2015)	14×14	65 (Boerci, 2016)
Power amplifier	RFPA (RFMD, 2018)	3×3	500 (Boerci, 2016)

The three-node resistance model shows that the resistor temperature increase depends on the footprint size, see figure 49a and 51b. The relative temperature increase at ambient conditions decreases with the footprint size, whereas the relative temperature increase $\Delta T_{amb \to 21Pa}$ between ambient ΔT_{amb} and vacuum ΔT_{21Pa} remains constant.

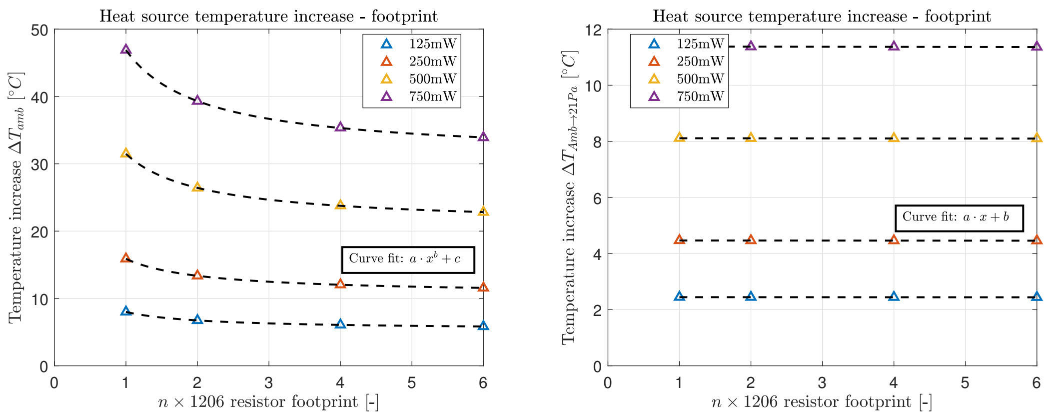

(a) (b)

Figure 49: Theoretical expectation thermal nodal network. (a) Heat source temperature increase as a function of the components footprint. (b) Heat source temperature increase between ambient and vacuum conditions.

A simplified version of the three-node network enables to explain the thermal behavior, see network figure 58a for the resistance network. The simplified version neglects the convective and radiative heat transfer from the resistor node considering that conduction to the board is significantly larger than radiation and convection from the resistor surface, see conductances in table 31. The simplification yields the analytical expression 28 considering that the radiative heat transfer is linearizable in the region of interest.

$$\Delta T = T_{res} - T_{amb} = \dot{Q} \left[\frac{1}{\frac{1}{1/C_{res} + 1/C_{board}}} + \frac{1}{h_{conv} A + 4 \sigma A \epsilon T_m^3} \right] \tag{28}$$

Table 31: Overview of the conductances related to the *1206* resistor node, see nodal network in figure 47a for reference. The convective and radiative convective conductances consider worst-case conditions yielding high conductance values, i.e., a $40K$ temperature gradient to the environment and ambient pressure conditions.

	Radiation	Convection	Conduction
Conductance $10^{-3}[W/K]$	0.03	0.04	50

The logarithmic behavior of the temperature increase at ambient pressure, ΔT_{amb}, is a consequence of analyzing the heating as a function of the thermal conductivity, $\Delta T = f(C_{res})$. The thermal conductivity scales linearly with the number of resistors when considering equal resistors.

Equation 29 illustrates that the conductivity of the resistor cancels out when considering the relative temperature increase between ambient and vacuum $\Delta T_{Amb \rightarrow 21Pa}$. Therefore, the relative temperature increase depends on the change in the convective heat transfer coefficient, $\Delta h_{Amb \rightarrow 21Pa}$. The convective and radiative heat transfer depend on the sink temperature of the board. The nodal network analysis shows that heat sink temperature varies by $0.4K$ between the analysis cases for a maximum power input of $750mW$. The small variation explains the nearly constant behavior of the relative temperature increase $\Delta T_{Amb \rightarrow 21Pa}$.

$$\Delta T_{Amb \rightarrow 21Pa} = \Delta T_{21Pa} - \Delta T_{Amb} = \dot{Q} \left[\frac{1}{h_{conv,\,21Pa} A + 4\sigma A \epsilon T_m^3} - \frac{1}{h_{conv,\,Amb} A + 4\sigma A \epsilon T_m^3} \right] \quad (29)$$

6.3.4 Thermal conductivity of the board

The board-level thermal resistance analysis in chapter 5 determines the PCB design characteristics that influence the thermal behavior the most. This bullet-points recall these design parameters, which provide the baseline for the test board layout in figure 45:

- The location of the hotspot in relation to the continuous copper planes.
- The number of continuous copper planes.
- The number of thermal VIAs.

Table 27 describes the available test boards. The boards span a spectrum of potential thermal design solutions to reduce the heat load of an isolated thermal hotspot. The equivalent board-level conductance, introduced in chapter 5, provides a quantitative parameter to compare the board layouts from a thermal perspective. The spectrum ranges from a worst-case isolated heat source (Case I) to a best-case highly connected scenario (Case VII).

Table 32: Design cases for the study of the test item. The first block refers to a single-layer PCB, while the second and third refer to a four-layer PCB-

Test ID	No. copper layers	Description	Conductance C_{Board} $10^{-3}[W/K]$
I	1	GND on back	2.6
III	1	2x VIA below	8.3
IV	1	2x VIAs below & 4x adjacent	13.0
II	1	GND on top	19.2
V	4	Four-layer PCB	22.2
VI	4	2x VIA below	43.2
VII	4	2x VIAs below & 4x adjacent	56.0

The graphs in figure 50a and 50b describe the resistor temperature increase as a function of the board conductance, C_{Board}. The ambient temperature increase scales logarithmically similar to the previous analysis case.

The magnitude of the temperature increase for the low conductance boards (I, III, IV) indicates a flaw in the modeling approach of the boards with tracing on top and an FR4 layer on top, see figure 39b for the equivalent thermal resistance network. The temperature increase is unrealistically high in comparison to the other boards. The experimental test campaign and design of a detailed thermal simulation model investigate this issue further.

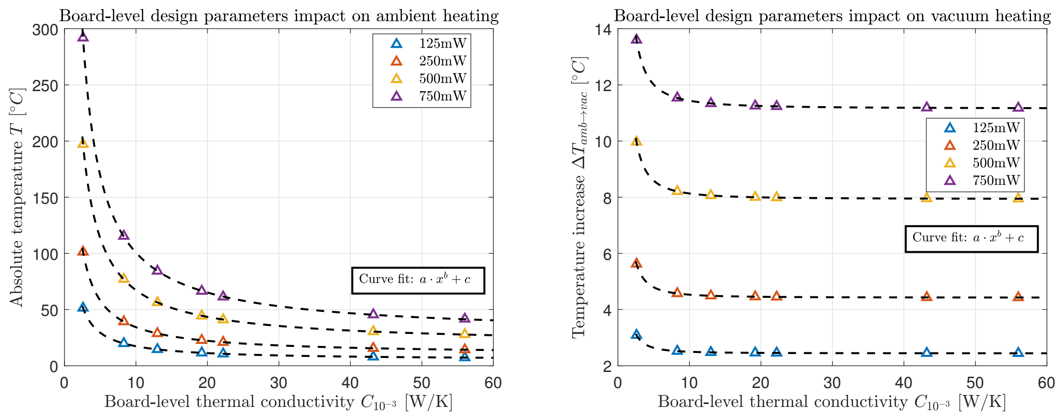

(a) (b)

Figure 50: Theoretical expectation thermal nodal network. (a) Temperature increase resistor at ambient conditions. (b) Relative temepràture increase between ambient and rough vacuum conditions.

6.3.5 Environmental temperature

The thermal screening method uses IR measurements. The method estimates the maximum flight temperature of a component by adding the measured temperature increase ΔT to expected subsystem temperature T_{subsy} of the global simulation model. Both the radiative and convective temperature scale with the mean temperature between the object and environment. The graphs in figure51a and 51b shows that the temperature increase of the resistor is temperature-independent at ambient but not at vacuum conditions.

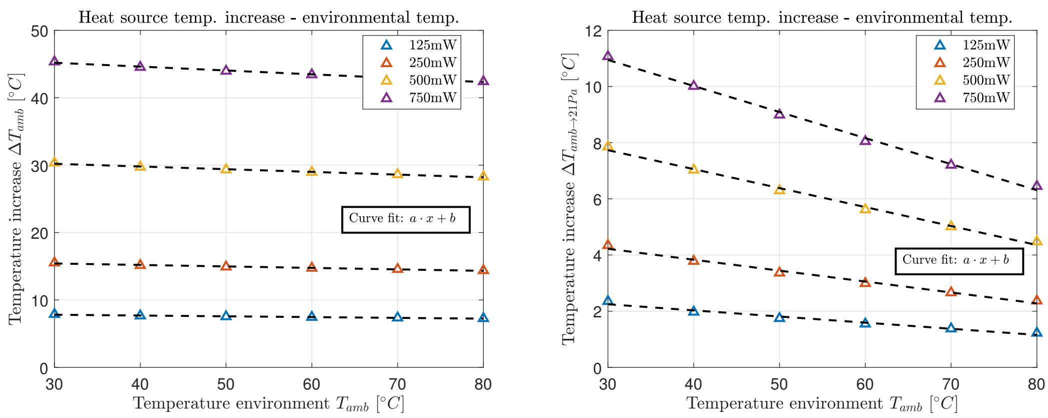

(a) (b)

Figure 51: Theoretical expectation thermal nodal network. (a) Heat source temperature increase as a function of the environmental temperature. (b) Heat source temperature increase between ambient and vacuum conditions.

7 DETAILED THERMAL SIMULATION MODEL

The generation of a detailed numerical simulation model relates to the secondary test objective. The validation of the numerical simulation model against the experimental results enables to investigate the temperature error between fine ($21Pa$) and ideal ($0Pa$) vacuum. Moreover, the validation of the modelling approach extends the analysis beyond the test cases presented in the previous section.

This chapter details the modelling approach. The methodology follows the thermal resistance analysis previously introduced. The numerical model increases the level of detail compared to the previous board-level analysis by describing the board-level conduction and heat sinking with a multi-nodal network. An emissivity calibration using the thermal IR camera determines the optical surface properties for the radiative heat transfer.

7.1 BOARD MODEL

The thermal modelling approach describes each PCB layer as a shell element with a thickness corresponding to the board layout. Two layers of in-plane nodes discretize the shell element further, see schematic in figure 52b. Each nodal plane consists of 42×42 nodes, which means that each node summarizes the temperature of a $1 \times 1mm^2$ element. The Biot number provides an estimate whether the discretization is appropriate, see a description in appendix A. The Biot number is significantly smaller for the mesh size considering worst-case assumptions of a single layer PCB, convective and radiative heat transfer, and a temperature gradient of $40K$ between object and environment.

$$Bi = \frac{l^* \left(h_{rad} + h_{conv.,1atm}\right)}{\lambda_{\parallel}} = 0.01 << 1 \tag{30}$$

The thermal conductivity determines the thermal resistance between nodes of the same material. The different material layers are thermally connected with a high contact conductance following the experimental results by Graebner and Azar (1997), which state that the thermal resistance between PCB layers is negligible. Moreover, the thermal conductivity of FR4 dominates the thermal resistance in the out-of-plane direction, which makes this contact conductance uncritical for the thermal behavior.

$$h_{contact} = 10^5 W/m^2K \tag{31}$$

Several test boards in chapter 6 employ thermal VIAs. The thermal VIAs provide a conductive link between the continuous copper planes. The modelling approach describes the VIAs as a thermal resistance between two thermal nodes. The thermal resistance considers out-of-plane heat transfer only because in-plane heat spreading to the adjacent FR4 material is assumed negligible due to the low thermal conductivity of FR4.

The single-layer test boards include a copper trace for power supply to the resistor. The copper trace provides a conductive heat path and, therefore, requires consideration in the model. The modelling approach describes the trace by a copper shell that is embedded in the FR4 plane, see figure 52b. The copper traces connects with the FR4 layers by a `fused contact zone`. This setting defines that the contact area is free from resistances.

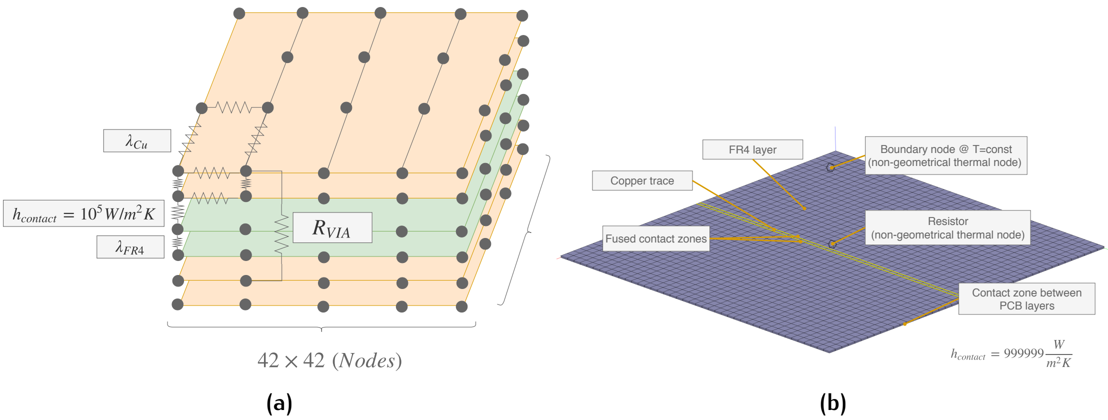

Figure 52: Numerical modelling approach to describe the test boards. (a) Multi-node network to describe the multi-layer board. (b) Modelling approach for a the single layer copper tracing with the continuous copper plane on the opposite side of the heat source. A shell element represents the copper trace, which is connected with FR4 plane using a fused contact.

7.2 RESISTOR MODEL

The modelling approach describes the resistor as a `non-geometrical thermal node`, see model in figure 52b. The resistance between node and board follows the thermal resistance value in the data sheet of the 1206 resistor, i.e., $R_{junction-2-board} = 20K/W$ (Vishay, 2010). Two parallel resistances describes the radiative and convective heat transfer from the resistors surface respectively. The analysis assumes that the resistor footprint corresponds to the effective area for the heat transfer. A constant heat load applies to the resistor node simulating the electrical power dissipation.

The test cases include boards with multiple resistors next to each other. The modelling approach describes the resistors by individual nodes next to each other, see schematic in figur 53.

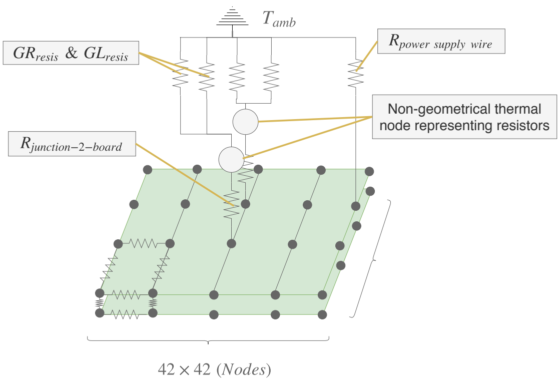

Figure 53: Modelling approach for the resistors using non-geometrical thermal nodes an equivalent thermal resistances to describe the heat transfer to the board and environment.

7.3 HEAT EXCHANGE WITH THE ENVIRONMENT

Each surface node, T_{ij}, includes two resistances that connect the surface node with a boundary node, as illustrated for the resistor nodes in figure 53. The boundary node maintains a constant temperature corresponding to the temperature of the test chamber during the experiment. The next subsections explain the definition of the convective and radiative heat transfer coefficients.

Two parallel resistances describe the convective and radiative heat exchange between the top and bottom surface with the environment. The parallel resistances connect each node with a boundary node, which maintains a constant temperature corresponding to the ambient temperature of each experiment. The local convective heat transfer coefficient h_{conv} is determined by taking each node's temperature and interpolate the heat transfer coefficient from the experimentally determined graph in figure 29b. The radiative heat transfer coefficient assumes radiation into a large cavity, see further discussion below. The radiative heat transfer coefficient uses the thermal IR camera to determine the emissivity of the test item, see experimental setup in figure 55a.

7.3.1 Convective heat transfer

Each surface node connects with the boundary node through a convective resistance. The convective resistance depends on the local heat transfer coefficient $h_{conv}\left(T_{ij}, p\right)$. The modelling approach uses the experimentally derived graphs for the convective heat transfer of a vertical flat plate at various pressures. The ESATAN model employs the `CNDFN1` function to interpolate the local heat transfer coefficient from the film temperature between th surface and boundary node.

7.3.2 Radiative heat transfer

Each surface node connects to the boundary node with a radiative resistance. The computation of the radiative resistance includes the emissivity and the radiative exchange factor between the board and the test chamber. This section describes the assumptions concerning these parameters.

Emissivity calibration of the test boards

The emissivities of the resistor and test board surface are unknown. The thermal IR camera enables to determine the surface emissivity through calibration either by comparison with a source of known emissivity or two-point emissivity calibration as described in chapter 3 for the ArduinoUNO case study, see equation 7.

The IR camera enables to determine the emissivity of the resistor and the test board. The determination of the emissivity is both possible through comparison of the IR signal with a surface of known emissivity and emissivity calibration as introduced in chapter 3.

The image in figure 54a shows the application of electrical tape to the resistor and board. The IR image shows an absence of temperature gradients between resistor junction, board, and electrical tape. The lack of temperature gradients implies that the emissivity of the resistor junction and board is similar to the electrical tape, i.e., around $\epsilon = 0.95$ (FLIR, 2015).

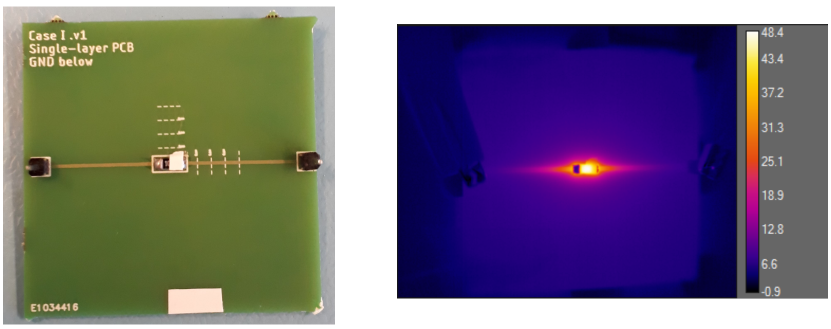

(a) (b)

Figure 54: Emissivity calibration of the test boards (a) using electrical tape. (b) Resulting IR image shows absence of temperature gradients between the resistor junction material and the tape, as well as an absence of temperature gradients between the PCB material and the electrical tape.

The image in figure 55a illustrates a second test set-up to determine the emissivity more precisely through a two-point calibration. The set-up includes a heater foil to heat the test board uniformly. Moreover, the test set-up compares one test board with a copper layer on top and one with an FR layer on top. Thermocouples on the top of the surface provide an absolute temperature measurement for calibration.

The IR image of the heated boards shows a uniform temperature distribution on each board, see figure 55. The absence of temperature gradients indicates a uniform emissivity for each board. Moreover, the emissivity of the resistor junction is equal to the board, whereas the solder presents low emissivity, see dark spots in the center of the board. The IR image illustrates that the polyimide foil is transparent to IR radiation.

The IR images show that the temperature between the two boards differs. The thermocouple measurement confirms a difference in temperature between the left (68.4°C) and right test board (71.8°C). Stronger mechanical contact between the right test board and the heater foil might explain the temperature difference between the two boards.

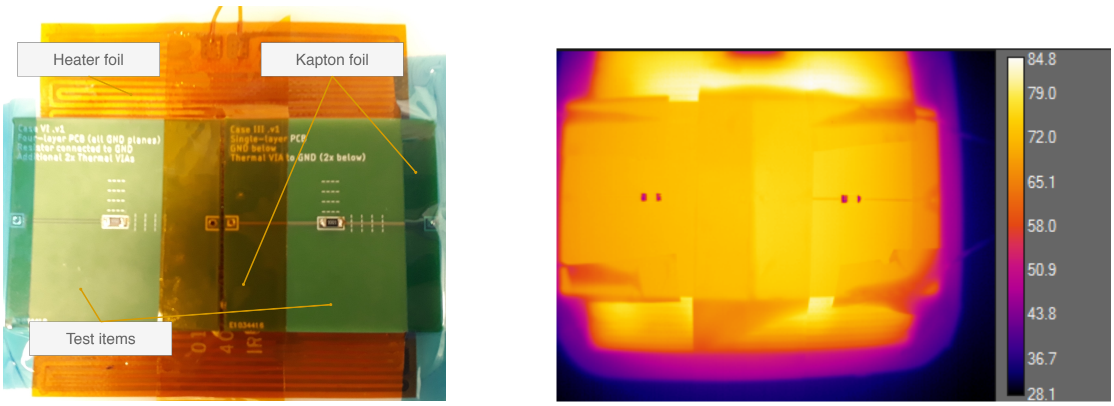

(a) (b)

Figure 55: Emissivity calibration of the test boards. (a) Measurement set-up as seen from the IR camera. The test set-up uses a heater foil to heat the test boards uniformly. (b) IR image of the test boards in a heated state.

Table 33 shows the emissivities that result from the two-point calibration described by equation 7 using three reference points on the board and averaging their emissivity. The calibration shows that the emissivity of board and resistor is high. Moreover, the calibration shows that the emissivity of the test board remains almost constant over a temperature range from $50 - 70°C$, see emissivity graph in figure 56b. Svasta et al. (2004) report a negligible temperature-dependency of PCB emissivities over a temperature range from $50 - 200°C$. This study, therefore, assumes that the emissivity is a temperature-independent parameter.

Table 33: Emissivity calibration of the test boards, actual surface temperature in the images measured with thermocouples.

	Board VI	Board III	Kapton tape
Emissivity ϵ $[-]$	0.982	0.977	0.989

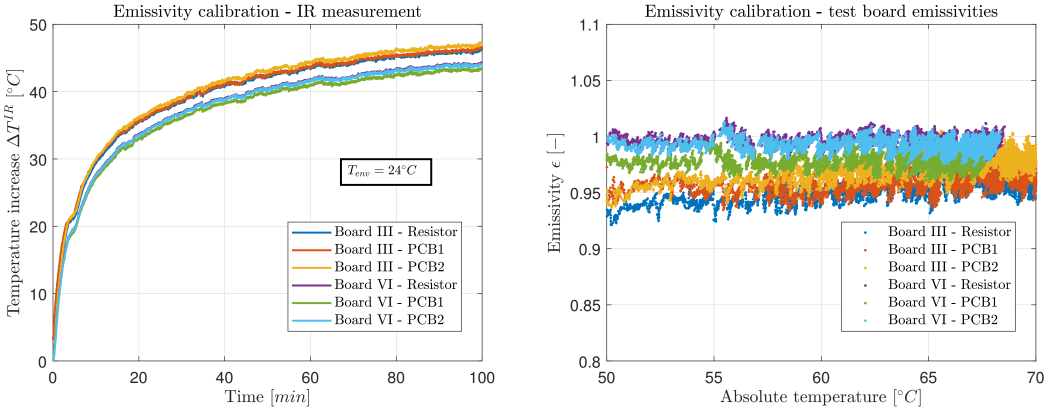

(a) (b)

Figure 56: Emissivity calibration of the test boards. (a) IR temperature measurement of the relative temperature increase to the ambient reference state. (b) Emissivity values deriving from applying equation 7 using the thermocouple measurements.

Radiative heat exchange with the chamber walls

The radiative resistance depends on the heat exchange factor B_{12} between the test item and the surroundings. The thermal simulation model assumes a radiative exchange factor of $B_{12} = 1$ considering the flat shape of the test boards ($F_{11} = 0$) and their small size compared to the Vacuumterm VT6130 test chamber.

The radiative heat exchange factor simplifies for small objects in large cavities, see below. The graph in figure 57 shows the relative error in the radiative heat transfer coefficient that results from the simplification as a function of the exposed surface area of geometries relevant to PocketQube testing. The shows that that relative error in the radiative heat coefficient is small.

$$B_{12} = \frac{1}{\frac{1}{\epsilon_1} + \frac{1}{F_{1,2}} + \frac{\epsilon_2 - 1}{\epsilon_2}\frac{A_1}{A_2}} \approx \epsilon_1 F_{1,2} \qquad A_1/A_2 \approx 0 \tag{32}$$

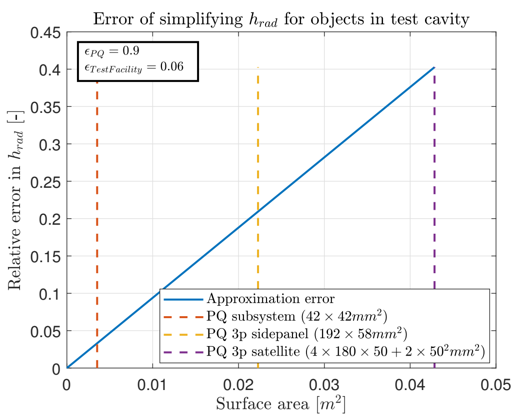

Figure 57: Relative error in the radiative heat transfer coefficient due to neglecting multiple reflections with the aluminum walls of the VT6130 test chamber.

7.4 VERIFICATION OF THE NUMERICAL SOLVER

The conceptual analysis in section 6.3 uses the ESATAN software as a nodal network solver. The detailed thermal model employs the same numerical solver to compute the nodal temperatures. The comparison of the numerical solver with an analytical solution verifies the ESATAN solver operates correctly.

A simplification of the three-node model in figure 47a yields an analytical expression for the nodal temperatures. The nodal network in figure 58a neglects the radiative and convective heat transfer from the resistor node, which yields the heat transfer equations33 and 34. The alignment between the analytical and numerical solution in figure 58b demonstrates that the solver operates correctly.

$$\dot{Q}_{in} = h_{conv}\left(T_{mean}, p\right) A \left(T_{board,sink} - T_{amb}\right) + \epsilon A * \sigma \left(T^4_{board,sink} - T^4_{amb}\right) \tag{33}$$

$$\dot{Q}_{in} = \frac{1}{1/C_{res} + 1/C_{board}} \left(T_{res} - T_{board,sink}\right) \tag{34}$$

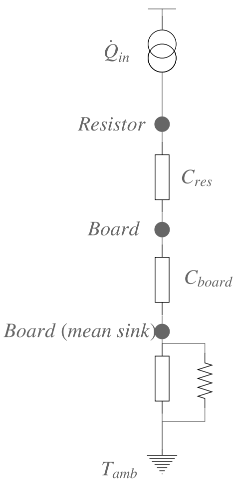

(a)

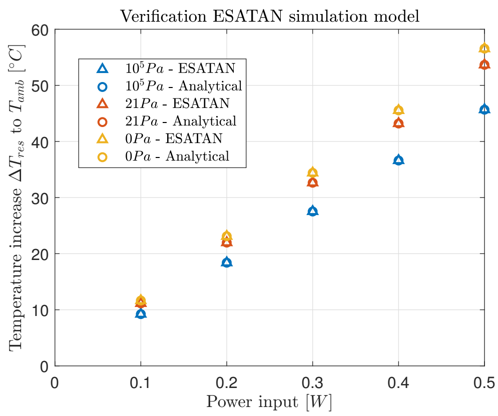

(b)

Figure 58: Verification of the ESATAN solver. (a) Simplified thermal resistance network using lumped three-node model. (b) Comparison between the ESATAN solver and the analytical calculation.

8 EXPERIMENTAL TEST CAMPAIGNS

This chapter presents the test results of the experimental test campaign by, first, describing the experimental set-up and, then, detailing the results concerning each test objective. The vacuum experiments show recurring issues because of an incorrect measurement set-up. The corresponding sections, therefore, focus also on explaining the root-cause for the insufficiencies in the measurement set-up.

8.1 EXPERIMENTAL TEST SET-UP

The test campaign uses both the IR camera and the thermocouples to measure the temperature of the test items. The images in figure 59a and 59b illustrate the experimental test set-up for both measurement techniques. The thermocouples facilitate both ambient and vacuum measurements, whereas the IR camera in the cleanroom is currently limited to use at ambient conditions.

A difference between the test set-ups is that the test chamber provides an enclosed environment, which might limit the effect of natural convection. However, the experimental results demonstrate that the test chamber provides a sufficiently large reservoir, such that both set-ups yield the same measurement at ambient conditions.

Both experimental set-ups employ fluorocarbon mono-filament fibers to suspend the test board. The fibers introduce a negligible conductive heat path, which simplifies thermal modelling of the test set-up. Moreover, the fibers provide flexibility in positioning the test item in the center of the chamber.

The image in figure 60 illustrates the measurement locations for each test. The number of thermocouple ports in the test chamber limits the number of temperature acquisition techniques. The lines on the PCB drawing facilitate the correct placement of thermocouples and temperature sampling points for the IR camera.

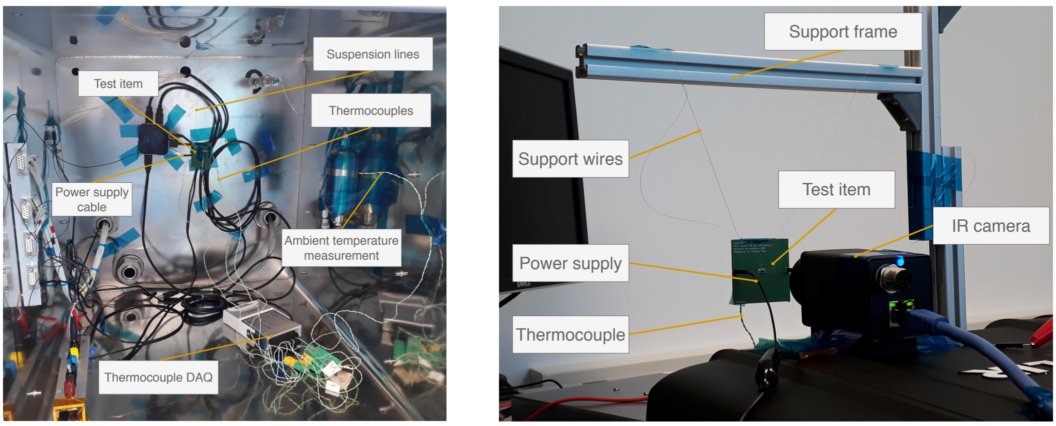

(a) (b)

Figure 59: Test set-ups in fulfillment of the two test objectives. (a) Test item hanging in the the Heraeus VT6130 thermal-vacuum oven. (b) Test item stand-off for IR imaging.

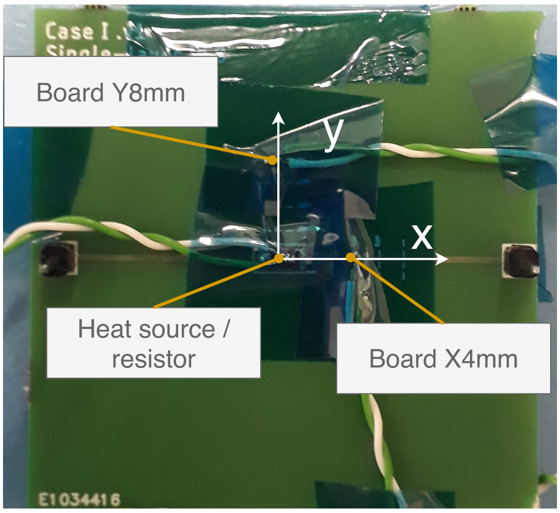

Figure 60: Temperature measurement locations. The orientation lines on the test boards facilitate locating the thermocouple measurement junction correctly.

8.2 DATA EXTRACTION AND PRESENTATION

The schematic in figure 61 illustrates how the next sections present the experimental data. The temperature measurements at ambient and vacuum conditions provide temperature plots, as shown on the left side of the schematic. Follow on analysis and data presentation presents the information using the temperature increase both at ambient, ΔT_{Amb}, and vacuum, ΔT_{vac}, as a function of the power input to the test board. The temperature increase accounts for difference in the environmental temperature among experiments.

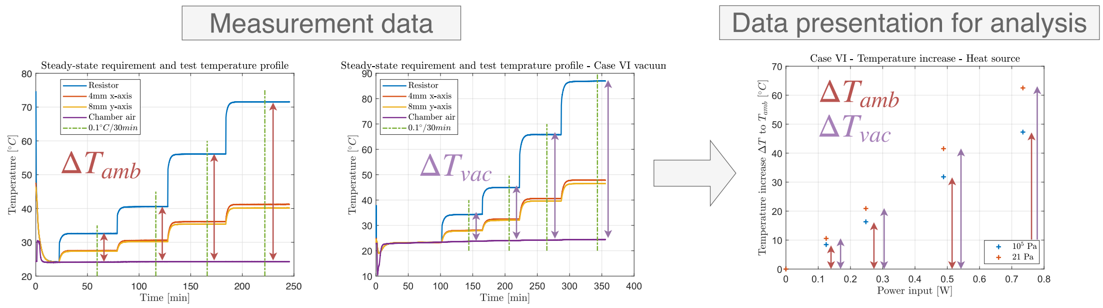

Figure 61: Illustration on how this chapter presents the measurement data in a single comparison plot. The resulting diagram corrects each measurement for the ambient temperature during each measurement.

8.3 TEST ACCEPTANCE CRITERIA

The establishment of acceptance criteria provides a means to check whether test data are adequate for further analysis. The establishment of acceptance criteria prevents concluding form test data that are flawed by an incorrect test set-up or human errors in the test procedure. This study uses the following acceptance criteria (a) - (c). Experiments that fail to meet the acceptance criteria build a starting point for further investigation. The examination is necessary to answer whether the non-compliance results from an incorrect measurements set-up or describes the actual physical behavior, which indicates a flaw in the reasoning on the expected behavior.

(a) The equipment and test set-up is free from visible defects before and after the experiment.

(b) The temperature measurement achieves stabilization, defined by a rate of change in the moving mean below $0.1°C/30min$.

(c) The measurement results are free from contradictions to the physical behavior described by the three-node thermal resistance model, see figure 47a.

8.3.1 Steady-state temperature stabilization

This study investigates the steady-state temperature increase to four power inputs. The consideration of steady-state conditions is appropriate for two reasons. The mass of PocketQube electronic subsystem components is low, which implies that steady-state conditions occur faster than for traditional spacecraft components. Moreover, thermal analysis by Avila de Luis (2018) indicates that PocketQube subsystem boards reach steady-state conditions during the sunlit part of a Low Earth Orbit.

Achieving actual steady-state in temperature requires extended test periods because both radiative and convective heat transfer scale with the temperature differences between the object and environment. The scaling implies that the temperature of an object approaches the steady-state conditions asymptotically, see the temperature graph in figure 62b of a conceptual, single-node model.

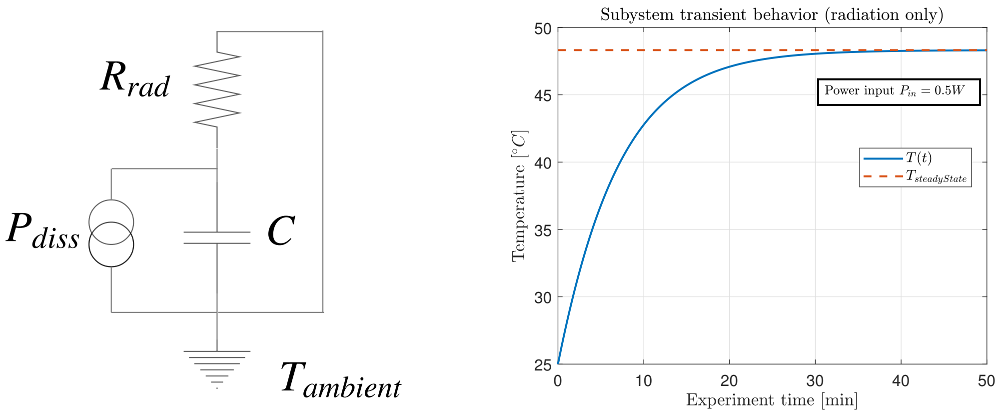

(a) (b)

Figure 62: Transient analysis of a single-node model of a four-layer PCB. (a) Equivalent thermal resistance network. (b) Transient temperature response to constant heat input.

The temperature stabilization criterion defines the acceptable temperature rate of change at which a measurement point is considered to be in approximate steady-state. Stabilization criteria in traditional thermal test standards define temperature stabilization when the temperature rate of change remains below $0.1 - 0.3°C/hr$ over several hours of testing(Welch, 2016). The low mass and thermal response time of PocketQube subsystems motivates adapting the stabilization criterion.

This study considers components in steady-state if the temperature rate of change in the moving average remains below $0.1°C/30min$. The plots in figure 63a show the temperature response of a four-layer board to the four power inputs described in table 29. The close-up of the first measurement point in figure 63b illustrates the noise in the measurement signal, which justifies considering a moving average to check to define the steady-stat criterion.

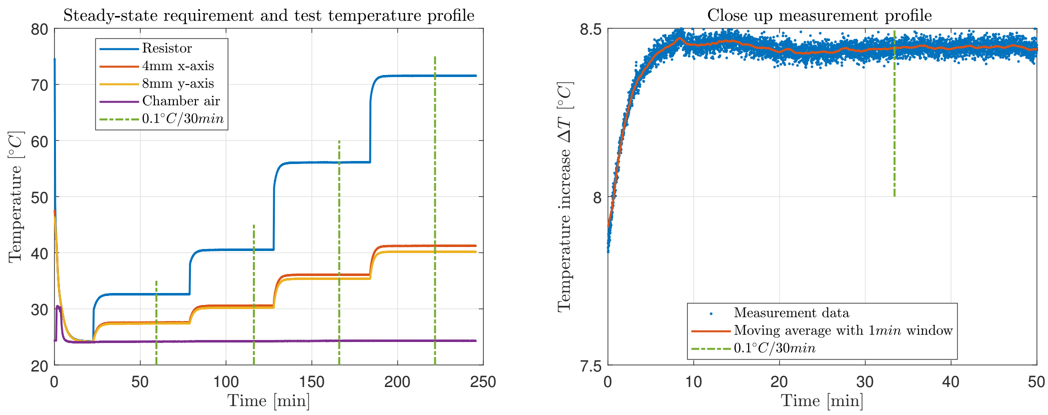

(a) (b)

Figure 63: Steady-state temperature criterion. (a) Temperature measurement profile for the heat inputs shown in table 29. The green, vertical lines indicate the time when the temperature stabilization criterion is satisfied for the resistor measurement. (b) Close-up of the temperature response to the first power input in (a). The graph shows the measurement signal and the moving mean, which is used to determine temperature stabilization.

8.4 PRIMARY TEST OBJECTIVE – RESULTS

The primary test objective aims at describing the relative temperature increase between ambient and vacuum conditions considering representative PocketQube subsystem boards. The experimental test campaign fails to meet the objective due to erroneous experiment design. This section describes why the application of thermocouples with polyimide foils is unreliable for this test set-up. Moreover, the section describes the approach to identify the design insufficiency. Ultimately, the section provides a solution to repeat the experimental test campaign.

8.4.1 Thermocouple application technique

The test set-up uses thermocouples to measure temperatures. Thermocouple are contact sensors and rely on surface contact between the measurement location and the thermocouple junction. A popular application techniques is to tape the thermocouple using polyimide foil. The application with polyimide foil facilitates reusing the thermocouples for multiple test campaigns. Moreover, removable application is also beneficial for subsystem boards that are subject to verification in multiple domains, e.g., mechanical and thermal testing.

The schematic in figure 64a illustrates two ways to apply the thermocouple to the resistor. The comparison between the two techniques in figure 64b demonstrates their equivalence concerning measurement accuracy. The longitudinal application is simpler to apply and is, therefore, the preferred application technique.

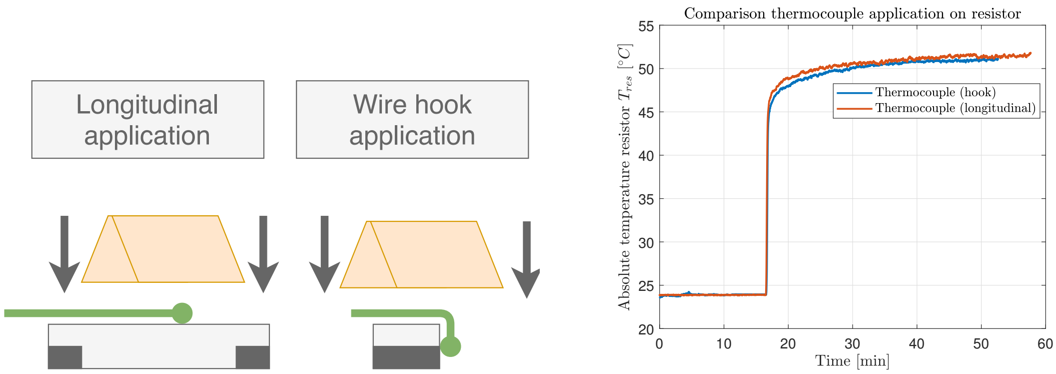

(a) (b)

Figure 64: Removable thermocouple technique. (a) Schematic of different techniques to apply a thermocouple (green) to a resistor (grey). The triangle illustrates the polyimide (orange) foil applied on top to ensure contact pressure between thermocouple and heat source. (b) Temperature response using both techniques.

8.4.2 First test campaign

Table 34 provides an overview of the testing during the first test campaign. The table lists the anomalies in the experimental test campaign. The anomalies motivate further investigation on the root cause, instead of continuing the test campaign for the remaining test cases.

Table 34: Overview on the results of the first test campaign employing thermocouples to measure the temperature in ambient and vacuum conditions. The symbol (✓) indicates compliance with all acceptance criteria. Non-compliance is indicated by the identifier of the corresponding criterion.

Date	Description	Acceptance	Description / Anomaly
20.09	Case II (50°C - vac.)	(a)	Thermocouple falling of test item, see figure 65a.
21.09	Case II (50°C - amb. and vac.)	(c)	Ambient measurement shows higher temperature increase than vacuum measurement, see figures 82a and 82b.
24.09	Case II (amb. and vac.)	(c)	Ambient measurement shows higher temperature increase than vacuum measurement.
24.09	Case VI (amb.)	(b)	Deviation from the steady-state behavior visible in measurement plot at last measurement point 750mW.
26.09	Case VI (vac.)	(c)	Ambient measurement shows higher temperature increase than vacuum measurement.
26.09	Case VIII (amb.)	(b)	Deviation from the steady-state behavior visible in measurement plot, see figure 66a .
27.09	Case VIII (vac.)	(b,c)	Deviation from the steady-state behavior visible in measurement plot, see figure 66b.
27.09	Case I (amb.)	✓	Successful test, see figure 80a.

The first experiment fails to meet the criteria due to visible damage in the experiment set-up, see the image in figure 65a. The measurement plot in figure 65b illustrates that the thermocouples detach from the test item. The graph shows first anomalies small anomalies in the temperature profile followed by rapid decreases in the measurement temperature signal. The first anomalies, i.e., signal diverging from expected steady-state behavior, indicate a loss in contact pressure, which, ultimately, leads to the detachment of the thermocouples. The anomalies in graph 65b provide insights that help to identify contact loss in follow-up tests. The subsequent tests employ a different polyimide foil, which provides better adhesion and prevents thermocouples from falling off the test item.

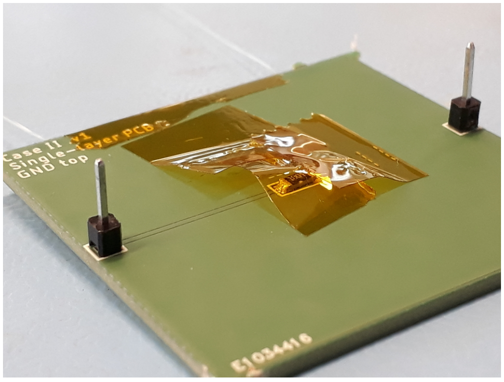

(a)

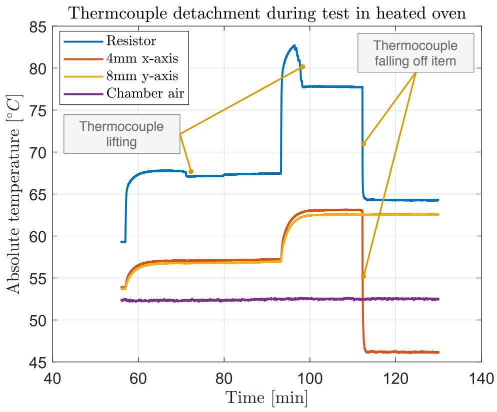

(b)

Figure 65: Thermocouple detachment during first test. (a) Visible defects in the experiment set-up after the test. (b) Thermocouple detachment visible in the temperature measurement plot.

Table 34 describes that the follow-up tests show visible anomalies in temperature plots. The measurement graphs of the test board VIII in figure 66a and 66b provide an example of the observed anomalies.

The ambient measurement profile in figure 66a shows a decreasing temperature at the final measurement point of 750mW power input. The continuous decrease in the measured temperature indicates a continuous decrease in contact pressure. Therefore, the last measurement point is unusable for further analysis, whereas the previous measurement points provide useful data. However, the vacuum measurement on the next day shows a lower temperature increase than at ambient conditions, see 66b. The lower temperature increase is unexpected considering the previous thermal resistance network, see figure 47a. Controversially, the measurement plot shows a temperature increase at the final measurement point. The temperature signal can only become large if the contact pressure increases because the resistor is the only heat source. However, the increase in contact pressure implies that the previous measurements are erroneous despite the absence of visible anomalies in the steady-state temperature profile.

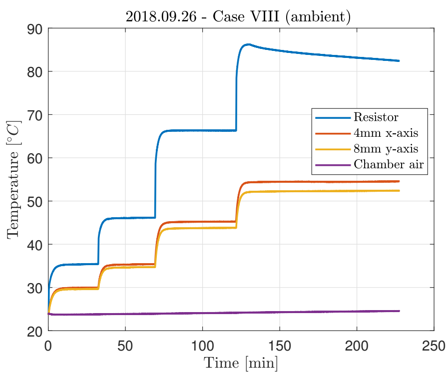

(a)

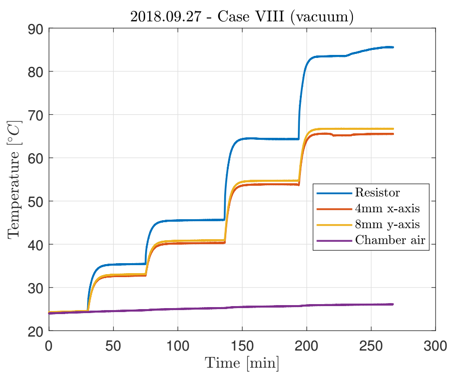

(b)

Figure 66: Thermocouple measurement plot of case VIII during the first test campaign. (a) Ambient and (b) vacuum measurement.

Similar anomalies occur in the measurement of the best board II and VI. In preparation of the experiment on test board I, it was was noticed that the blank thermocouple wires of the resistor thermocouple were almost touching. The manual application of the thermocouples with applying pressure might have caused the thermocouples to touch and create an additional junction. The hypothesis is that an additional junction measures a different temperature than the assigned location explaining the lower temperature of the vacuum measurements, like for the ArduinoUNO case study in figure 18a. As a consequence, the experiment of the board I applies an untwisted thermocouple and a larger piece of polyimide foil to ensure proper surface contact, see right image in figure 67. The compliance of the experiment with the acceptance criteria motivates to investigate the root cause of the observed anomalies further.

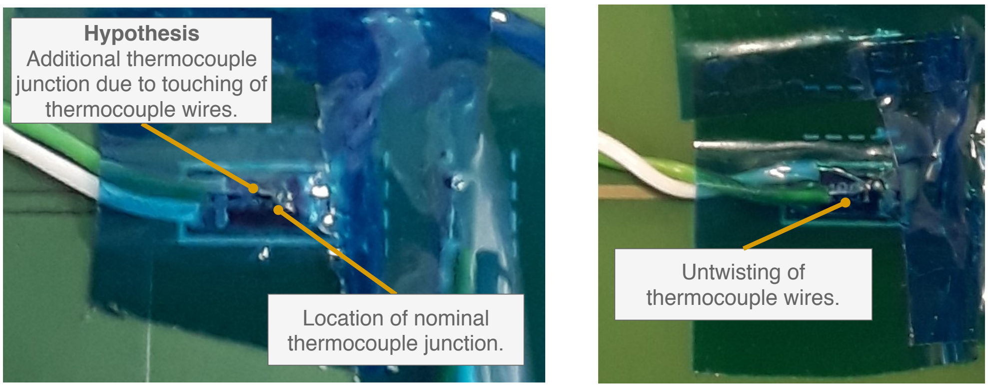

(a) (b)

Figure 67: Potential error in the thermocouple application during the first test campaign. (a) Touching of the thermocouple wires potentially creates an additional thermocouple junction without direct contact to the heat source (Test board VI on 26.09). (b) Untwisting of the thermocouple wires during subsequent test results in successful measurement (Test board I on 27.09).

8.4.3 Second test campaign – Failure investigation

The previous test campaign shows two primary anomalies. The first are the visible deviations in the temperature plots from the steady-state temperature equilibrium. The second are the recurring issues that the ambient pressure measurements show higher temperature increases than the vacuum measurements. This section describes the approach to investigate the measurement issues further, see the following bullet point list for the steps taken.

- Re-testing of the first test campaign to check if the anomalies persist.
- Comparison with the ESATAN numerical simulation model.
- Validation against thermal IR measurements.
- Investigation of the conductive heat loss through the thermocouples wires.
- Validation against measurements using thermal epoxy to apply the thermocouples.

The investigation shows that loss in contact pressure between the thermocouple and the heat source is the reason for the observed anomalies. This conclusion disproves the hypothesis of the previous section that an additional thermocouple explains the issues.

Re-testing of the analysis cases in the first test campaign

Re-testing enables to check whether anomalies persist. The recurrence of anomalies indicates systematic errors in the experimental set-up.

Table 35 summarizes the results of the second test campaign, which repeats several experiments of the first campaign. The first two experiments, case VI and VIII, comply with the acceptance criteria. The successful experiments motivate to continue the re-testing for the remaining test boards. However, the experiments of board I and II show the same anomalies like in the first test campaign, i.e., visible deviations in the measurement plot from the steady-state behavior and ambient experiments showing higher temperature increases than vacuum tests. The inconsistency in the anomalies indicates an error in the measurement set-up.

Table 35: Overview of the results of the second test campaign as a follow-up of the first test campaign described in table 34. The symbol (✓) indicates compliance with all acceptance criteria. Non-compliance is indicated by the identifier of the corresponding criterion.

Date	Description	Acceptance	Description / Anomaly
08.10	Case VI (vac. and amb.)	✓	Successful test, see figures 83a and 83b.
09.10	Case VIII (vac. and amb.)	✓	Successful test, see figures 84a and 84b.
10.10	Case II (vac. and amb.)	(c)	Ambient measurement shows higher temperature increase than vacuum measurement, see figures 81a and 81b.
11.10	Case I (vac.)	(b)	Deviation from the steady-state behavior visible in measurement plot, see figure 80b.
12.10	Case I (vac. and amb.)	(b)	Deviation from the steady-state behavior visible in measurement plot, see figure 80b.
16.10	Case I (vac.)	(b)	Deviation from the steady-state behavior visible in measurement plot, see figure 80b.

Comparison with the numerical simulation model

The measurements of the test cases VI and VIII show alignment with the numerical simulation results, see graphs in the figures 68a and 69a. The relative error between simulation model and experiment remains below 30% in both cases.

The low relative error provides confidence that the simulation model predicts the experimental behavior correctly. On the other hand, the alignment leaves ambiguity about the question if the experimental set-up is flawless.

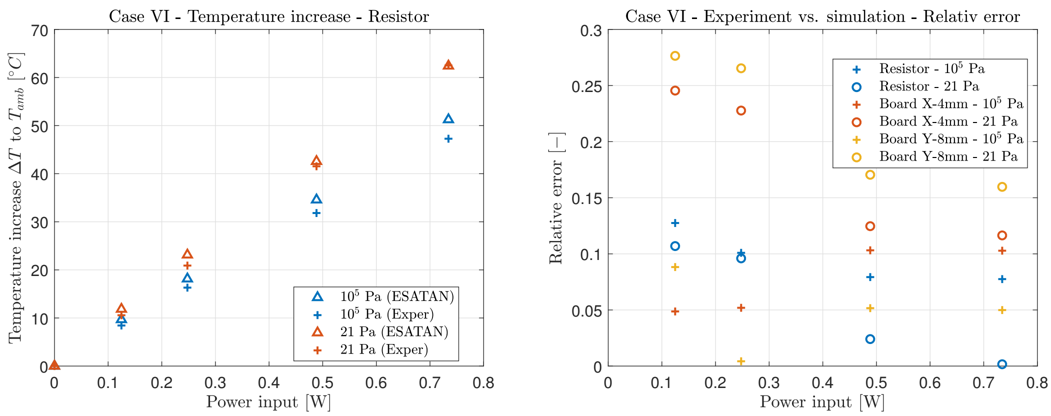

(a) (b)

Figure 68: Comparison of the ESATAN simulation model with the thermocouple measurements of the board VI. (a) Comparison temperature measurement at ambient and low-pressure. (b) Relative temperature error between simulation and experiment.

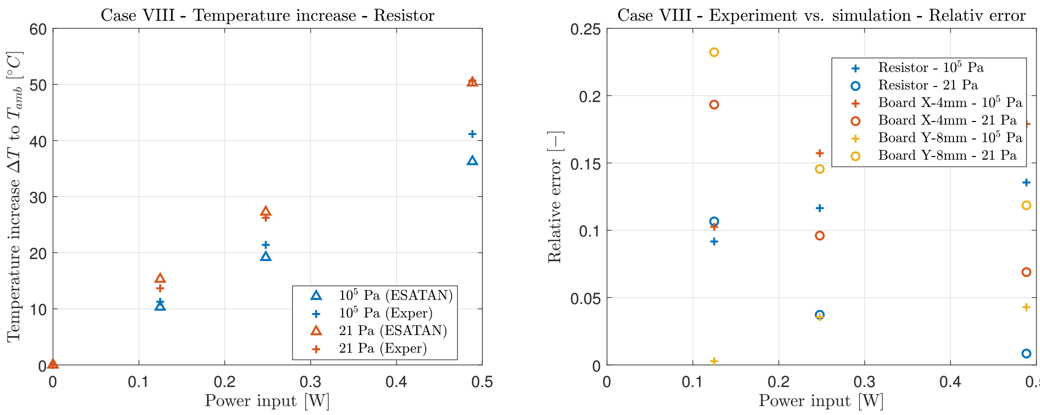

(a) (b)

Figure 69: Comparison of the ESATAN simulation model with the thermocouple measurements of the board VIII. (a) Comparison temperature measurement at ambient and low-pressure. (b) Relative temperature error between simulation and experiment.

Validation against thermal IR measurements

The application of a different measurement technique enables to validate the experimental set-up. The comparison of thermal IR measurement with thermocouple read out demonstrates a systematic error in the thermocouple measurements.

The graph in figure 70a compares the temperature profile when measuring a test board with thermocouples and the IR camera. Both measurement plots align for the first, three heat input but deviate for the last measurement point. The decrease in the measurement graph of the thermocouple confirms that loss of contact pressure is the reason for the visible deviations in the temperature plots.

Moreover, the comparison shows that the measured equilibrium temperature of the two techniques deviates. The temperature difference between the thermocouple and IR data scales with the power inputs. Further investigation on the apparent anomalies of test board I, show the effect more prominently, see the deviation between the ambient measurements indicated through the horizontal lines in figure 70b.

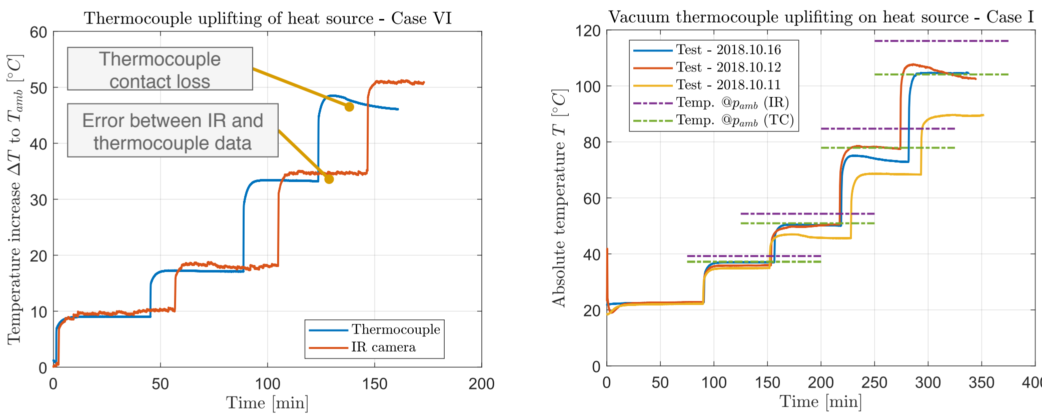

(a) (b)

Figure 70: Thermocouple contact loss visible in temperature plot. (a) Ambient measurement of the Case VI during the first test campaign. (b) Comparison of the vacuum temperature plots of the board I with the ambient measurements. The temperature equilibrium at ambient pressure is indicated by the horizontal lines, which describe both the thermocouple (green) and thermal IR measurement (purple).

The graphs in figure 71a to 71d show the difference between thermocouple and IR measurement for four test boards. The presence of temperature errors in three out of four measurements confirms a systematic error between the two techniques. Moreover, the graphs indicate that the temperature error scales linearly with temperature.

The performance characterization in chapter 3 highlights the challenges with thermal IR imaging and particularly the emissivity. Incorrect emissivity settings yield measurement errors that scale in temperature, see the emissivity error of the ArduinoUNO board in figure 12b. The calibration of the test board determines the emissivity at a resistor temperature around $70°C$, see figure 56b, which corresponds to the third temperature equilibrium point in figure 70b. The calibration implies that the error between IR camera and thermocouple should scale as the measurement temperature moves away from the calibration point. However, the graph shows the opposite behavior, which confirms that incorrect emissivity settings are insufficient to explain the observed behavior.

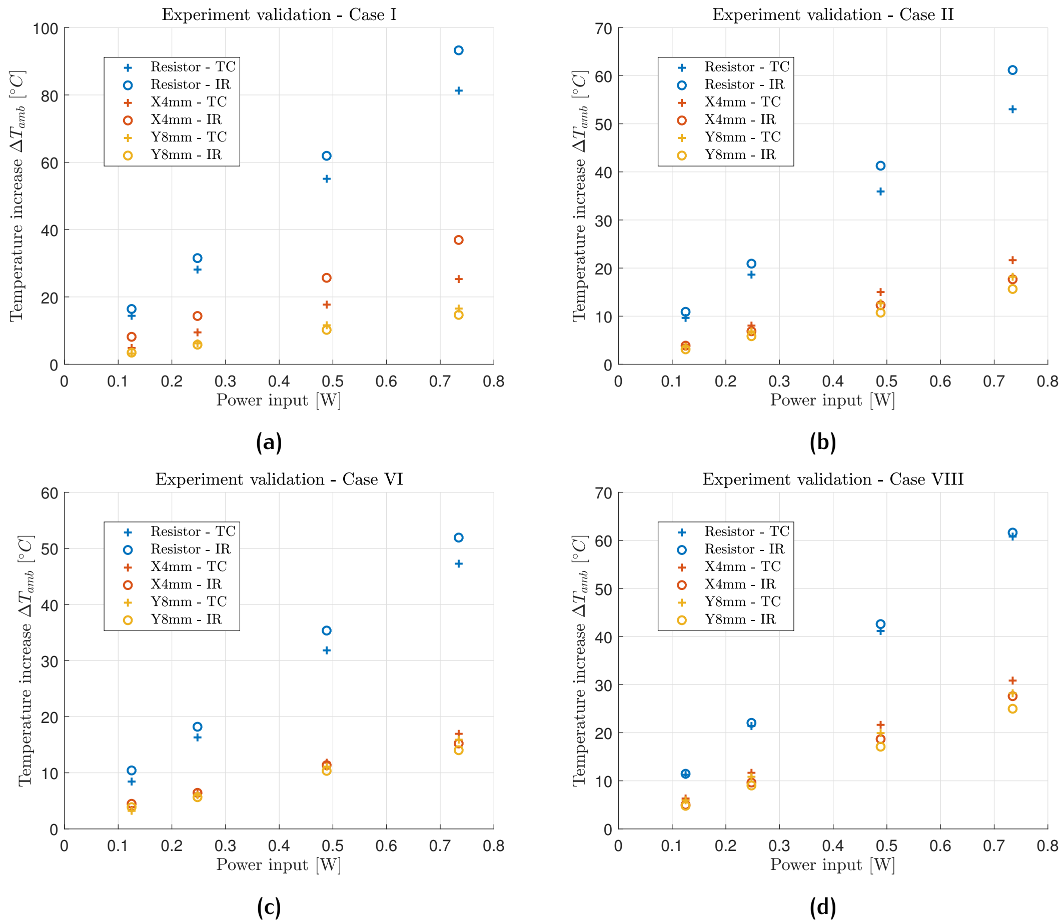

Figure 71: Comparison thermocouple and IR measurements at ambient pressure conditions. (a) Case I. (b) Case II. (c) Case VI. (d) Case VIII.

Heat loss through the thermocouple wires

The difference between thermocouple and thermal IR measurement scales with temperature. The scaling of the temperature error indicates that conductive heat loss through the thermocouple wires may cause the difference between the two measurement techniques.

A comparison of the IR images of the test board with and without thermocouple shows that the application of a taped thermocouple smears out the sharp temperature gradients that are visible in the IR image of the blank test board, see the camera images in figure 72a and 72b. The smearing occurs evenly over the resistor without a clearly distinguishable heat flow through the thermocouple wires.

An estimation of the heat loss through the thermocouples using the IR measurement shows that the heat loss through the thermocouple wires is negligible. The application of a thermocouple with adhesive confirms this conclusion, see next sections.

$$\dot{Q}_{loss} = \frac{\lambda_{Cr} A_{AWG\,32}}{l} \Delta T = \frac{\lambda_{Cr} A_{AWG\,32}}{8.6mm} 10K = 2mW \qquad \dot{Q}_{supplied} = 400mW \tag{35}$$

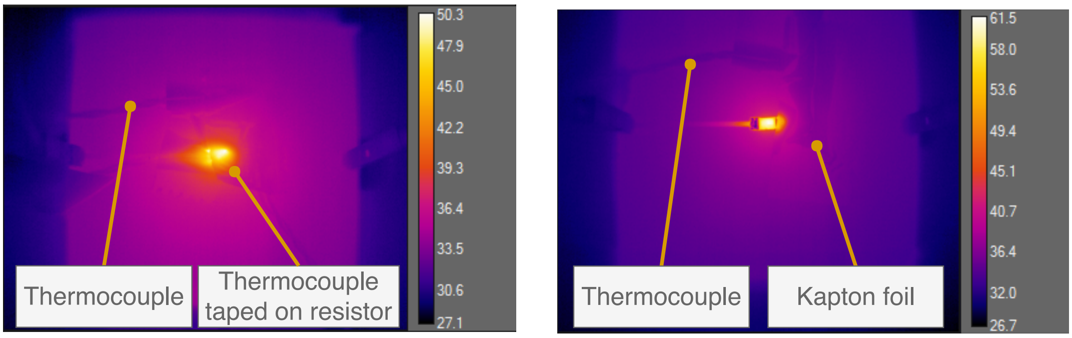

(a)

(b)

Figure 72: IR image of a test board (a) with and (b) without a thermocouple taped to the resistor.

Validation against different thermocouple application technique

The comparison of IR and thermocouple measurements shows that loss in contact pressure is responsible for the visible deviations of the thermocouple read-out from the equilibrium temperatures. However, what is missing is a proof that loss in contact pressure is also responsible for the anomalies of the vacuum measurements, which yield a lower temperature increase than experiments at ambient pressure. The application of thermally conductive adhesive ensures contact between thermocouple and resistor regardless of the pressure condition.

The modified application technique yields alignment between the thermocouple and IR measurements, see figure 73b and 73c. Moreover, the gluing of the thermocouples removes the previously observed anomaly of ambient temperature increases being higher than the vacuum measurement. The results of the glued thermocouples prove the hypothesis that the non-compliance with the acceptance criterion (c) is due to an erroneous measurement technique.

The alignment between IR and glued thermocouple measurement confirms, moreover, that the heat conduction through the thermocouple wires is negligible. The differences between IR and thermocouple measurements would persist if the thermocouple wires were providing a significant heat leakage. The alignment, furthermore, validates that thermal IR imaging provides a reliable measurement technique for the test boards, and thus PocketQube subsystem boards.

The glued thermocouples show a higher temperature increase than the taped thermocouples, see figure 73d. The difference between the measurement techniques makes the previous ESATAN validation obsolete, see further discussion on the model validation below. The alignment of the taped thermocouple measurement with the ESATAN simulation model highlights, first, that an insufficient contact pressure between thermocouple and heat source can remain unnoticed in the measurement plot and, second, that the comparison of an invalidated simulation model with an invalidated measurement technique can lead to false conclusions.

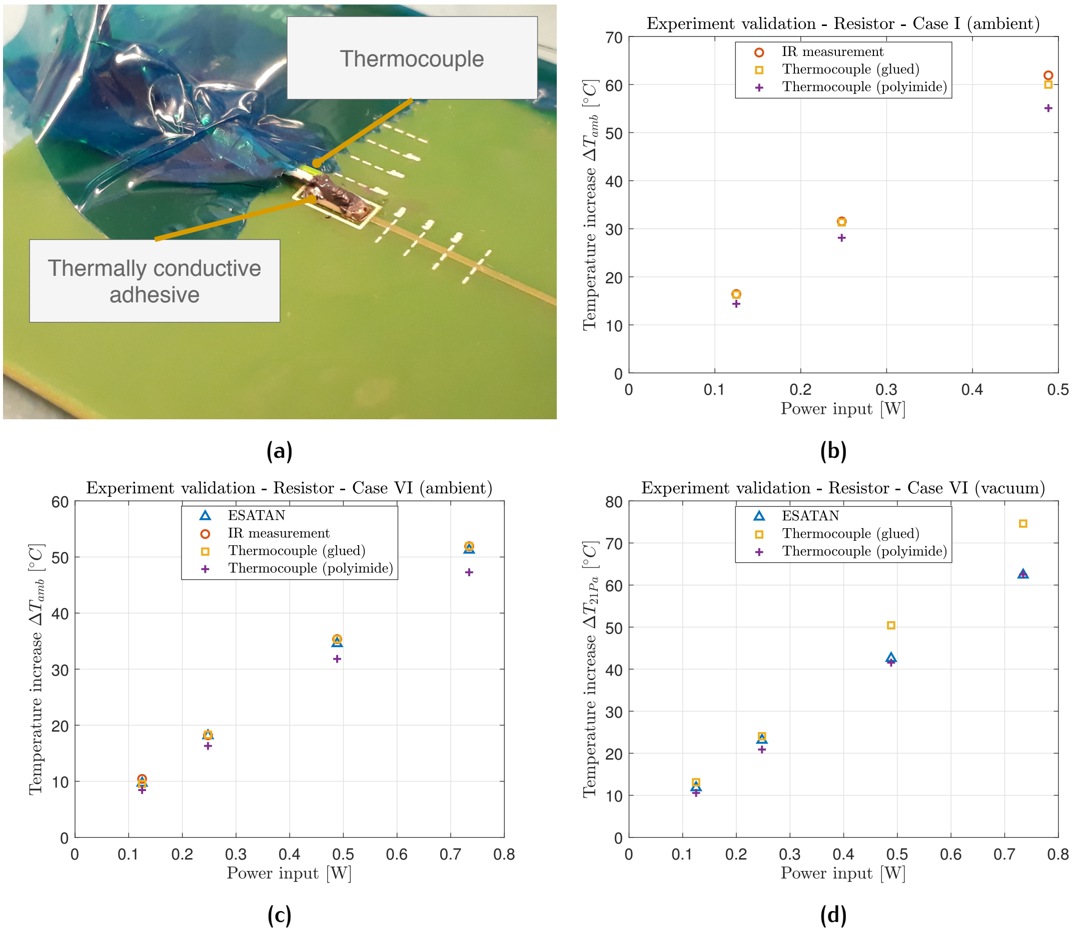

Figure 73: Comparison thermocouple application techniques (a) Application of thermocouple to heat source using thermally conductive adhesive. Comparison of temperature acquisition techniques: (b) Case I ambient pressure. (c) Case VI ambient and (d) vacuum pressure.

Thermocouple contact loss – Discussion of the measurement error root cause

The gluing of the thermocouples provides the final evidence that contact loss is responsible for the observed measurement anomalies. This section discusses why thermo-mechanical effects present the most likely explanation for the contact loss and the scaling of the temperature error.

The thermocouples application techniques builds on adhesive polyimide tape. A potential explanation for the contact loss is that the adhesive strength of the tape decreases continuously over the measurement period. The measurement plot in figure 70a shows that the thermocouple measurement is stable in time and that deviations from the IR measurement occur with changes in temperature instead of time.

Differential thermal expansion between the polyimide foil, resistor and thermocouples provides an explanation for the measurement error. The coefficient of thermal expansion describes how much a material expands or contracts in response to temperature changes. Table 36 compares the expansion coefficient for the materials relevant to the measurement set-up. The polyimide foil shows the largest coefficient of thermal expansion, which means that tape expands relative to the other components. The relative expansion of the tape reduces the contact pressure between thermocouple and resistor. The decrease in contact pressure results in the measurement difference compared to the contactless IR imaging. The differential thermal expansion, moreover, explains why signs of contact loss through visual inspection after the testing.

Table 36: Overview of the coefficient of thermal expansion for various materials employed in the measurement set-up. The abbreviation CTE refers to coefficient of thermal expansion.

Component	Material	CTE $[10^{-6}/K]$	Reference
Adhesive tape	Polyimide	30-70	(Jeon et al., 2018; Song et al., 2014)
SMD resistor (body)	Ceramic	6	(Lau et al., 1987; Suhling et al., 1994)
PCB	Copper	17	(Jeon et al., 2018)
PCB	FR4	15	(Lau et al., 1987)
Thermocouple	Chromel	13	(Omega Engineering, 2005)
Thermocouple	Alumel	12	(Omega Engineering, 2005)

8.4.4 Measurement error correction

The differential thermo-mechanical expansion provides an explanation why for the systematic measurement error of the taped thermocouples. The systematicality motivates characterizing the error to correct the taped thermocouple measurements.

The scatter plot in figure 74a shows the error between taped thermocouple and the two alternative measurement techniques. The plot compares the ambient measurements with the IR read out and the vacuum measurement with the glued thermocouple read-outs considering the high fidelity of both techniques. The graph in figure 74b shows a linear curve fit through the measurement with largest temperature error in figure 74a. The curve fit describes the maximum error due to the loss of contact in the taped thermocouple measurements.

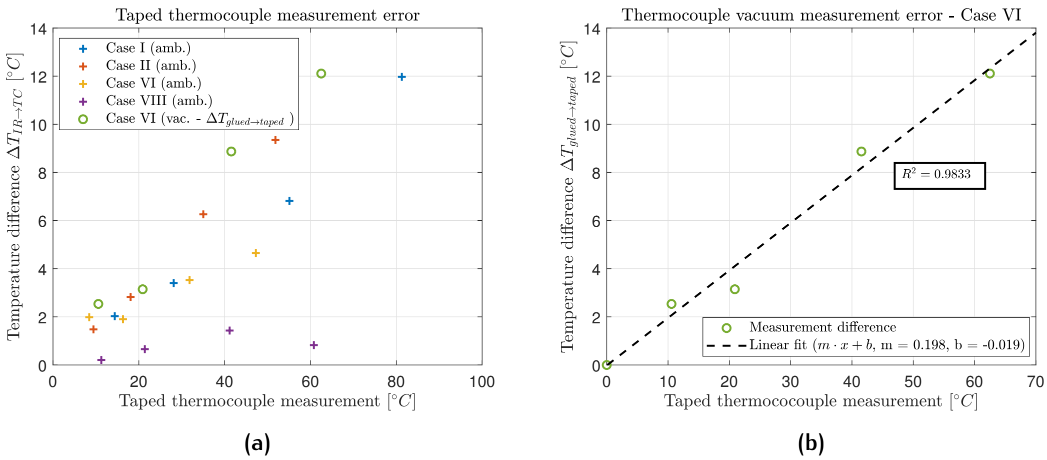

Figure 74: Thermocouple measurement error using taped thermocouple. (a) Error in between thermocouple measurement techniques. (b) Correction using the largest thermocouple error during the vacuum measurement of Case VI. Fitting a correction graph through the measurement.

The error graph enables to correct the taped thermocouple measurements of the board VIII. The measurement points in figure 74b show the ambient and vacuum temperature increase of three test boards. The measurement points provide a starting point for the implementation of the thermal screening method, see application to the Delfi-PQ case study in the next section.

The measurement points indicate a linear behavior between ambient and vacuum temperature increase. The linear behavior is reasonable considering that the convective and radiative heat transfer are linearizable with respect to the temperature difference between object and environment, see discussion on equation 27.

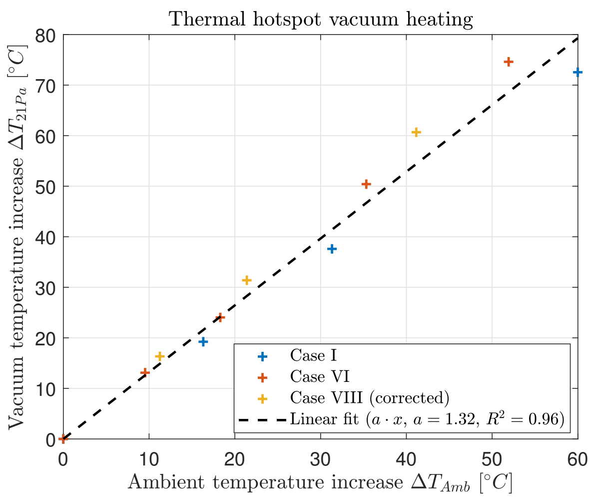

Figure 75: Overview of the vacuum temperature increase measured with the glued thermocouple (Case I and VI) and the corrected measurement graph VIII.

8.4.5 Application of thermal screening method to Delfi-PQ case study

The test board VIII severs as a reference case for the power amplifier on the Delfi-PQ communication board, both in terms of board layout and component size, see discussion in chapter 6. The operation of the power amplifier constitutes a critical scenario concerning hotspot overheating. Therefore, the test board provide a case study to demonstrate the application of the thermal screening method.

Table 37 details the steps to estimate the worst-case flight temperature of the hotspot. The analysis shows that the maximum temperature remains below the operational temperature limit of 85°C (RFMD, 2018) . The step (3) illustrates that the vacuum temperature increase includes the estimation of the taped thermocouple error and the additional temperature increase due to the vacuum quality of the available test facility.

Table 37: Application of the thermal screening methodology to Delfi-PQ power amplifier, the most critical component concerning overheating. The symbol (✓) indicates compliance with the operational temperature limit according to the thermal screening method.

Step	Description	Parameter	Temperature [°C]
(1)	Maximum board temperature predicted with satellite simulation model (Avila de Luis, 2018)	$T_{max,board}$	42
(2)	Ambient temperature increase ($P_{dis} = 0.5W$)	ΔT_{op}	+ 21.4
(3)	Vacuum temperature increase (measured) Thermocouple vacuum error Vacuum quality test facility (simulated)	$\Delta T_{amb \rightarrow 21Pa}$ $\Delta T_{TC\,err}$ $\Delta T_{21Pa \rightarrow 0Pa}$	+ 4.8 + 5.2 + 2.3
(4)	Thermal model uncertainty margin	$\Delta T_{uncertainty}$	+ 8
(5)	Total temperature of the component	T_{total}	= 83.7
	Margin to hardware temperature limit	T_{margin}	$1.3 > 0$ (✓)

8.5 SECONDARY TEST OBJECTIVE (A) – RESULT

The secondary test objective (a) aims at determining the effectiveness of board-level design solutions in reducing the temperature of a thermal hotspot. The thermal resistance analysis in chapter 5 identifies PCB layout characteristics and describes their impact on the conductive heat sinking from a hotspot through a subsystem board. The experimental campaign compares the layout parameters by measuring the hotspot temperature using the IR camera at ambient conditions, see image of the test set-up in figure 59b.

Table 38 shows the decrease in the hotspot temperature with each of the design measures. The design parameters range from the worst (I) to the best-case (VII) in terms of thermal conductivity through the board. The table shows that locating a thermal hotspot on a continuous copper plane is the most effective way to reduce its temperature. The comparison highlights that the application of the six thermal VIAs in the worst-case board layout is as effective as placing a component on a continuous copper plane. The results, therefore, confirm the qualitative outcome of the thermal resistance analysis in chapter 5.

The graph in figure 76a shows the experimental results for the various power inputs. The analysis uses the equivalent board conductance to quantify the impact of the design parameters in the conduction through a board, see chapter 5 for an explanation of modeling approach. The equivalent board conductance builds is an input to the conceptual three-node model used to predict the experimental behavior in chapter 6, see network schematic in figure 47a. The graph in figure 76b compares the results of conceptual analysis with the experiments. The comparison with the fitted curve in figure 76a shows that modelling approach follows the same trend as the experimental results. However, the model deviates significantly from the experimental results at low conductances, particularly the lower three conductances. The three low conductances describe the test boards with a copper trace on top and the continuous copper plane on the opposite side of the hotspot, see board layout in figure 46. The misalignment leads to the conclusion that the equivalent board conductance analogy is insufficient for describing the thermal behavior. However, the conceptual model describes the experimental behavior of the remaining boards with a temperature error below $\pm 5K$ for power inputs of 125 and $250mW$. The low temperature error shows that the equivalent board conductance is appropriate for describing boards with a resistor on a continuous copper plane.

Table 38: Overview of the hotspot temperature decreases with each of the board-level design parameters for a $500mW$ heat input to the resistor. The board conductance C_{Board} refers to the results of the thermal resistance analysis in chapter 5. The third column contains the measured temperatures, whereas the fourth column shows results of power fit through the experimental results, see figure 76a.

Test ID	Description	C_{Board} $10^{-3}[W/K]$	Temp. decrease $500mW$ (exp.) $[K]$	Temp. decrease $500mW$ (fit) $[K]$
I	GND on back	2.6	-	-
III	2x VIA below	8.3	−11.9	−14
IV	2x VIA below & 4x adjacent	13.0	−9.0	−4.7
II	GND on top	19.2	−0.1	−3.8
V	Four-layer PCB	22.2	−5.8	−1.4
VI	2x VIA below	43.2	−0.1	−5.9
VII	2x VIA below & 4x adjacent	56.0	−6.5	−2.1

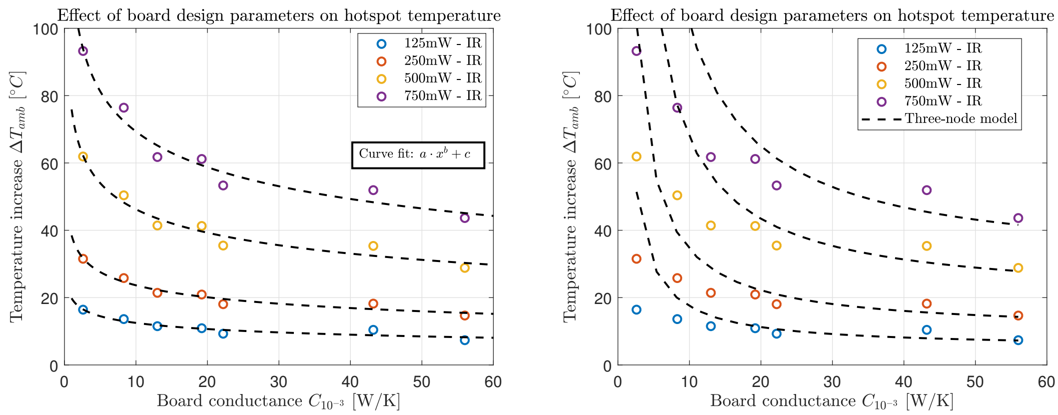

(a) (b)

Figure 76: Experimental IR measurements for the secondary test objective. (a) Resistor temperature increase as a function of the board-level thermal conductivity. (b) Comparison of the experimental results with the analytical prediction following the three-node thermal resistance model in figure 47a.

8.6 SECONDARY TEST OBJECTIVE (B) – RESULTS

The secondary objective (B) aims at validating the thermal models of the test boards, see chapter 7 for a description of the modelling approach. The hypothesis is that a two-point validation of the simulation model at ambient ($10^5 Pa$) and fine vacuum ($21 Pa$) conditions provides confidence in using use the simulation model to determine the temperature increase between fine and ideal ($0 Pa$) vacuum. The temperature increase accounts for the vacuum quality of the test facility used for this study. Quantification of the error enables to correct the diagram in figure 75. The temperature increase equals the error of performing thermal-vacuum testing at moderate pressure levels compared to the recommended threshold in environmental test standards (ECSS, 2016). Moreover, quantification of the temperature error provides a baseline to choose the appropriate pressure level for thermal-vacuum testing of PocketQubes.

The model validation requires a criterion to judge if simulation and experiment align sufficiently. The following threshold derives from the literature (Gilmore, 2002; Welch, 2016) and thermal balance testing for nanosatellites (Mason et al., 2017; Kang and Oh, 2016).

The numerical simulation model is validated if the temperature error between numerical simulation and experiment remains below $\pm 3K$ for all measurement points.

8.6.1 Validation ambient pressure measurement

The validation of the numerical model against the experiments at ambient ($10^5 Pa$) pressure uses the measurements by the IR camera because it provides reliable results. Table 39 summarizes which model satisfies the validation criterion considering the three measurement locations, introduced in figure 60.

The validation shows that the simulation model of the boards with a single resistor mounted on a continuous copper plane (board II to VI) , i.e., board II to VI, align with the experiments. However, the simulation model deviates significantly from the experiment for a copper trace and FR4 layer on top (board I).

Table 39: Validation of the ESATAN numerical simulation results against the ambient measurement results provided by the thermal IR camera. The (✓) symbolizes compliance with the validation criterion, whereas the (✗) marks non-compliance. The magnitude of the error between simulation and experiment is shown in the appendix, see figure 86a to 86e.

Test ID	Validation - Resistor	Validation - Board X4mm	Validation - Board Y8mm
I	✗	✓	✓
II	✓	✓	✓
V	✗	✓	✓
VI	✓	✓	✓
VIII	✗	✓	✓

A comparison between the temperature map by the simulation model and IR camera shows qualitative alignment of the temperature distribution, see temperature maps in figure 77a and 77b. However, the measured and predicted temperature increase of the resistor show a substantial difference. The resistor temperature by the simulation is double the temperature of the experiment. The qualitative alignment of the board's temperature distribution indicates a modelling error in both the conductive resistance between resistor and board and between the FR4 layer and copper trace, see figure 52b for the modelling schematic of the embedded trace.

Modelling the trace as a separate shell element with conductive resistances connecting each trace element with the FR4 layer provides a $15K$ improvement in reducing the temperature difference for the $500mW$ example. However, the temperature difference remains unsatisfactorily high considering the validation criterion.

8.6.2 Validation vacuum pressure measurement

The validation against the vacuum ($21Pa$) experiments uses the measurement with the glued thermocouple and the tape measurements using the graph in figure 74b for correction. Table 39 shows which simulation models satisfy the validation criterion for both vacuum and ambient measurement.

Table 40: Validation of the ESATAN numerical simulation results against the vacuum measurement results. The annotation (corr.) refers to the measurements with the application of the measurement correction factor. The (✓) symbolizes compliance with the validation criterion, whereas the (✗) marks non-compliance. The magnitude of the error between simulation and experiment is shown in the appendix, see figure 87a to 87d.

Test ID	Resistor (vac.)	Board X4mm (vac.)	Board Y8mm (vac.)	Resistor (amb.)	Board X4mm (amb.)	Board Y8mm (amb.)
I	✗	✗	✓	✗	✓	✓
II (corr.)	✗	✗	✗	✓	✓	✓
VI	✗	✓	✗	✓	✓	✓
VIII (corr.)	✗	✓	✓	✗	✓	✓

The vacuum measurements further confirm the modelling errors of the board I. Moreover, the validation shows that the simulation results of board II and VI align with the experiment at ambient but not at vacuum conditions. This results implies that either the previous alignment is coincidental or that the simulation of the vacuum conditions is incorrect. The following subsection discusses the validity of several model assumptions and elaborates on their plausibility for explaining the model deviation.

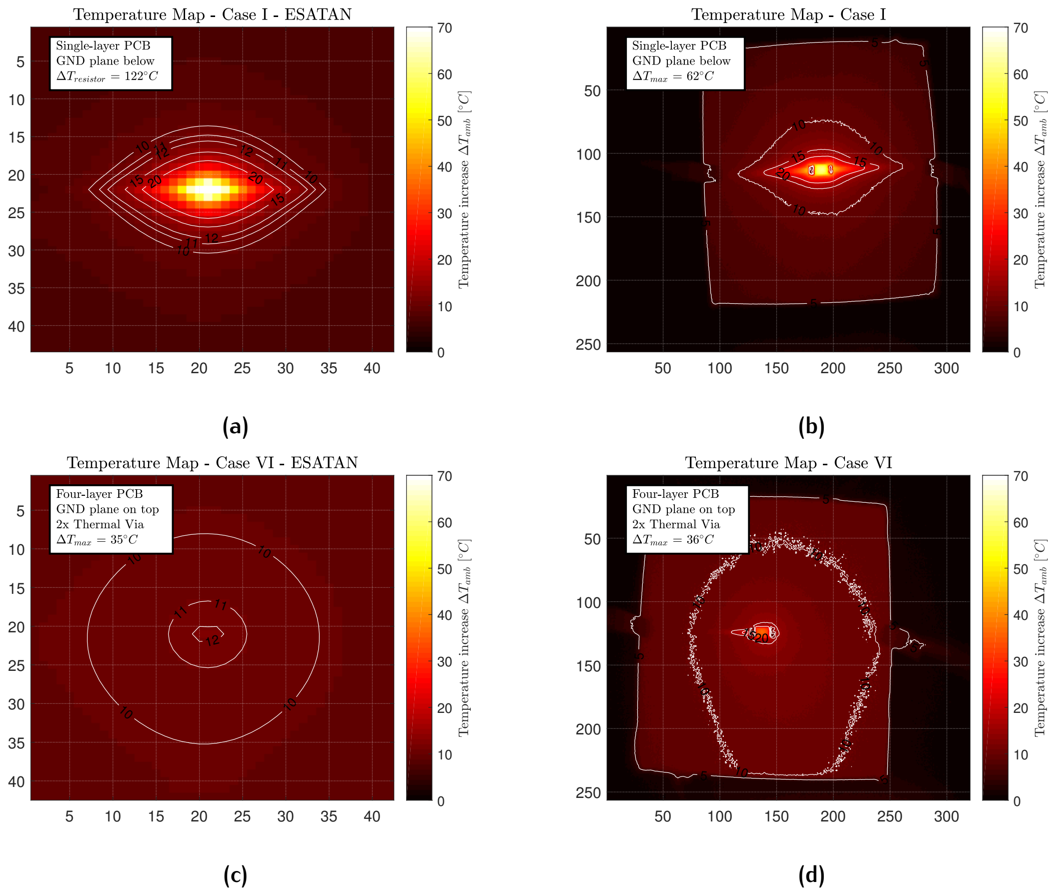

Figure 77: Temperature map comparison between numerical simulation and IR measurement for a power input of $500mW$. The numerical temperature maps show only the board's temperature distribution considering that the resistor is modelled as a non-gemetrical thermal node, see modelling schematic in figure 53. The resistor temperature increase is given in the white annotation boy. (a) ESATAN model case I. (b) IR temperature map case I. (c) ESATAN model case VI. (d) IR temperature map case VI.

8.6.3 Discussion modelling assumptions

The modelling approach relies on several assumptions. The steady-state heat balance of the simplified, three-node resistance network highlights which parameters influence the temperature increase of the resistor, see figure 58a for the network schematic. Table 41 summarizes the model parameters and their corresponding assumptions. The experiments in vacuum yield higher temperatures than the measurements at ambient conditions. The discussion, therefore, focuses on temperature dependencies of the model parameters.

$$\Delta T = T_{res} - T_{amb} = \dot{Q}_{in} \left[\frac{1}{\frac{1}{1/C_{res}+1/C_{board}}} + \frac{1}{h_{conv}A + 4\sigma A \epsilon T_m^3} \right] \tag{36}$$

The heat input to the systems, $\dot{Q}_{in}$, equals to power dissipation over the resistor. The power dissipation depends on the supply voltage and the electrical resistance. The power supply unit provides a constant voltage supply, whereas the electrical resistivity changes as a function of temperature. However, the resistor temperature during the experiments yields a maximum change of 0.5% in the electrical resistivity (Zandman and Szwarc, 2008), which is too small to explain the model deviations.

The model of ambient and vacuum measurement are identical apart from the natural convection heat transfer coefficient, h_{conv}, see modelling approach in figure 53. The misalignment

Table 41: Overview of the parameters and assumptions for the detailed simulation model described in chapter 7.

Parameter	Modelling assumption
$\dot{Q}_{in}$	The power dissipation is a function of the supply voltage, assumed constant in time, and the electrical resistance, assumed constant in temperature.
h_{conv}	The model uses experimentally derived graphs for h_{conv}, see figure 29b .
ϵ	Constant temperature and wavelength, deriving from IR calibration.
C_{res}	Temperature-independent conductive resistance, value taken from datasheet (Vishay, 2010).
C_{Board}	Temperature-independent thermal conductivity, values taken from (Gilmore, 2002; Graebner and Azar, 1997).

of the vacuum measurements indicates an error in the convection coefficient. The simulation of radiation only, $h_{conv} = 0$, still shows a lower temperature than the experiment, see yellow triangles in figure 29b. This outcome shows that an error in the natural convection heat transfer coefficient misses to explain why the simulation model predicts lower temperatures than the experiment in vacuum.

The radiative heat transfer depends on the emissivity, which is both wavelength- and temperature-dependent, $\epsilon(T, \lambda)$. The emissivity calibration of the test item shows a constant emissivity over a temperature range of $50 - 70°C$, which align with findings in the literature (Svasta et al., 2004). The constant behavior, therefore, provides an improbable explanation for the deviation between experiment and simulation, which scales with temperature.

The conductive heat transfer depends on the thermal conductivity of the materials. The conduction between resistor and board, C_{res}, as a function of the solder's thermal conductivity. And, the conduction through the PCB, C_{board}, depends on the thermal conductivity of copper and FR4, with copper being the dominant parameter for the conductive heat transfer as the thermal resistance analysis in chapter 5 shows. The literature describes that both the thermal conductivity of solder (Aksöz et al., 2013) and copper (Sidles and Danielson, 1951) decrease with temperature. The decrease in thermal conductivity reduces the thermal conductance, which an increase in the temperature gradients, see equation 37. The temperature dependency of the thermal conductivity, therefore, provide an explanation why the simulation model predicts lower temperatures than the experiment.

$$C(T) = (\lambda(T) A) / l \qquad \Delta T = \dot{Q} / C \tag{37}$$

The validation considers three measurement points, on the resistor and two on the board. The simulation model shows better alignment with the experimental results for the board than for the resistor. The difference between the measurement points indicates that the temperature-dependency of the solder's thermal conductivity is responsible for the unsuccessful validation. The scatter plots in figure 78b show the error between simulation and experiment as a function of the resistor conductance. The analysis considers the board VI as a case study because the simulation shows alignment at ambient but not in vacuum and high-fidelity temperature measurements are available by the glued thermocouples.

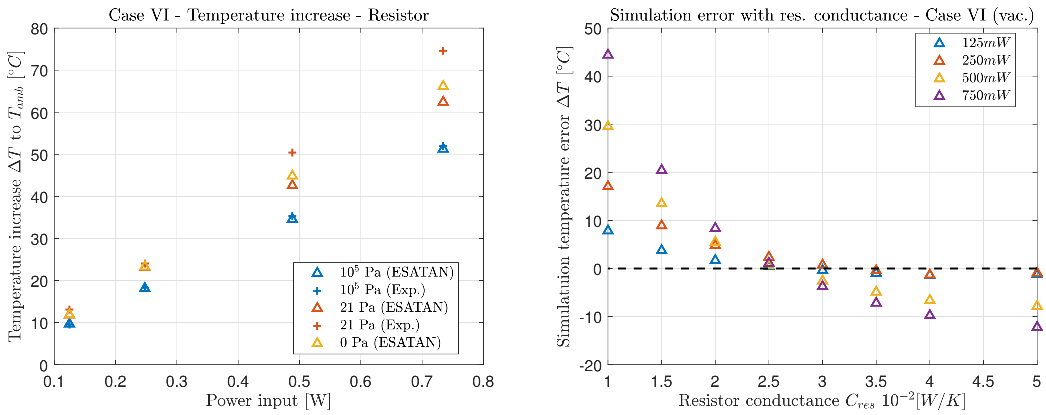

(a) (b)

Figure 78: Simulation model sensitivity to thermal analysis parameters. (a) Comparison between the simulation model of the board VI and the experimental results. The yellow triangles indicate the temperature increase in the complete absence of natural convection phenomena. (b) Error between simulation model and experiment as a function of the resistor conductance, C_{res}.

The sensitivity of the resistor temperature to the conductance strengthens the hypothesis that the temperature dependency of the thermal conductivity explains the unsuccessful validation. Table 42 summarizes the previous discussion indicating which parameter is most likely to explain the observed behavior.

Table 42: Plausibility of the model parameters in explaining the misalignment between simulation and experiment at vacuum conditions.

Parameter	Plausability	Rationale
C_{res}	Most likely	The thermal conductivity of solder decreases with temperature.
C_{Board}	Likely	The thermal conductivity of copper, the dominant material for conductive heat transfer in PCBs , decreases with temperature.
h_{conv}	Unlikely	The simulation of the radiation-only case shows that an incorrect description of h_{conv} cannot explain the deviations.
ϵ	Unlikely	The emissivity is constant over part of the temperature range.
$\dot{Q}$	Unlikely	The temperature dependency of the power dissipation is insignificant.

The misalignment between simulation and experiment leads to a non-compliance with the secondary test objective (B). The modelling assumptions on the temperature dependency of the thermal conductivity explain the deviation between experiment and simulation. However, an insufficient number of measurements are available to validate that the hypothesis.

The objective of the validation is to obtain a high-fidelity simulation model to quantify the temperature error due to residual gas at low pressures. The simulation model in figure 78a shows that the temperature difference between fine ($21Pa$) and ideal vacuum ($0Pa$) remains below $5K$ in all measurement points, see the difference between red and yellow triangles. However, validation of the simulation model is missing. The simplest way to characterize the error is to repeat the measurement in a facility of higher vacuum quality than those used in this project.

8.7 SUMMARY TEST RESULTS

The diagram of the hotspot vacuum heating provides a starting point for the implementation of the thermal screening method. The three subsystem boards describe the hotspot behavior concerning two geometric sizes and board layouts. The measurement issues with the taped thermocouples prohibit the investigation of all test scenarios outlined in chapter 6. The limited number of analysis cases compared to the available test boards leads to a partial fulfillment of the primary test objective. However, the Delfi-PQ case study demonstrates that the methodology is already applicable to assess the temperature compliance of a hotspot component. The investigation of the root cause for the observed measurement anomalies provides alternative measurement techniques to continue this research.

The IR camera enables to test all subsystem boards at ambient conditions. The analysis of the hotspot temperature results in PCB layout guideline to mitigate critical thermal hotspots. The analysis of all test boards leads to a fulfillment of the secondary test objective (A).

The thermal simulation models indicate that performing thermal-vacuum testing in the fine vacuum regime results in temperature errors below $5K$. However, final validation of the numerical simulation model is missing because simulation and experiment deviate for the low-pressure case. The missing validation leads to a non-fulfillment with the secondary test objective (B). The simplest way to further investigate the temperature error is to repeat the vacuum measurement in a test facility of higher vacuum quality than those used in this study.

Table 43: Overview of the test results considering the test objectives.

Test objective	Description (shortened)	Fulfillment
Primary	To characterize the vacuum temperature increase of local thermal hotspots.	Partial
Secondary (A)	To compare how board-level design solutions perform in reducing temperature loads of local thermal hotspot.	Full
Secondary (B)	To determine the temperature error of performing thermal-vacuum testing at moderate pressure levels through validation of a numerical simulation model.	None

9 CONCLUSIONS

This chapter concludes the research project by answering the research questions stated in the introduction. The three sub-questions support the answer to the primary research question.

What are necessary elements to facilitate quick testing and re-design of PocketQube subsystems?

The second chapter of this report introduces a thermal screening method to scan PocketQube subsystems for thermal hotspots and verify compliance against the hot-side temperature requirements. Key elements of the methodology are a temperature screen at ambient conditions using a thermal IR camera and experimentally derived diagrams to estimate how much thermal hotspots heat up under vacuum conditions. The Delfi-PQ case study demonstrates how to perform a quick judgment call whether a hotspot experiences critical temperatures during flight. The test method omits the necessity to perform thermal-vacuum testing to estimate the maximum flight temperature. The methodology contributes, therefore, to the development of cost- and time-effective test strategies for PocketQube subsystems.

The chapters of this report describe the process of implementing the thermal screening method. The ArduinoUNO case study and experimental test campaign demonstrate that thermal IR imaging is a viable tool to identify hotspots and measure their temperature. The experimental test campaign results in a diagram that describes the vacuum heating of thermal hotspots. The diagram is necessary to estimate the maximum flight temperature of a hotspot. Moreover, the experimental study provides PCB layout options to mitigate overheating of a thermal hotspot. The description of design options complements the thermal screening method.

The available diagram describes the thermal behavior of resistor hotspots. The resistors represent a worst-case scenario for the thermal behavior of SMDs. Larger semiconductor and IC components typically present better heating sinking capabilities because the heat transfer scales with the geometric size. The application of the available diagram to larger semiconductor components yields a conservative estimation of the maximum flight temperature.

An incorrect test set-up limits the number of available measurements to describe the hotspot behavior. The investigation of the root-cause for error yields alternative measurement techniques to repeat the unsuccessful experiments and expand the analysis.

What temperature measurement techniques are appropriate for PocketQube subsystem testing?

The thesis compares the performance of thermal LWIR imaging and thermocouple contact sensors in measuring the temperature of representative PocketQube components. The analysis uses the microcontroller of an ArduinoUNO and resistors on test PCBs as a case study to determine the performance of both measurement techniques.

The performance characterization demonstrates thermal LWIR imaging achieves the same accuracy as thermocouples in measuring the relative temperature increase of the representative components. Moreover, a thermal IR camera allows to capture the temperature distribution of an entire board and facilitate understanding of the board-level thermal behavior. Thermocouple contact measurements prove to be unreliable in measuring SMD resistors when being applied with adhesive polyimide tape. The application with thermally-conductive epoxy adhesives enables to overcome the reliability issues related to loss of contact pressure. However, the permanent application is inappropriate for flight hardware and multiple test campaigns with the subsystem boards. The comparison leads to the conclusion that IR imaging is the recommended temperature measurement technique for PocketQube subsystems.

Precise temperature measurements using IR imaging require calibration for the reflected background and emissivity of the body of interest. Digital image subtraction using a reference image taken from an inactive subsystem is a simple means to remove the disturbance of the reflected background radiation. The case study shows that surface reflection of the camera's IR emission dominates the background radiation. Moreover, IR temperature measurements require for emissivity correction. Digital emissivity correction is directly applicable to high-emissivity components, whereas for reflective components it is necessary to increase the local emissivity, e.g., through the application of a removable, high-emissivity paint. The case studies including the ArduinoUNO and PocketQube test boards provide reference values for the emissivity of PCBs and electronic components. Moreover, the report shows how to determine the emissivity of objects using a two-point emissivity calibration.

Which pressure levels are necessary to support thermal-vacuum testing of PocketQube subsystems?

This thesis investigates the temperature errors due to residual gas in vacuum testing. The analysis approach includes creating of thermal simulation models of the test boards used to answer the primary research question. Moreover, the analysis relies on the experimental derivation of the natural convection heat transfer coefficient at ambient ($10^5 Pa$) and subatmospheric pressures ($21 Pa$). The primary assumption is that successful validation at both pressure conditions provides confidence in using the model to determine the temperature difference relative to ideal vacuum conditions ($0 Pa$). The temperature difference equals the temperature error due to imperfections in the vacuum representation.

The numerical simulation shows that the temperature difference for a resistor hotspot between fine ($21 Pa$) and ideal vacuum ($0 Pa$) remains below $5K$ considering a maximum power dissipation of $750 mW$. The acceptable temperature error for thermal-vacuum testing depends on the test objective. This study uses thermal model correlation as a case study to establish a potential reference value for an acceptable temperature error. A statistical analysis of the deviations between simulation and flight data of nanosatellite missions yields a $\pm 8K$ (1σ) thermal model uncertainty margin. The temperature error remains below this threshold, which indicates that pressure requirements for thermal-vacuum testing can be moderated.

Final validation of the simulation model through testing at the two reference pressures is missing. The simplest way to characterize the temperature error further is repeat the vacuum measurements in a test chamber of higher vacuum quality than those used in this research project. The quantification of the temperature error could provide ultimate proof that pressure levels by four order larger than those used in environmental test standards for larger satellites suffice to maintain the error acceptably low.

What are effective design solutions to mitigate thermal issues?

This thesis report investigates thermal control solutions for PocketQubes both on a subsystem- and board-level. The subsystem-level analysis describes the thermal behavior of subsystems in a satellite assembly. The analysis builds on the thermal resistance analogy and uses the Delfi-PQ and SMOG-1 as reference cases. The study shows that seventy percent of the subsystem-level heat exchange occurs through radiation, primarily between adjacent subsystem boards. The importance of radiation makes the optical surface properties an effective parameter for thermal control to either reject or retain heat on subsystems.

The board-level study includes both analysis and experiments. On the board-level, heat transfer occurs primarily through conduction with copper dominating the thermal behavior. The analysis of PCB layouts characteristics focuses on design parameters to enhance conductive heat spreading to mitigate critical hotspots. The investigated spectrum of board layout options shows that it is possible to reduce the hotspot temperature by $30K$ for a $500 mW$ resistor hotspot. The most effective solution to reduce the temperature is to place the hotspot component on a continuous copper plane. Thermal VIAs provide an effective means to bypass the insulating PCB layers when the previous solution is impractical. The application of six thermal VIAs yields an equal temperature reduction as placing the component on a continuous copper plane. The analysis of layout parameters provides guidelines to design PocketQube subsystem boards for preventing critical hotspots, apart from providing re-design solutions in support of the thermal screening method.

Conclusive statements

The following final statements summarize the conclusions of this research project:

- The thermal screening method enables to perform a quick estimation of the maximum flight temperature of thermal hospots without thermal-vacuum testing.
- Thermal IR imaging is the recommended technique to measure the temperature of PCB-based subsystems.
- Taped thermocouples are unreliable in measuring SMD-resistor-sized objects.
- Effective means to reduce hotspot temperatures include placing the component on a continuous copper plane or adding thermal VIAs that connect with copper planes.
- The fine vacuum regime ($21 Pa$) suppresses natural convection effects sufficiently to maintain the resulting temperature errors below $5K$ for hotspot components with power dissipations below $750 mW$.

10 RECOMMENDATIONS

This chapter provides recommendations about future work that results from this thesis project.

10.1 THERMAL SCREENING METHOD

The incorrect measurement set-up limits the number of available graphs to describe the vacuum heating of thermal hotspots. The available diagram presents a worst-case scenario for the hotspot behavior. Future testing is necessary to improve the accuracy of the screening method.

1. **Repeat the vacuum experiments that used taped thermocouples by either applying the thermocouples with adhesive or using thermal IR imaging.** The investigation of the issues in the measurement set-up identifies two reliable temperature acquisition techniques to repeat the unsuccessful vacuum measurements. The first option is to apply the thermocouples with thermally-conductive epoxy adhesive and the second is to use thermal IR imaging.

   The application of COTS thermal IR cameras for vacuum testing requires additional design efforts because outgassing of volatile materials inside the camera can jeopardize its functionality. Options to use an IR camera in vacuum are the design of a hermetically sealed enclosure with an IR-transparent window or viewport from outside the vacuum enclosure by integrating such a window into the chamber walls.

2. **Increase the accuracy of the vacuum heating diagrams by extending the analysis to other hotspot components.** This study uses resistors to describe the vacuum heating of thermal hotspots. The use of passive resistors facilitates the study of various power inputs for the hotspot creation. The resistors provide a worst-case scenario considering the component size and conductive link to the mounting location. However, it is desirable to improve the accuracy of the thermal screening method by extending the analysis to other components, such as semiconductor and IC components.

3. **Validate the thermal screening method through thermal-vacuum testing of engineering or flight models of actual PocketQube subsystems.** This study uses test PCBs to represent thermal hotspot behavior of PocketQube subsystem boards. Thermal-vacuum testing of PocketQube subsystems enables to determine the performance of the thermal screening method and verify that the method provides a worst-case temperature estimation.

4. **Update the statistical analysis for the thermal model uncertainty margin by including flight data from PocketQubes.** The derivation of a thermal model uncertainty margin uses flight data from CubeSat missions. The upcoming launches of future PocketQubes, such as the Delfi-PQ and Unicorn-1, offer the opportunity to extend the analysis.

10.2 THERMAL-VACUUM TESTING FOR POCKETQUBES

This thesis investigates the impact of residual natural convection phenomena for thermal-vacuum testing of PocketQube subsystems. The numerical analysis shows that the temperature error remains low, which means that thermal-vacuum requirements can be moderated.

1. **Validate the hypothesis that thermal-vacuum testing at moderate pressure levels results in small temperature errors by repeating the vacuum testing in a test chamber of higher vacuum quality, e.g., at a pressure of $10^{-3}Pa$.** The two-point validation of the numerical simulation model shows a misalignment between simulation and experiment at low-pressure. The unsuccessful validation provides that final validation of the hypothesis is missing. The simplest way to determine the temperature error and prove the hypothesis is to repeat the vacuum measurements in a test facility of higher vacuum quality.

2. **Investigate the natural convection phenomena in the interior of an assembled PocketQube.** This study focuses on the effects of natural convection on PocketQube subsystems that are hanging in the center of a large enclosure. The common stacking assembly for PocketQubes arranges the subsystem boards one on top of the other. The compartmentalization reduces natural convection phenomena compared to the isolated, hanging configuration. Further investigation is necessary to describe the temperature error due to residual gas inside an assembled satellite. Quantification of the error or proof that it is acceptably low enables to moderate pressure requirements for system-level thermal-vacuum testing of PocketQubes.

3. **Determine the necessary pressure and temperature levels to trigger outgassing for PocketQube components.** Vacuum testing of spacecraft hardware is relevant beyond thermal reasons. The exposure of hardware to low-pressure conditions triggers the outgassing of volatile material. The outgassing can result in material damage or contamination of sensitive equipment. An investigation of the necessary pressure and temperature level for outgassing could lead to a moderation in the pressure requirements.

BIBLIOGRAPHY

Adafruit.com (2010). Arduino – ArduinoBoardUno (EAGLE files and schematic posted). Retrieved from `https://blog.adafruit.com/2010/09/27/arduino-arduinoboarduno-eagle-files-and-schematic-posted/`.

Aksöz, N., Öztürk, E., Bayram, , Aksöz, S., Kervan, S., Ülgen, A., and Maraşli, N. (2013). Thermal conductivity variation with temperature for Lead-Free ternary eutectic solders. *Journal of Electronic Materials*, 42(12):3573–3581.

Atmel (2012). Datasheet - ATmega16U2. Technical report, Atmel Corporation, San Jose, CA, USA.

Avila de Luis, R. (2018). *Standardized Thermal Control Solutions for PocketQubes*. Master's thesis, Delft University of Technology.

Bagavathiappan, S., Lahiri, B. B., Saravanan, T., Philip, J., and Jayakumar, T. (2013). Infrared thermography for condition monitoring - A review. *Infrared Physics and Technology*, 60:35–55.

Baturkin, V. (2005). Micro-satellites thermal control—concepts and components. *Acta Astronautica*, 56(1):161–170.

Bejan, A. (2013). *Convection Heat Transfer*. John Wiley & Sons, Ltd, New York, 4th edition.

Bentley, R. E. (1998). *The Theory and Practice of Thermoelectric Thermometry*. Springer-Verlag Berlin Heidelberg, Heidelberg, Germany, 3 edition.

Boerci, M. (2016). Delfi-PQ Systems Specification Document. Technical report, Delft University of Technology.

Bouwmeester, J., Gill, E., Speretta, S., and Uludag, S. (2017). New Approach on the Physical Architecture of CubeSats & PocketQubes. In *Proceedings of the 15th Reinventing Space Conference*, Glasgow, Scotland. [BIS-RS-2017-45] British Interplanetary Society.

Bouwmeester, J. and Guo, J. (2010). Survey of worldwide pico- and nanosatellite missions, distributions and subsystem technology. *Acta Astronautica*, 67(7-8):854–862.

Bouwmeester, J., Radu, S., Uludag, M., Chronas, N., Speretta, S., Menicucci, A., and Gill, E. K. A. (2018). Conditions and Application Domains for PocketQubes. In *The 4S Symposium*, Sorrento, Italy.

Breitenstein, O., Warta, W., and Langenkamp, M. (2010). *Lock-in Thermography*. Springer-Verlag Berlin Heidelberg, Berlin, Germany, 2 edition.

Brieß, K., Baumgartl, R., Henjes, C., Hülsenbusch, U., Grillenbeck, A., Kügler, H., Ley, W., Schneider, A., Scholz, A., Kayal, H., Bärwald, W., and Kuhlen, H. (2009). Spacecraft Design Process. In *Handbook of Space Technology*, pages 646–737. John Wiley & Sons, Ltd, New York, USA.

Busch, S., Bangert, P., Dombrovski, S., and Schilling, K. (2015). UWE-3, in-orbit performance and lessons learned of a modular and flexible satellite bus for future pico-satellite formations. *Acta Astronautica*, 117:73–89.

Carlomagno, G. M. and Cardone, G. (2010). Infrared thermography for convective heat transfer measurements. *Experiments in Fluids*, 49(6):1187–1218.

Deepak, R. A. and Twiggs, R. J. (2011). Thinking Outside the Box : Space Science Beyond the CubeSat. *Journal of Small Satellites*, 1(1):3–7.

DelfiSpace (2016). Testing for mechanical and electrical interfaces for delfi-pq. [Twitter post] Retrieved from `https://twitter.com/DelfiSpace`.

Diaz-Aguado, M. F., Ghassemieh, S., VanOutryve, C., Beasley, C., and Schooley, A. (2009). Small class-D spacecraft thermal design, test and analysis - PharmaSat biological experiment. In *IEEE Aerospace Conference Proceedings*, Big Sky, MT, USA. IEEE.

Dijstra Vereenigde (2018). Draaischuifpompen. Retrieved from `https://www.vacuubrandpompen.nl/draaischuifpompen?dir=asc&order=price`.

Döring, D., Hein, P. J., and Spiessberger, C. (2016). Temperature measurements in thermal-vacuum tests for spacecraft qualification – possibilities for infrared thermography. In *Quantitative InfraRed Thermography Conference*, pages 217–225, Gdansk, Poland.

DSPE (2018). Contact sensors. Dutch Society for Precision Engineering, Retrieved from `http://www.dspe.nl/knowledge-base/thermomechanics/chapter-5---measurement/5-2-contact-sensors/`.

Dubos, G. F., Castet, J.-F., and Saleh, J. H. (2010). Statistical reliability analysis of satellites by mass category: Does spacecraft size matter? *Acta Astronautica*, 67(5):584–595.

ECSS (2004). ECSS-Q-70-71A - Space Product Assurance - Data for selection of space materials and processes. Technical report, European Cooperation for Space Standardization, Noordwijk, Netherlands.

ECSS (2011). ECSS-E-HB-31-01 Part 1A - Thermal design handbook - Part 1: View factors. Technical report, European Cooperation for Space Standardization, Noordwijk, Netherlands.

ECSS (2016). Space engineering - Thermal analysis handbook. Technical report, European Cooperation for Space Standardization, Noordwijk, Netherlands.

Edwards, D. and Nguyen, H. (2016). Semiconductor and IC Package Thermal Metrics. Technical report, Texas Instruments Inc., Dallas, TX., USA.

Fishburne, R. (2000). IR thermography for electronic assembly design verification. Technical report, FLIR Systems, Wilsonville, OR, USA.

FLIR (2015). Use low-cost materials to increase target emissivity. Retrieved from `http://flir.co.uk/science/blog/details/?ID=71556`.

FLIR (2018). User's manual FLIR Ax5 series. Technical report, FLIR Systems, Wilsonville, OR, USA.

Foster, W. M. (1992). Thermal verification testing of commercial printed-circuit boards for spaceflight. In *Reliability and Maintainability Symposium, 1992. Proceedings., Annual*, pages 189–195. IEEE.

Gerhardt, D., Palo, S. E., Schiller, Q., Blum, L., Li, X., and Kohnert, R. (2013). The Colorado Student Space Weather Experiment (CSSWE) On-Orbit Performance. *Journal of Small Satellites*, 3(1):265–281.

Gilmore, D. G. (2002). *Spacecraft thermal control handbook: Volume I*. Aerospace Press, El Segundo, Calif., USA, 2nd edition.

Gluck, D. F. and Baturkin, V. (2002). Mountings and Interfaces. In Gilmore, D. G., editor, *Spacecraft Thermal Control Handbook*, chapter 8. Aerospace Press, El Segundo, Calif., USA, 2nd edition.

Graebner, J. E. and Azar, K. (1997). Thermal Conductivity Measurements in Printed Wiring Boards. *Journal of Heat Transfer*, 119(3):401–405.

Graziosi, M. (2008). *Delfi-C3 Thermal Control Subsystem: Design, Assembly, Integration and Verification*. Master's thesis, Delft University of Technology.

Gryzagoridis, J. (1971). Natural convection from a vertical flat plate in the low grashof number range. *International Journal of Heat and Mass Transfer*, 14(1):162–165.

Guo, J., Bouwmeester, J., and Gill, E. (2016). In-orbit results of Delfi-n3Xt: Lessons learned and move forward. *Acta Astronautica*, 121:39–50.

Guo, J., Monas, L., and Gill, E. (2014). Statistical analysis and modelling of small satellite reliability. *Acta Astronautica*, 98:97–110.

Gurrum, S. P., Romig, M. D., Horton, S. J., and Edwards, D. R. (2011). A quick PCB thermal calculator to aid system design of exposed pad packages. In *2011 27th Annual IEEE Semiconductor Thermal Measurement and Management Symposium*, pages 63–69.

Han, Z. and Fina, A. (2011). Thermal conductivity of carbon nanotubes and their polymer nanocomposites: A review. *Progress in Polymer Science (Oxford)*, 36(7):914–944.

Hosseini, R. and Saidi, M. (2012). Experimental study of air pressure effects on natural convection from a horizontal cylinder. *Heat Transfer Engineering*, 33(10):878–884.

Hosseini, R., Taherian, H., and Campo, A. (2010). Measurements of natural convection and surface radiation from a heated vertical plate immersed in quiescent air at sub-atmospheric pressures. *Experimental Heat Transfer*, 23(2):117–129.

Jeon, H., Yoon, C., Song, Y.-G., Han, J., Kwon, S., Kim, S., Chang, I., and Lee, K. (2018). Reducing the Coefficient of Thermal Expansion of Polyimide Films in Microelectronics Processing Using ZnS Particles at Low Concentrations. *ACS Applied Nano Materials*, 1:1076–1082.

Jones, N. (2014). Space: Mini satellites prove their scientific power. *Nature*, 508(7496):300–301.

Jousten, K. (2016). *Handbook of Vacuum Technology*. John Wiley & Sons, Ltd, New York, USA, 2nd edition.

Kang, S. J. and Oh, H. U. (2016). On-orbit thermal design and validation of 1 U standardized CubeSat of STEP cube lab. *International Journal of Aerospace Engineering*, 2016.

Kasemsadeh, B. and Heng, A. (2017). SNOA967: Temperature Sensors: PCB Guidelines For Surface Mount Devices. Technical report, Texas Instruments Inc., Dallas, TX., USA.

Kinzie, P. A. and Rubin, L. G. (1973). Thermocouple temperature measurement. *Physics Today*, 26:52.

Kovács, R. and Józsa, V. (2018). Thermal analysis of the SMOG-1 PocketQube satellite. *Applied Thermal Engineering*, 139:506–513.

Langebach, J., Senin, S., and Karcher, C. (2007). Experimental study of convection and radiation interaction in a headlight model using pressure variation. *Experimental Thermal and Fluid Science*, 32(2):521–528.

Langer, M. and Bouwmeester, J. (2016). Reliability of CubeSats – Statistical Data, Developers' Beliefs and the Way Forward. In *30th Annual AIAA/USU Conference on Small Satellites*, pages SSC16–X–2, Logan, USA. AIAA/USU.

Lau, J. H., Rice, D. W., and Avery, P. A. (1987). Elastoplastic Analysis of Surface-Mount Solder Joints. *IEEE Transactions on Components, Hybrids, and Manufacturing Technology*, 10(3):346–357.

Lohan, J., Tiilikka, P., Rodgers, P., Fager, C. M., and Rantala, J. (2000). Experimental and numerical investigation into the influence of printed circuit board construction on component operating temperature in natural convection. *IEEE Transactions on Components and Packaging Technologies*, 23(3):578–586.

Macco, C. (2014). *Design and Verification of the Delfi-n3Xt Thermal Control Subsystem*. Master's thesis, Delft University of Technology.

Martynenko, O. G. and Khramtsov, P. P. (2005). *Free-Convective Heat Transfer*. Springer-Verlag Berlin Heidelberg, Heidelberg, Germany.

Mason, J. P., Lamprecht, B., Woods, T. N., and Downs, C. (2017). CubeSat On-Orbit Temperature Comparison to Thermal-Balance-Tuned-Model Predictions. *Journal of Thermodynamics and Heat Transfer*, 32(1):237–255.

Meola, C. and Carlomagno, G. M. (2004). Recent advances in the use of infrared thermography. *Measurement Science and Technology*, 15(9):R27.

Morgan, V. T. (1975). The overall convective heat transfer from smooth circular cylinders. *Advances in heat transfer*, 11:199–264.

Mortan, F. and Wright, L. (2004). Quad Flatpack No-Lead Logic Packages. Technical report, Texas Instruments Inc., Dallas, TX., USA.

National Instruments (2015). NI 9211 Datasheet. Technical report, Texas Instruments.

National Physics Laboratory (2010). What do 'high vacuum' and 'low vacuum' mean? (FAQ - Pressure) : FAQs : Reference : National Physical Laboratory. Retrieved from `http://www.npl.co.uk/reference/faqs/what-do-high-vacuum-and-low-vacuum-mean-(faq-pressure)`.

Omega Engineering (2005). Physical Properties of Thermoelement Materials. Technical report, OMEGA Engineering, Norwalk, CT, USA.

Orlove, G. (2011). ITC TECHNICAL PUBLICATION 54 - Two Dimensional Spatial Emissivity Correction Technique. Technical report, FLIR Systems, Wilsonville, OR, USA.

Radu, S., Uludag, M., Speretta, S., Bouwmeester, J., Menicucci, A., Cervone, A., Dunn, A., Walkinshaw, T., Kaled Da Cas, P., Cappelleti, C., and Graziani, F. (2018). PocketQube Mechanical Interface Standard. Technical report, DataverseNL.

RFMD (2018). RFPA0133 - 3 TO 5 V PROGRAMMABLE GAIN HIGH EFFICIENCY POWER AMPLIFIER. Technical report, RF Micro Devices, Greensboro, NC, USA.

Robinson, D. W., Simpson, R., Parian, J. A., Cozzani, A., Casarosa, G., Sablerolle, S., and Ertel, H. (2017). 3D thermography for improving temperature measurements in thermal vacuum testing. *CEAS Space Journal*, 9(3):333–350.

Saidi, M. and Abardeh, R. H. (2010). Air Pressure Dependence of Natural-Convection Heat Transfer. In *Proceedings of the world congress on engineering*, volume 2, pages 1–5, Londin, UK. WCE 2010.

Sattel, S. (2018). Getting Your Layer Stack Right the First Time. Retrieved from `https://www.autodesk.com/products/eagle/blog/getting-layer-stack-right-first-time/`.

Saunders, O. A. (1936). The Effect of Pressure Upon Natural Convection in Air. *Proceedings of the Royal Society of London. Series A, Mathematical and Physical Sciences*, 157(891):278–291.

Schlichting, H. and Gersten, K. (2016). *Boundary-layer theory*. Springer-Verlag Berlin Heidelberg, Heidelberg, Germany, 9 edition.

Shaukatullah, H. and Claassen, A. (2003). Effect of thermocouple wire size and attachment method on measurement of thermal characteristics of electronic packages. *Ninteenth Annual IEEE Semiconductor Thermal Measurement and Management Symposium, 2003.*, pages 97–105.

Sidles, P. H. and Danielson, G. C. (1951). Thermal conductivity of metals at high temperatures. Technical report, Atomic Engergy Commission United States of America, Oak Ridge, TN, USA.

Song, G., Wang, D., Dang, G., Zhou, H., Chen, C., and Zhao, X. (2014). Thermal expansion behavior of polyimide films containing benzoxazole unit. *High Performance Polymers*, 26(4):413–419.

Speretta, S., Gill, E. K. A., Guo, J., Pérez Soriano, T., Bouwmeester, J., Carvajal Godínez, J., Watts, T. G., Menicucci, A., and Sundaramoorthy, P. P. (2016). Cubesats to pocketqubes: Opportunities and challenges. In *Proceedings of the 67th International Astronautical Congress*, Guadalajara, Mexico. IAF.

Stout, R. (2009). Thermal Considerations for a 4x4 mm QFN. Technical report, ON Semiconductor, Phoenix, AZ, USA.

Suhling, J. C., Johnson, R. W., White, J. D., Matthai, K. W., Knight, R. W., Romanczuk, C. S., and Burcham, S. W. (1994). Solder joint reliability of surface mount chip resistors/capacitors on insulated metal substrates. *Proceedings of the 1994 IEEE 44th Electronic Components & Technology Conference*, pages 465–473.

Svasta, P., Simion-Zanescu, D., and Ionescu, R. (2004). Components' emissivity in reflow soldering process. In *Electronic Components and Technology Conference, 2004. Proceedings. 54th*, volume 2, pages 1921–1924, Las Vegas, NV, USA. IEEE.

Swartwout, M. (2016). Secondary spacecraft in 2016: Why some succeed (And too many do not). In *IEEE Aerospace Conference Proceedings*, Big Sky, MT, USA. IEEE.

Texas Instruments (2013). AN-2020 Thermal Design By Insight, Not Hindsight. Technical report, Texas Instruments Inc., Dallas, TX., USA.

Texas Instruments (2015). MSP432P401R, MSP432P401M. Technical report, Texas Instruments Inc., Dallas, TX., USA.

Theodore, L. (2011). *Heat transfer applications for the practicing engineer*. John Wiley & Sons, Ltd, New York, USA, 7 edition.

Van Boxtel, T. a. (2015). *Thermal modelling and design of the DelFFi satellites*. Master's thesis, Delft University of Technology.

VDI (2010). *VDI Heat Atlas*. VDI-buch; VDI-Buch. Springer-Verlag Berlin Heidelberg, Heidelberg, Germany, 2nd edition.

Vellvehi, M., Perpiñà, X., Lauro, G. L., Perillo, F., and Jordà, X. (2011). Irradiance-based emissivity correction in infrared thermography for electronic applications. *Review of Scientific Instruments*, 82(11).

Venturini, C., Braun, B., Hinkley, D., and Berg, G. (2018). Improving Mission Success of CubeSats. Technical report, The Aerospace Corporation, El Segundo, Calif., USA.

Vishay (2010). Power Dissipation Considerations in High Precision Vishay Sfernice Thin Film Chips Resistors and Arrays. Technical report, Vishay Intertechnology, Inc., Malvern, PA, USA.

Vollmer, M. and Möllmann, K.-P. (2010). *Infrared Thermal Imaging: Fundamentals, Research and Applications*. Wiley-VCH.

Welch, J. W. (2002). Thermal Testing. In Gilmore, D. G., editor, *Spacecraft Thermal Control Handbook*, chapter 19, pages 709–757. Aerospace Press, El Segundo, Calif., USA, 2nd edition.

Welch, J. W. (2016). Assessment of Thermal Balance Test Criteria Requirements on Test Objectives and Thermal Design. In *46th International Conference on Environmental Systems*, Vienna, Austria. ICES.

Woellert, K., Ehrenfreund, P., Ricco, A. J., and Hertzfeld, H. (2011). Cubesats: Cost-effective science and technology platforms for emerging and developing nations. *Advances in Space Research*, 47(4):663–684.

Zandman, F. and Szwarc, J. (2008). Non-Linearity of Resistance/Temperature Characteristic: Its Influence on Performance of Precision Resistors. Technical report, VISHAY INTERTECHNOLOGY, INC.

A NATURAL CONVECTION EXPERIMENT

CONDUCTIVE HEAT LOSS THROUGH POWER SUPPLY CABLING

The graph in figure 79a illustrates the experimental measurements for the conductive heat loss through the cable. The measurement data of the test item and the power supply cable yield the following heat loss through the cable, see figure 79b. The temperature values of cable are measured at a distance of $23mm$ from the test item. The computation of the conductive heat loss considers an AWG26 aluminum cable with a thermal conductivity of $\lambda = 260W/mK$ (Gilmore, 2002).

$$\dot{Q}_{loss} = \frac{\lambda A_{AWG26}}{l} \left(T_{TC} - T_{cable} \right) \tag{38}$$

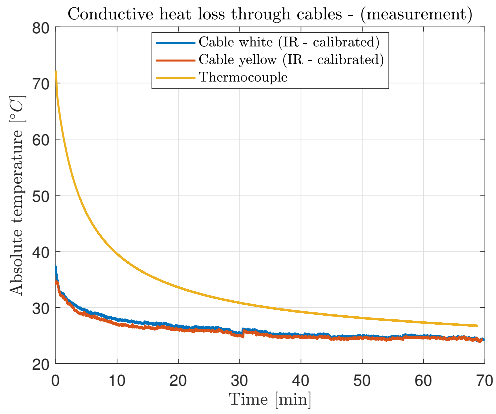

(a)

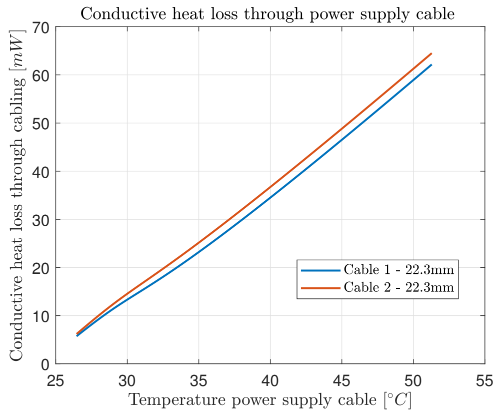

(b)

Figure 79: Conductive heat loss through the power supply cables of the convection test item. (a) Temperature measurement plots and (b) heat loss as a function of the cable temperature.

BIOT NUMBER

The Biot Bi number is a dimensionless parameter that indicates whether it is appropriate to assume isothermal surface properties for a test body, i.e. apply a single thermal node to the object. The Bi number compares the internal heat transfer due to conduction to the heat exchange with the environment due to radiation and convection. It is appropriate to assume isothermal surface condition when the conduction inside an object is significantly larger than the heat exchange with the environment, i.e. corresponding to a low Bi number. The highest Bi numbers occur at highest temperature since the radiative and convective heat transfer scale with temperature, while the conductive heat transfer is assumed independent of temperature for the temperature ranges of interest to this study.

The analysis in chapter considers a PocketQube subsystem as a single thermal node. The following calculation shows that this assumption is appropriate reasoning from the Bi number. Since the Bi number is highest for the largest temperature, a test object temperature of $100°C$

and test facility temperature of $25°C$ is assumed. The following relation describes the equivalent thermal conductivity of a multi-layer PCB as a function of $Z = n\frac{t_{Cu}}{t_{PCB}}$ with t denoting the thickness and n the number of continuous copper planes according to the empirical relation described by Graebner and Azar (1997).

$$\lambda_{\parallel} = 385 * Z + 0.87 \tag{39}$$

$$\lambda_{\perp} = (3.23\,(1 - Z) + 0.0026Z)^{-1} \tag{40}$$

The characteristic length l^* is assumed as the surface area over the perimeter. These inputs yield a Bi number significantly lower than unity. The low value in the Bi number shows that the single-node assumption is appropriate in first order.

$$Bi = \frac{h_{rad} + h_{conv}}{\lambda_{PCB,4-layer}/l^*} = \frac{6.8 + 9.6}{34.6/0.01} = 0.0047 << 1 \tag{41}$$

B | TEST RESULTS

B.1 EXPERIMENTAL MEASUREMENT PLOTS

Case I

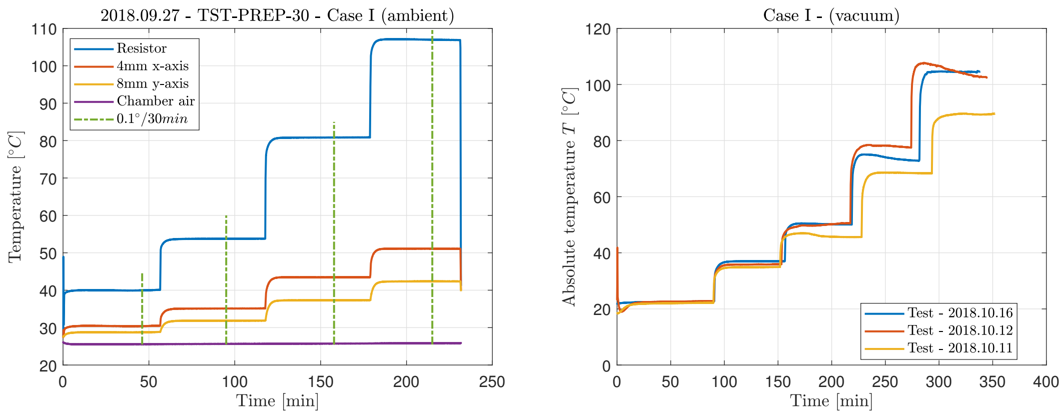

(a) (b)

Figure 80: Thermocouple measurement plot case I test board (a) Ambient measurement. (b) Overview of vacuum measurements.

Case II

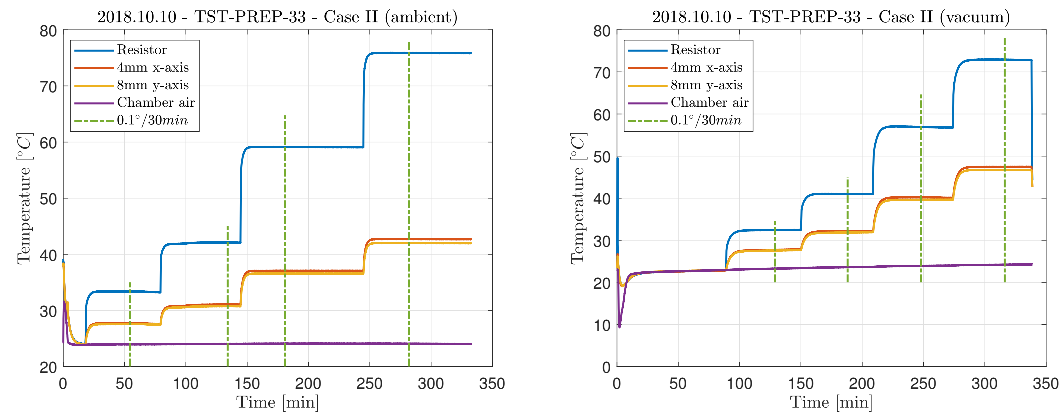

(a) (b)

Figure 81: Thermocouple measurement plot case II test board (a) Ambient and (b) vacuum measurement.

Case II (oven)

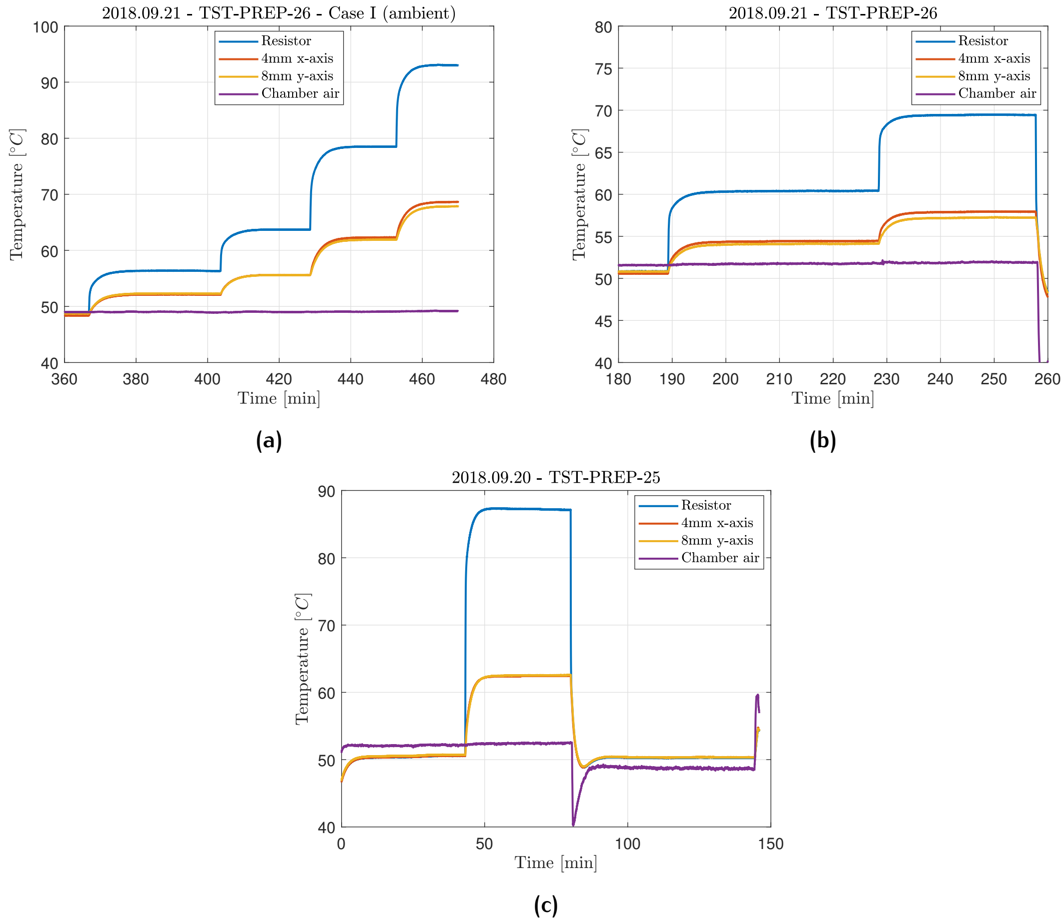

Figure 82: Thermocouple measurement plot case II (50°C) test board (a) Ambient and (b), (c) vacuum measurement. The single vacuum measurement points was taken after the detachment of the thermocouples, see figure 65a, using a different polyimide foil.

Case VI

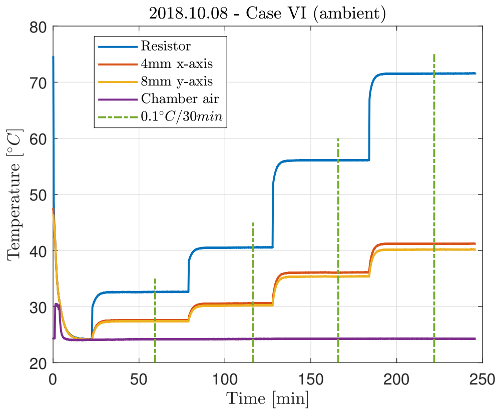

(a)

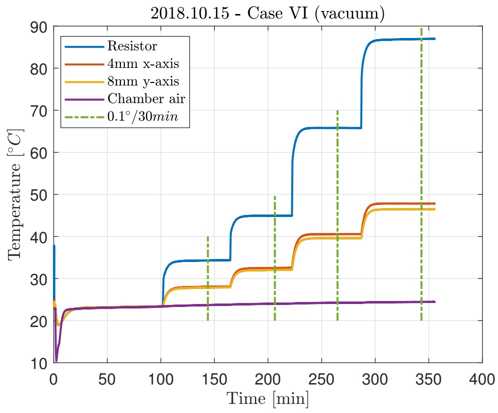

(b)

Figure 83: Thermocouple measurement plot case VI test board (a) Ambient and (b) vacuum measurement.

Case VIII

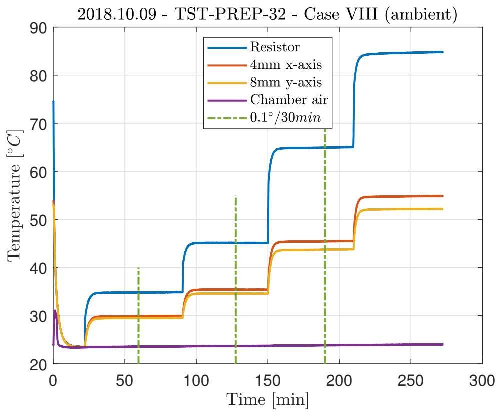

(a)

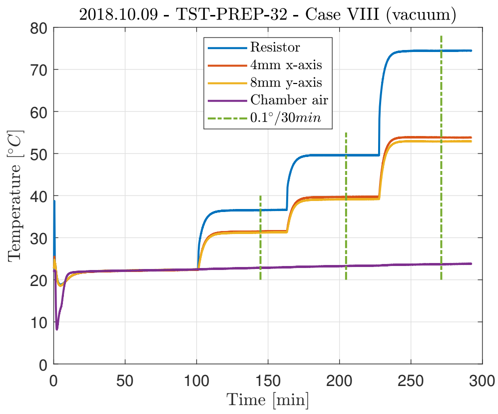

(b)

Figure 84: Thermocouple measurement plot case VIII test board (a) Ambient and (b) vacuum measurement. The measurement of the $750mW$ measurement point was omitted due to time constraints that day.

B.2 IR TEMPERATURE MAPS OF THE TEST BOARDS

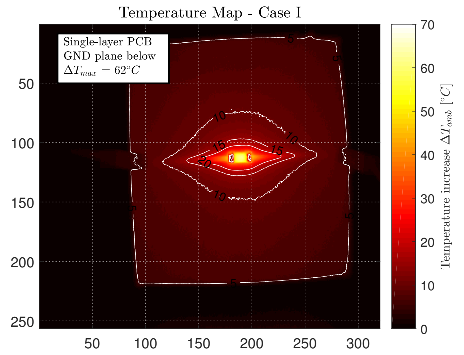

(a)

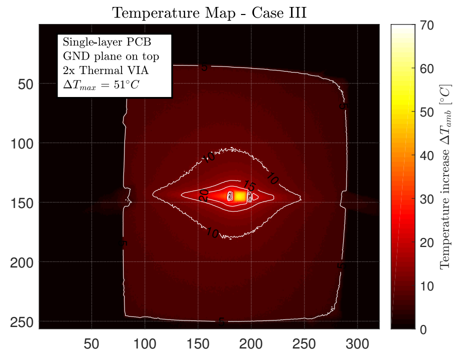

(b)

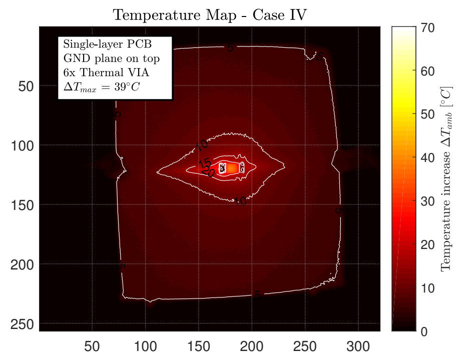

(c)

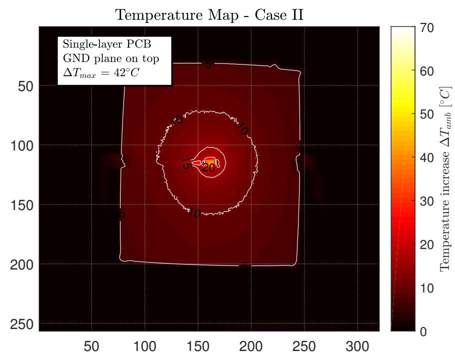

(d)

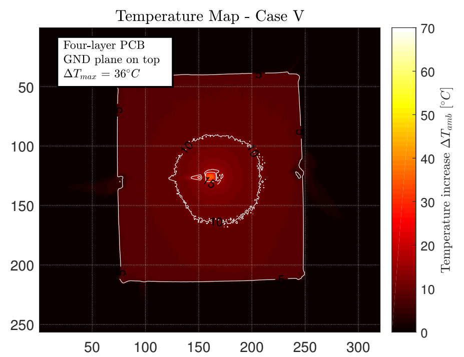

(e)

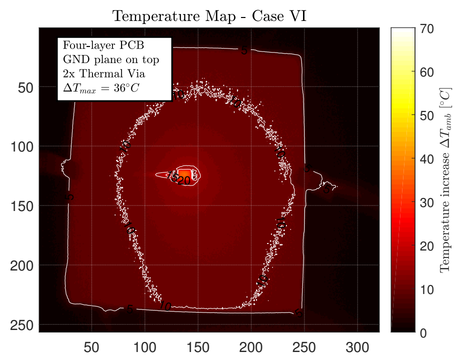

(f)

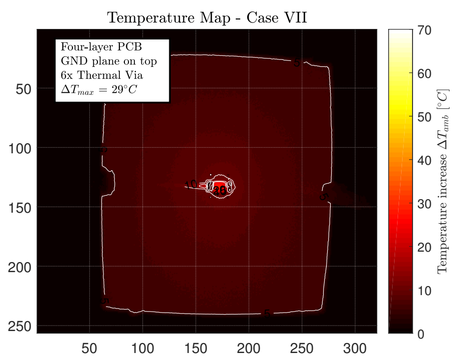

(g)

Figure 85: IR temperature maps resulting from a power input of 0.5W. Case I (a) to VII (g).

B.3 VALIDATION OF THE ESATAN THERMAL SIMULATION

Ambient pressure measurement

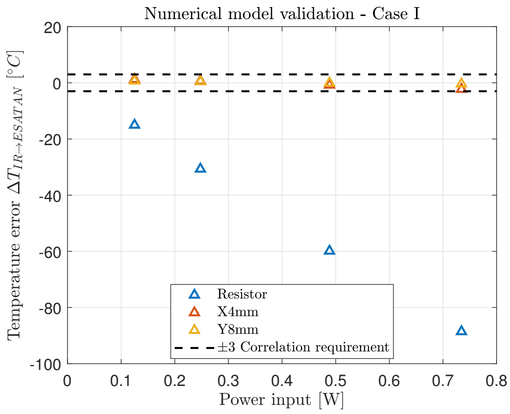

(a)

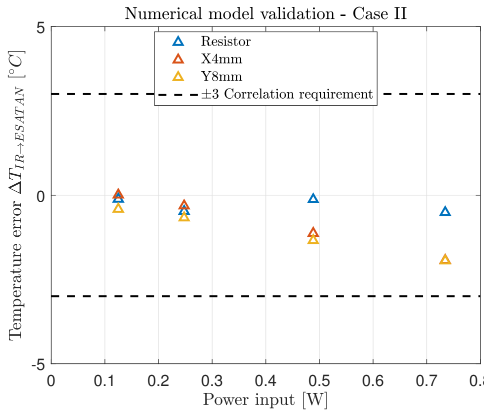

(b)

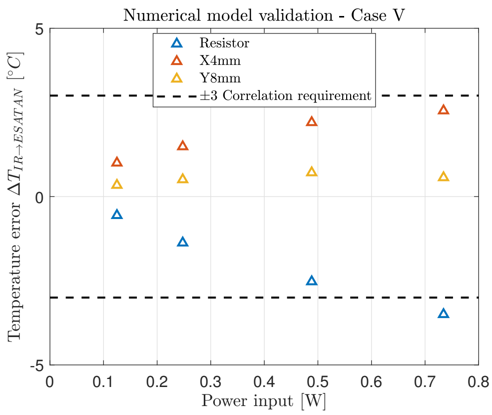

(c)

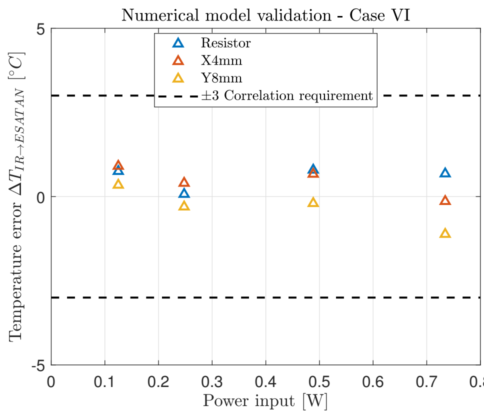

(d)

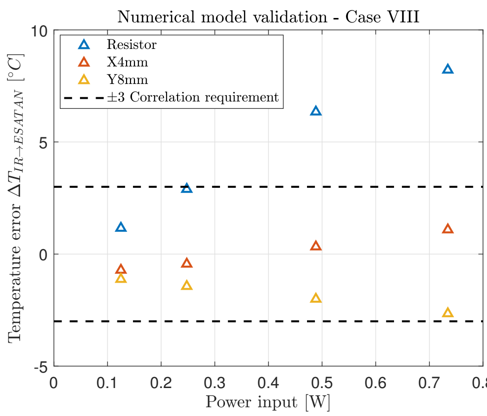

(e)

Figure 86: Comparison between IR measurements and numerical prediction at ambient pressure conditions. The legend in the graphs refers to the measurement locations in figure 60. (a) Case I. (b) Case II. (c) Case V. (d) Case VI. (e) Case VIII

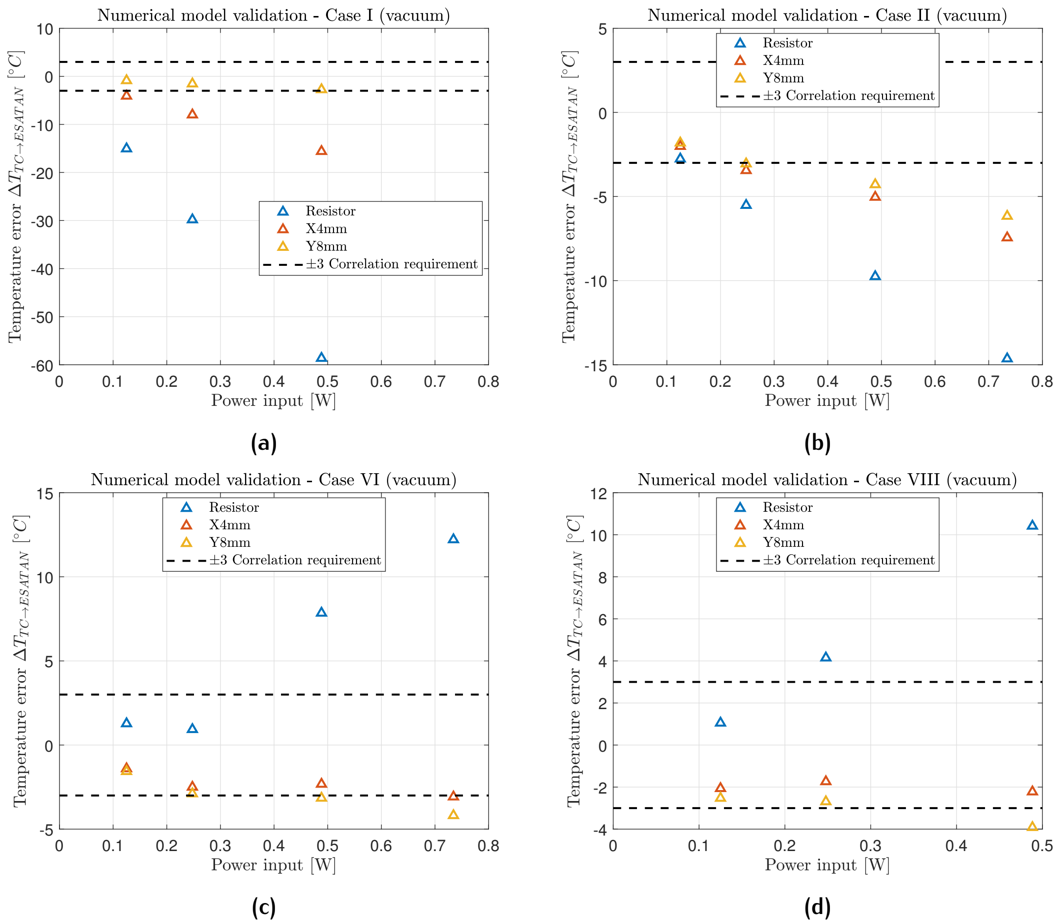

Figure 87: Comparison between thermocouple measurements and numerical prediction at vacuum pressure conditions. The legend in the graphs refers to the measurement locations in figure 60. (a) Case I. (b) Case II. (c) Case VI. (d) Case VIII.

C CONFERENCE PAPER

12TH IAA SYMPOSIUM ON SMALL SATELLITES FOR EARTH OBSERVATION, BERLIN, GERMANY

Draft conference paper (Abstract accepted, December 2018)

Effective thermal testing and design solutions for PocketQube subsystems

TimoRühl[1a], Jasper Bouwmeester[1b]

[1]Faculty of Aerospace Engineering, Delft University of Technology
Kluyverweg 1, 2629HS Delft, Netherlands
Mail: (a) timo.ruehl@community.isunet.edu (b) jasper.bouwmeester@tudelft.nl

Abstract: The PocketQube is promising to be the next step in the miniaturization of space technology. The ambitious goals of achieving rapid design-to-orbit cycles while maintaining the lowering the cost of accessing space requires cost- and time-effective test strategies. This research proposes and implements a thermal screening method for PocketQube subsystems to identify temperature-critical hotspots and verify their compliance against operational hardware limits. Key elements of the test method are a thermal IR scan at ambient conditions and an estimation of the worst-case flight temperature using experimentally derived graphs that describe the vacuum heating of thermal hotspots. Moreover, the study proposes to lower the required pressure levels for thermal-vacuum testing of PocketQube subsystems. Numerical analysis shows that, due to the small form factor of PocketQubes, pressure levels by three orders of magnitude larger than those used in environmental test standards for larger satellites suffice to maintain the resulting error acceptably low for the thermal balance testing. Both the screening method and moderation in vacuum requirements contribute to the development test methods requiring minimum effort concerning necessary equipment.

1. INTRODUCTION

The PocketQube is an emerging satellite class, which pushes the miniaturization of space technology beyond the well-established CubeSats [1]. A showstopper in the success story of nano- and picosatellites are their high mission failure rates [2]. Design flaws and workmanship errors are primary reasons for the low mission success rates [2], [3]. Pre-flight testing and verification are typically effective means to reveal design deficiencies and incorrect assemblies. Stringent cost and schedule restrictions, together with inefficiencies throughout the design process, often motivate nano- and picosatellite developers to postpone environmental testing towards the end of the design lifecycle, where recovering for design flaws is considerably inefficient [3], [4]. The project circumstance of nano- and picosatellite missions require, therefore, test strategies that facilitate early design evaluation requiring minimum effort concerning cost and necessary equipment.

This paper proposes a thermal screening method to support verification programs in the thermal domain during early development phases. The methodology provides a quick means to check compliance with the hot-side temperature requirements. The necessary steps to implement the test method enable, moreover, to investigate the necessary pressure levels for thermal-vacuum testing of PocketQube subsystems, which directly relate to cost of the necessary laboratory equipment.

2. TEST METHODS FOR POCKETQUBE SUBSYSTEMS

2.1 Thermal screening method for thermal hotspot identification

The introduction of the PocketQube poses new challenges to thermal engineering. The low mass of PocketQubes implies larger temperature swings oscillations [1] and on-going research indicates that PocketQubes reach steady-state conditions during the sunlit part of the orbit [5]. Moreover, the aspiration for miniaturization drives toward increasing the energy density per subsystem board. These challenges motivate to develop a test methodology to verify compliance of subsystems with the hot-side temperature requirements.

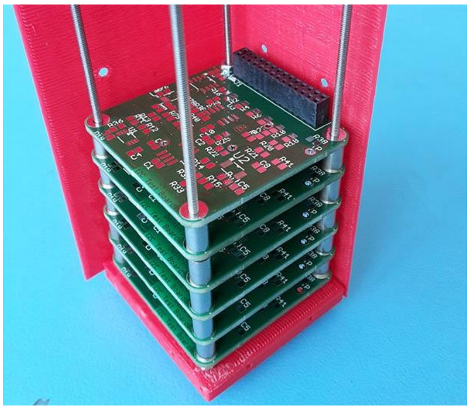

Figure 1 – Delfi-PQ subsystem assembly.

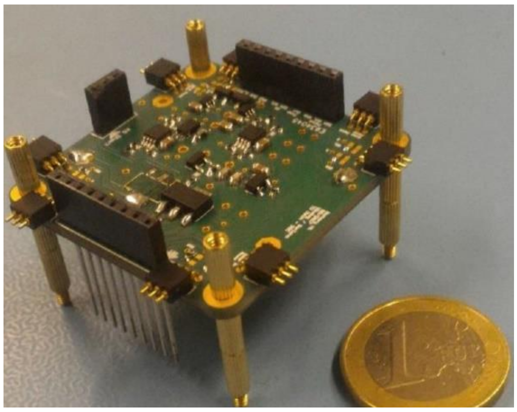

Figure 2 – PocketQube subsystem board.

The proposed test method leverages thermal IR imaging to identify thermal hotspots and measure their temperature increase. Diagrams describing the vacuum heating of thermal hotspots complement the ambient IR temperature screen. The combination of IR screen and heating diagrams enables to perform a judgment whether critical temperatures occur. Figure 3 outlines the thermal screening method, which includes the following steps:

1. An IR scan of a subsystem board in a laboratory environment yields a temperature map, which contains information on thermal hotspots and their temperature relative to the subsystem board.
2. A thermal simulation model of the entire satellite assembly estimates the maximum subsystem temperature during flight.
3. Experimentally derived graphs describe how much more hotspots heat up in vacuum due to the absence of natural convection cooling.
4. Thermal simulation models rely on parameter and modelling assumptions, which result in differences between predicted and flight temperatures. This paper defines an uncertainty margin to account for the model uncertainties.
5. The summation of all previous contributions yields an estimate of the maximum hotspot temperature during flight. Comparing the estimated temperature with the operational hardware limit shows whether a hotspot is critical concerning overheating. Further simulative analysis with a higher fidelity simulation model or redesign becomes necessary when the estimated temperature exceeds the limit.

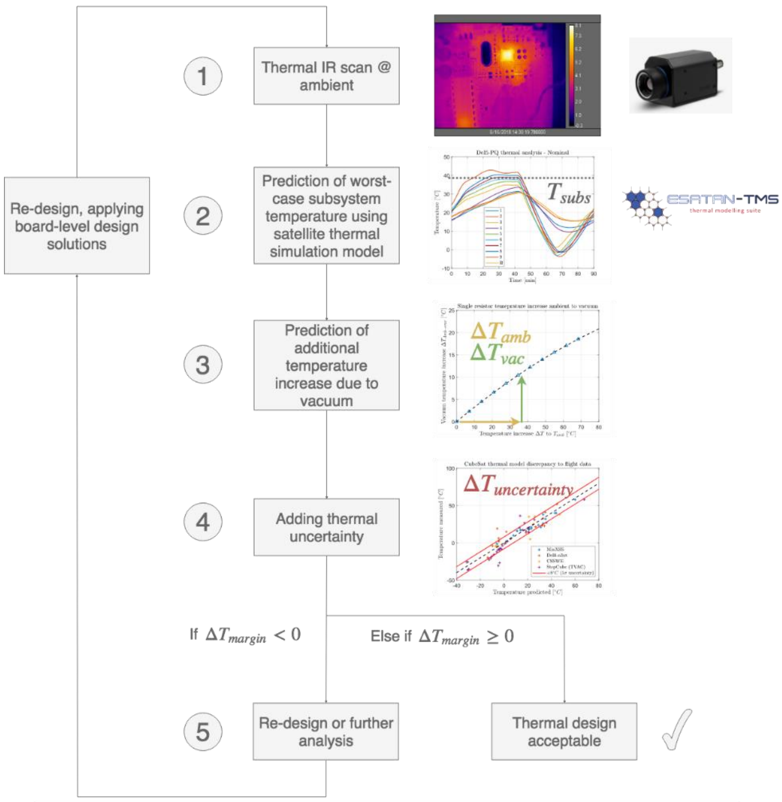

Figure 3 – Thermal screening methodology to assess thermal hotspots.

2.2 Pressure requirements for thermal vacuum testing

The derivation of graphs to describe the thermal behavior of thermal hotspots (step 3 - screening method) involves thermal-vacuum testing. The vacuum quality of a test facility determines its cost and the amount of residual gas in the test environment. Residual gases introduce inaccuracies concerning flight conditions. The residual gas creates additional heat paths through convection and gas conduction that introduce temperature errors compared to ideal vacuum conditions. Quantification of the temperature error allows choosing the necessary pressure levels for thermal-vacuum testing.

This paper uses thermal balance testing as a case study to define the acceptable temperature error due to residual gas effects. The objective of a balance test is to produce data for correlating unknown parameters of a thermal simulation model [6]. The temperature error due to inaccuracies in the facilities must be lower than the model uncertainty that the testing tries to improve. The thermal model uncertainty margin (step 4 in the screening method) provides a reference value establishing an acceptable temperature error.

3. TEST METHODOLOGY

3.1 Implementation of the thermal test methodology

The experimental part of this research focuses on characterizing the performance of a commercial-off-the-shelf thermal IR camera (step 1 – screening method) and describing the vacuum heating of thermal hotspots (step 3 – screening method).

The performance characterization uses the operation of an ArduinoUNO microcontroller as a case study. The microcontroller shows similarity in board layout and component size to the Delfi-PQ power amplifier, a critical hotspot component. Thermocouple measurements provide a reference to compare the performance of both techniques.

The analysis uses representative PocketQube subsystem boards with surface mount resistors as the hotspot component. Resistors are flexible towards manipulating the power dissipation. Moreover, the resistors provide a worst-case scenario because of their small size and conduction to the board. Larger semiconductor components show better heat sinking capabilities due to their size and mounting to the board. Figure 4 shows the test board layout, which enables to study the hotspot behavior concerning geometric size (single and double resistor) and board layout (mounted on FR4 or continuous copper ground plane).

Figure 4 – Electrical layout of the three test boards considered in this paper.

The experimental test set-up consists of a hanging test configuration using fluorocarbon mono-filament fibers and thermocouples taped with polyimide foil.

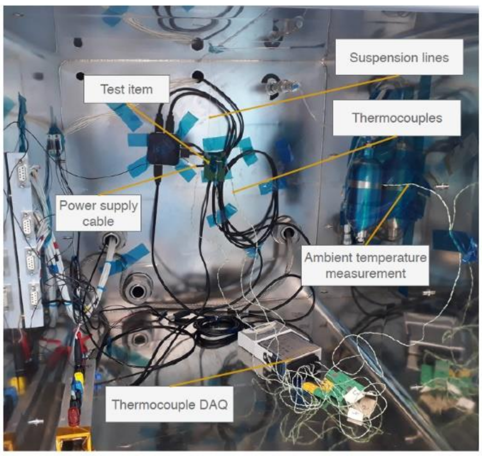

Figure 5 – Experimental test set-up vacuum measurements.

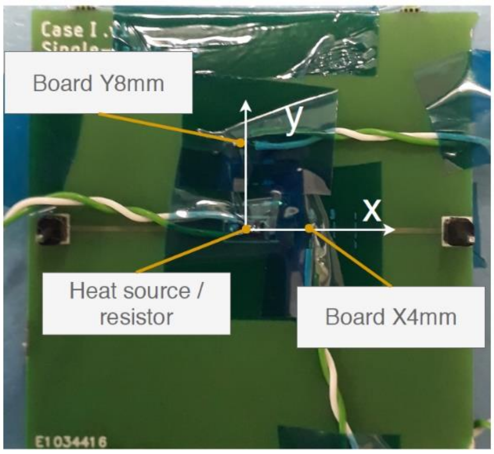

Figure 6 – Thermocouple measurement locations on the test board.

3.2 Natural convection at subatmospheric pressure

The pumping systems of the test facility in this study achieve ultimate pressures of 280 and $21 Pa$. A description of the natural convection coefficient enables to numerically determine the temperature penalty compared to testing in ideal vacuum ($0 Pa$).

The experimental test set-up consists of a rectangular copper test specimen with the footprint of a Delfi-PQ subsystem board. The test sequence consists of, first, heating the test item to a steady-state temperature and, then measuring the temperature during the cooling. The transient heat balance of the cooling process yields the natural convection heat transfer coefficient. The emissivity of the copper test item and conductive heat loss through the cabling are calibrated using a thermal IR camera.

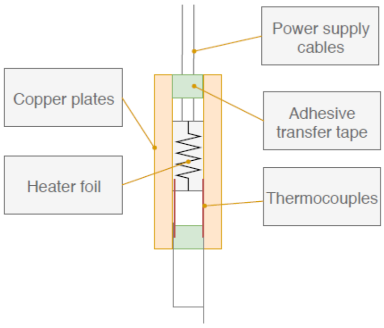

Figure 5 – Schematic test item configuration

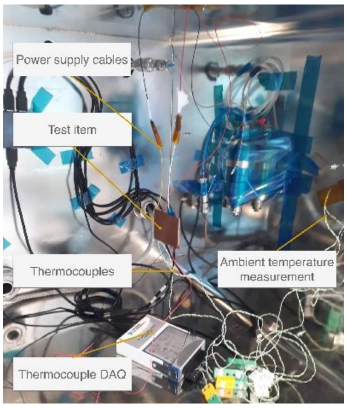

Figure 6 – Measurement set-up natural convection testing

4. RESULTS

4.1 Thermal screening method

The performance characterization shows thermal IR imaging achieves the same accuracy as thermocouples in measuring the relative temperature increase of the resistors and the Arduino microcontroller. The IR imaging requires calibration for the background radiation and emissivity of the body of interest. Digital image subtraction using a reference image of an inactive test board is a simple means to remove the background radiation. The dominant disturbance is the reflected IR radiation that the camera itself emits. Above 10K temperature increase, IR imaging of high-emissivity components requires for emissivity correction as described in [7], whereas low-emissivity components require the application of a correction fluid first to increase the target emissivity. The emissivity correction requires either reference values for the emissivity or a two-point emissivity calibration as described in [7].

Taped thermocouples prove unreliable in maintain sufficient contact pressure to measure resistor temperatures. The taped thermocouple measurements show a systematic error that scales in temperature, see error plot in Figure 9. The maximum observed error is used to determine an error correction graph, see Figure 10. The error graph enables to correct the taped vacuum measurement of the test board VIII, which serves as a reference case for the Delfi-PQ communication board concerning board layout and geometric size of the hotspot.

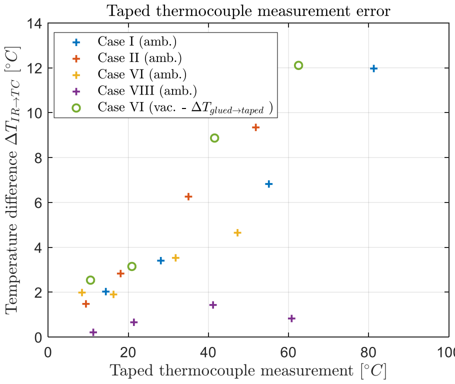

Figure 7 – Taped thermocouple measurement error

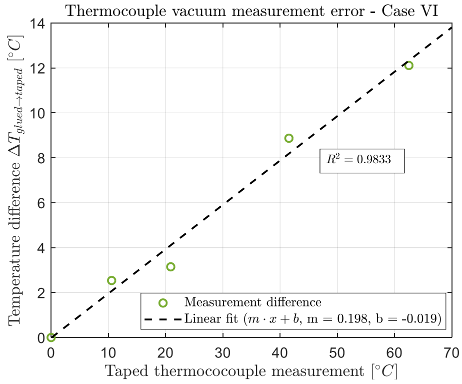

Figure 10 – Correction graph for the thermocouple measurement.

The diagram in Figure 8 describes the hotspot vacuum heating concerning geometric size and board layout. The test board VIII saves as a reference case to show the application of the thermal screening method. The test board VIII resembles the Delfi-PQ communication subsystem in board layout and hotspot size. Table 1 details the steps of the screening methodology to estimate the maximum hotspot temperature. The methodology shows that the maximum temperature remains below the $+85°C$ operational hardware limit.

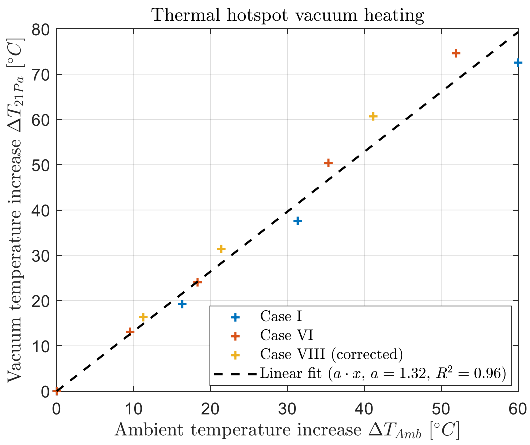

Figure 8 – Thermal hotspot heating characteristics.

Table 1 – Application of the thermal screening method to the Delfi-PQ communication subsystem.

Step	Description	Temp. [°C]
(1)	Max. subsystem temperature with satellite simulation model	42
(2)	Ambient temperature increase (0.5W - dissipation)	+21.4
(3)	Vacuum Temperature increase Thermocouple detachment error (Figure 10)	+4.8 +5.2
(4)	Thermal model uncertainty margin (see next section)	+8
(5)	Total temperature of the power amplifier	81.4

4.2 Thermal model uncertainty margin

The derivation of a thermal model uncertainty margin uses flight and test data of four CubeSat missions: Delfi-n3xt [10], MinXSS [11], CSSWE [12], StepCubeLab [13]. The distribution of the error between simulation and measurement yields a $\pm 8K$ standard deviation assuming a Gaussian distribution of the temperature error. The standard deviation implies a 68% (1σ) confidence that the actual flight data remain within the predicted boundaries. The higher risk acceptance of nano- and picosatellite missions justifies the lower confidence level compared to the 2σ margin used in environmental standards for traditional satellites [6].

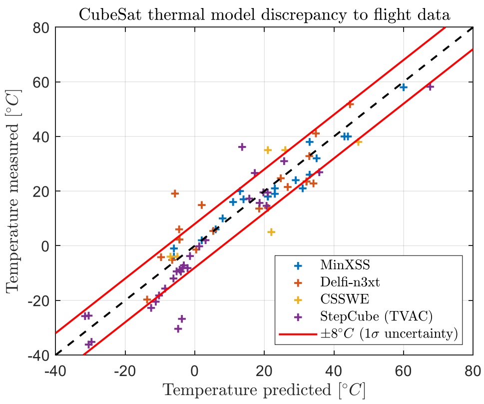

Figure 9 - Deviation between predicted and measured temperatures for CubeSats.

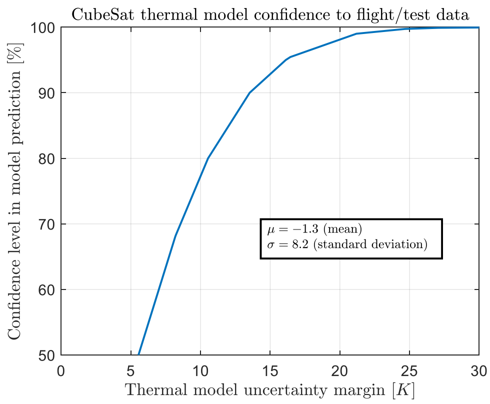

Figure 10 - Confidence level thermal model uncertainty margin.

4.3 Pressure requirements for thermal balance testing of PocketQubes

This paper uses thermal balance testing as a case study to discuss the acceptable temperature error due to residual gas in the test environment. The thermal model uncertainty margin provides a reference value for the parameter uncertainty that thermal balance testing tries to improve. Therefore, a threshold for the maximum temperature error due to inaccuracies in the test environment is $\pm 8K$. However, lower temperature errors are desirable to improve the accuracy of a thermal simulation model through testing.

The experimental test set-up in Figure 8 provides the natural convection heat transfer coefficient at subatmospheric pressures. The data provide an input to numerically determine the temperature error the pressure levels of the test facility and ideal vacuum conditions ($0Pa$). Figure 15 shows that pressure levels by three orders of magnitude larger than those used in environmental test standards for larger satellites [8] suffice to maintain the error below the previously defined threshold for thermal balance testing.

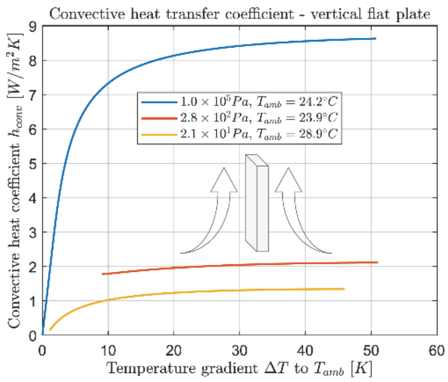

Figure 14 – Natural convection heat transfer at subatmospheric pressures.

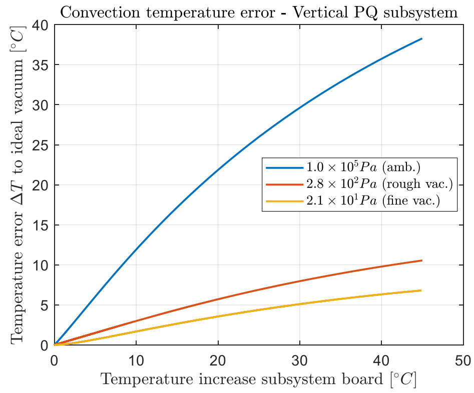

Figure 15 – Temperature error for PocketQube subsystems due to natural convection.

5. CONCLUSIONS

This paper proposes and implements a thermal screening method to check compliance of thermal hotspots with the hot-side temperature requirements. The methodology omits the necessity to conduct vacuum testing to perform an early estimation of the maximum flight temperatures. The available diagram describes the hotspot behavior of resistors providing a worst-case scenario of the thermal behavior of hotspots. Moreover, the study illustrates that pressure requirements for thermal-vacuum testing of PocketQubes can be moderated. The analysis shows that the resulting temperature error is low. The graph describing the temperature errors provides a reference to choose appropriate pressure levels. Both the screening method and moderation in vacuum requirements contribute to the development of cost- and time-effective test strategies for PocketQubes.

6. REFERENCES

[1] S. Speretta *et al.*, “Cubesats to pocketqubes: Opportunities and challenges,” in *Proceedings of the 67th International Astronautical Congress*, 2016.

[2] M. Swartwout, “Secondary spacecraft in 2016: Why some succeed (And too many do not),” in *IEEE Aerospace Conference Proceedings*, 2016.

[3] C. Venturini, B. Braun, D. Hinkley, and G. Berg, “Improving Mission Success of CubeSats,” El Segundo, Calif., USA, 2018.

[4] M. Langer and J. Bouwmeester, “Reliability of CubeSats – Statistical Data, Developers’ Beliefs and the Way Forward,” in *30th Annual AIAA/USU Conference on Small Satellites*, 2016, pp. SSC16-X-2.

[5] R. Avila de Luis, “Standardized Thermal Control Solutions for PocketQubes,” Delft University of Technology, 2018.

[6] D. G. Gilmore, *Spacecraft thermal control handbook: Volume I*, 2nd ed. El Segundo, Calif., USA: Aerospace Press, 2002.

[7] O. Breitenstein, W. Warta, and M. Langenkamp, *Lock-in Thermography*, 2nd ed. Berlin, Germany: Springer-Verlag Berlin Heidelberg, 2010.

[8] ECSS, “ECSS-E-ST-10-03C - Space Engineering, Testing,” 2012.